

The social (neural) network:
Towards a unifying endophenotype between genes and behavior

Tyler Santander
San Diego, CA

B.A., University of California, Santa Barbara, 2011

A Dissertation presented to the Graduate Faculty
of the University of Virginia in Candidacy for the Degree of
Doctor of Philosophy

Department of Psychology

University of Virginia
May 2017

FINAL EXAMINATION FORM

This form is to be completed by a student's committee and department to indicate that the student has passed the final defense of their thesis/dissertation, written or oral exams. This form must be scanned and emailed to the Enrolled Student Office by the appropriate deadline: **November 30** for December, **April 30** for May, and **July 30** for August graduation.

Last Name SANTANDER First Name TYLER University/SIS ID 517094563
 Program COGNITIVE PSYCHOLOGY (PHD) Date Final Examination Passed: 4/18/17

Master's Final Examination: A candidate must achieve satisfactory standing in a final examination (oral, written or both) conducted by two or more graduate faculty members designated by the candidate's department.

PhD Final Examination: This committee, chaired by the primary advisor, will consist of a minimum of four tenured or tenure-track members of the faculty of the Graduate School of Arts and Sciences. One member of the committee will serve as a representative of the Graduate School of Arts and Sciences to affirm that the student has been assessed fairly and with due rigor. This representative is appointed by the student's director of graduate studies and must hold a primary appointment outside of the student's department. This representative may be drawn from the tenured or tenure-track faculty of other graduate schools at the University, but must hold a Ph.D. A director of graduate studies may petition to permit a reader from outside the University who holds a Ph.D. to serve as one of the four core members of the committee by providing the associate dean with the reader's CV and a statement regarding the reader's particular suitability for the committee. This external reader may not serve as the representative of the Graduate School. Once these minimum requirements have been met, additional committee members from within the University or other institutions may be added.

Committee	Name	Signature	Department
Primary Advisor	James Morris		Psychology
Committee Member	Jessica Connelly		Psychology
Committee Member	Jason Dziugol		Radiology & Medical Imaging
GSAS Representative	Chad Dodson		Psychology
Committee Member (optional)			

Approved Title of Doctoral Dissertation or Master's Thesis if Required

THE SOCIAL (NEURAL) NETWORK:
TOWARDS A UNIFYING ENDOPHENOTYPE BETWEEN GENES & BEHAVIOR

James P Morris
Graduate Advisor
(if no thesis, Graduate Studies Director) (Print) 4/18/17
Signature Date

Donna Hearn
Department Chair or Representative (Print) 4-26-17
Signature Date

***If Advisor is the Graduate Director, Chair Signature is required. If Chair is advisor, Graduate Director Signature is required.*

This examination is in fulfillment of the requirements as described in the Record for the appropriate degree.

✓

The social (neural) network:

Towards a unifying endophenotype between
genes and behavior

©2017 Tyler Santander

Abstract

The human brain is a hierarchical system where molecular, cellular, and cortical-level components interact to produce myriad mental states. Thus, brain networks can broadly be characterized in a hierarchical fashion, such that macroscale cortical functions result from accumulated microscale events ranging from the cellular to the molecular levels. However, modern neuroimaging techniques are limited in the extent to which they can resolve these interactions. In the following set of experiments, we employ a combination of imaging epigenetics and statistical machine learning techniques to decode individual differences in epigenetic makeup from multiple modalities of macroscale brain network data. A convenient target for this approach is the oxytocin system, which is modulated by epigenetic modifications to the oxytocin receptor gene (*OXTR*). Differential levels of DNA methylation in *OXTR* are thought to have downstream effects on both social behavioral phenotypes and the development of neural networks supporting such behaviors. Using data obtained from a large sample of healthy young adults, we describe: 1) The identification of epigenetic fingerprints in macroscale neural network architecture; 2) Spatially-heterogeneous relationships between epigenetic factors and spontaneous BOLD dynamics; and 3) An entropy-based model that links epigenotypes and behavioral phenotypes through patterned network dynamics. Our approach offers both novel applications of previously-existing techniques and new tools for quantifying dynamics in functional brain networks. Together, these methods have the potential to illuminate complex interactions across multiple levels of brain systems in numerous contexts, from social behavior and beyond.

Contents

Contents	iii
List of Figures	vii
List of Tables	xv
1 Introduction	1
1.1 Oxytocin at a glance	2
1.2 The molecular and cellular bases of oxytocinergic action	2
1.3 Oxytocin as a neuromodulator	3
1.4 Genetic and epigenetic regulation of the oxytocin system	4
1.5 Oxytocin and human brain function	6
1.6 Towards a gene-brain-behavior model	8
1.6.1 Social cognition is an inferential process	10
1.6.2 Failures of inference	11
1.6.3 A “critical period” for oxytocin in social development?	12
1.7 The present investigation	15
2 Experiment 1	18
2.1 Materials and Methods	19
2.1.1 Participants	19

2.1.2	Blood collection and DNA extraction	20
2.1.3	Epigenotyping targets and procedures	20
2.1.4	Social attribution task	21
2.1.5	fMRI acquisition and preprocessing	22
2.1.6	Functional connectivity estimation	23
2.1.7	Multivariate pattern analysis: Relevance vector regression	26
2.1.8	Brain data visualization	31
2.2	Results	31
2.2.1	DNA methylation on <i>OXTR</i>	31
2.2.2	Multivariate pattern analyses	32
2.3	Discussion	33
2.3.1	Functional relevance of subnetwork regions	34
2.3.2	Network threshold and metric considerations	35
2.3.3	Implications for oxytocin action and social behavior	37
2.4	Figures	39
3	Experiment 2	45
3.1	Materials and Methods	46
3.1.1	Participants	46
3.1.2	Blood collection and epigenotyping	46
3.1.3	Resting-state fMRI acquisition and preprocessing	47
3.1.4	Brain parcellation and timeseries extraction	48
3.1.5	Quantifying BOLD dynamics	48
3.1.6	Multivariate pattern analysis: Bayesian efficient multiple kernel learning	51
3.1.7	Multivariate pattern analysis: Relevance vector regression	53
3.1.8	Brain data visualization	55

3.2	Results	55
3.2.1	DNA methylation on <i>OXTR</i>	55
3.2.2	Whole-brain BEMKL	56
3.2.3	Network-specific RVR	57
3.3	Discussion	59
3.3.1	Evidence for oxytocin-dopamine interactions	60
3.3.2	Oxytocin, social perception, and predictive coding	62
3.4	Figures	65
4	Experiment 3	73
4.1	Materials and Methods	74
4.1.1	Participants	74
4.1.2	Blood collection epigenotyping	74
4.1.3	Behavioral assessment: The broad autism phenotype	75
4.1.4	Resting-state fMRI acquisition and preprocessing	75
4.1.5	Network selection and timeseries extraction	75
4.1.6	Dynamic functional connectivity estimation	76
4.1.7	Multivariate pattern analysis: Relevance vector regression	78
4.1.8	Brain data visualization	79
4.2	Results	79
4.2.1	<i>OXTR</i> methylation and the broad autism phenotype	79
4.2.2	Connectivity entropy: Default mode network	80
4.2.3	Connectivity entropy: Salience network	81
4.3	Discussion	82
4.3.1	Open questions about methylation-behavior relationships	83
4.3.2	Functional networks and their subsystems	84
4.3.3	Entropy and the search for a gene-brain-behavior model	85

4.4	Figures	88
5	General discussion	93
5.1	Emergent phenomena and the evolution of network neuroscience . .	94
5.2	Epigenetic modulation of functional network architecture	96
5.3	Epigenetic modulation of functional network dynamics	98
5.4	Oxytocin and social inference	100
5.5	Bridging the gap between genes and behavior	102
5.6	Conclusion	103
	Bibliography	105
A	Supplementary information: Experiment 1	130
B	Supplementary information: Experiment 2	139

List of Figures

2.1	OXTR methylation by CpG site and sample. A , Distribution of percent methylation values for CpG site -934. B , Distribution of percent methylation values for CpG site -860. In both A and B , Study 1 samples ($N = 127$) are shown in light red while Study 2 samples ($N = 48$) are shown in light blue. No differences in mean methylation were observed between samples.	39
2.2	Results of relevance vector regression by threshold, metric, and CpG site. Model performance for the full 90-region network (see also Table S1), trained/tested on the Study 1 sample ($N = 127$). Left panels give prediction accuracies for CpG site -934; right panels give accuracies for CpG site -860. Performance summarized using both Pearson correlations (actual vs. predicted methylation; <i>top</i>) and model error (<i>RMSE</i> ; <i>bottom</i>). Point size indicates significance derived from 1,000 iterations of nonparametric permutation testing; similarly, darker shading indicates smaller p -values (shading is scaled by $-\log(p)$).	40

2.3 **Relevance probabilities and subnetwork map.** **A**, Regional relevance probabilities for each network metric and methylation site (models trained/tested on Study 1 data). Brighter colors indicate higher probabilities of model inclusion across all 10 threshold levels. **B**, Reduced subnetwork of anatomically-defined nodes, relevant in more than 75% of all models for either site. 41

2.4 **Subnetwork RVR performance.** Model performance (prediction correlation, *top*, and prediction error, *bottom*) for the 43-region subnetwork (see also **Table S3**), trained/tested on the Study 1 sample. Point size and shading schemes are identical to **Figure 2.2**. 42

2.5 **Multivariate weight maps derived from subnetwork relevance vector regression models.** Relevance vector regression analyses on the 43-region subnetwork revealed spatially-distributed sets of brain regions relevant for predicting individual differences in *OXTR* methylation. Models were trained and tested using data from Study 1 ($N = 127$). For both CpG site -934 (*left*) and CpG site -860 (*right*), weight maps are provided at the top 30% and top 25% connectivity thresholds. Values reflect average weights across CV folds (with unit normalization). Note that exact local inference is inappropriate given the non-independence of multivariate weights—nevertheless, “hot” colors push the prediction function towards higher expected methylation (with increased connectivity) while “cool” colors indicate the reverse. 43

2.6	Subnetwork eigencentality models generalize to new data. Applying the subnetwork models derived from Study 1 to data from Study 2 ($N = 48$) significantly predicted <i>OXTR</i> methylation on CpG site -934—this was largely threshold-invariant, but we provide the four best-fitting thresholds here. Prediction accuracy is given as model error (<i>RMSE</i>), and <i>p</i> -values were derived through 1,000 iterations of nonparametric permutation testing.	44
3.1	Shen atlas partitions. The 268 individual regions of the Shen atlas (<i>top</i>) are further partitioned into 8 functional networks (<i>bottom</i>). See Table 3.1 for network labels and sizes (i.e. number of nodes).	65
3.2	Multivariate patterns of spectral variance across the whole brain predict <i>OXTR</i> methylation on CpG site -934. Average, unit-normalized weight maps from whole-brain BEMKL analyses are given for individual regions (<i>top</i>) and networks (<i>middle</i>). In general, increased spectral variability predicted decreased methylation. The bottom panel displays the correspondence between actual methylation values (<i>black</i>) and model predictions (<i>red</i>). See Table B.1 for a full summary of model fit for all variability metrics at the whole-brain level.	66

3.3 Multivariate patterns of fALFF across the whole brain predict OXTR methylation on CpG site -860. Average, unit-normalized weight maps from whole-brain BEMKL analyses are given for individual regions (*top*) and networks (*middle*). Although some regions were weighted negative,, an increased proportion of low-frequency power across the brain (relative to the full signal power spectrum) generally predicted increased methylation. The bottom panel displays the correspondence between actual methylation values (*black*) and model predictions (*red*). See **Table B.1** for a full summary of model fit for all variability metrics at the whole-brain level. 67

3.4 Multivariate patterns of LFP in the subcortical-cerebellum network predict OXTR methylation on CpG site -860. Network-specific RVR in the subcortical-cerebellum network suggested that greater levels of low-frequency power were associated with increased methylation (weight maps, *top*, are averaged and unit-normalized). The bottom panel displays the correspondence between actual methylation values (*black*) and model predictions (*red*). See **Table B.5** for a full summary of model fit for all variability metrics in subcortical-cerebellum analyses. 68

3.5 **Multivariate patterns of entropy in the secondary visual network predict *OXTR* methylation on CpG site -934.** Both approximate entropy (*left*) and sample entropy (*right*) were significantly associated with methylation on CpG -934. We omit multivariate weight maps due to the extreme sparsity of each RVR model—ApEn was driven by a mere two regions while SampEn was driven by one region. We therefore recommend cautious interpretation of these findings. See **Table B.8** for a full summary of model fit for all variability metrics in secondary visual analyses. 69

3.6 **Multivariate patterns of LFP in the secondary visual network predict *OXTR* methylation on CpG site -934.** Low-frequency power in the secondary visual network was a weak predictor of *OXTR* methylation on CpG site -934. See **Table B.8** for a full summary of model fit for all variability metrics in secondary visual analyses. 70

3.7 **Multivariate patterns of temporal variability (σ_t) in the visual association network predict *OXTR* methylation on CpG site -934.** RVR analyses in the visual association network revealed a right-lateralized set of regions whose variability over time significantly predicted methylation (weight maps, *top*, are averaged and unit-normalized). The bottom panel displays the correspondence between actual methylation values (*black*) and model predictions (*red*). See **Table B.9** for a full summary of model fit for all variability metrics in visual association analyses. 71

3.8 **Multivariate patterns of spectral variability (σ_ω^2) in the visual association network predict OXTR methylation on CpG site -934.** RVR analyses in the visual association network demonstrated that spectral variability across a right-lateralized set of regions significantly predicted methylation (weight maps, *top*, are averaged and unit-normalized). The bottom panel displays the correspondence between actual methylation values (*black*) and model predictions (*red*). See **Table B.9** for a full summary of model fit for all variability metrics in visual association analyses. 72

4.1 **Subsystems of the default mode network.** Dynamic connectivity was assessed in two functionally-distinct subdivisions of the default mode network, as defined by the Willard atlas: the dorsal component (*left*) and the ventral component (*right*). 88

4.2 **Subsystems of the salience network.** Dynamic connectivity was assessed in two functionally-distinct subdivisions of the salience network, as defined by the Willard atlas: the anterior component (*left*) and the posterior component (*right*). 88

4.3 **Distribution of broad autism phenotype scores.** The extent to which individuals expressed autistic-like traits was normally-distributed in our sample ($N = 50$; $M = 17.02 \pm 5.38$ *SD*, range = 4-30). Note, however, that none exceed the suggested clinical cutoff of 32. 89

4.4 **Relationships between BAP and OXTR methylation by sex and CpG site.** In general, higher levels of methylation predicted lower expression of the broad autism phenotype, but there was not a significant effect of sex (nor an interaction between methylation and sex; see **Table 4.1** for parameter estimates from a linear mixed effects model). 90

4.5 **Connectivity entropy in the dorsal DMN predicts OXTR methylation and BAP scores.** Multivariate weight maps for edgewise connectivity entropy are displayed for CpG site -860 (*left*) and BAP (*right*). Weights were exclusively positive for the methylation model, such that increased entropy across the network predicted increased levels of methylation; similarly, weights were almost entirely negative for the BAP model, such that more entropic brains were associated with lower levels of BAP. Bottom panels display the correspondence between target values (*black*) and relevance vector model predictions (*red*). 91

4.6 **Connectivity entropy in the anterior SN predicts OXTR methylation.** Multivariate weight maps for edgewise connectivity entropy are displayed for CpG site -860 (*left*) and CpG site-934 (*right*). Unlike the dorsal DMN, connectivity entropy did not predict behavior. For both models, weights were exclusively positive, such that increased entropy across the network predicted increased levels of methylation. Bottom panels display the correspondence between target values (*black*) and relevance vector model predictions (*red*). 92

A.1 **Proportional thresholds nontrivially affect overall network topology.** Degree distributions for each threshold are given for the full 90-region network (Study 1 data, $N = 127$). As the threshold becomes more stringent, the distribution approaches a heavily-tailed power law—this is characteristic of so-called “small-world” networks where a few highly-connected hubs control most of the information flow. 131

A.2 Multivariate weight maps derived from the full 90-region network.

Relevance vector regression identified a highly consistent set of regions relevant for predicting *OXTR* methylation. Models trained/tested using Study 1 data ($N = 127$). For simplicity, only models from CpG site -860 are presented here; weight maps are provided at the top 30% and top 25% thresholds. Values reflect average weights across CV folds, normalized to unit length. “Hot” colors push the prediction function towards higher expected methylation (with increased connectivity) while “cool” colors indicate the reverse. 132

List of Tables

2.1	Independent model fit: Eigencentality on CpG site -934. Model error (<i>RMSE</i>) after applying Study 1 subnetwork models to Study 2 data (<i>p</i> -values derived from 1,000 iterations of nonparametric permutation testing).	34
3.1	Networks of the Shen atlas. Network labels with corresponding numbers of nodes. The far right column indicates whether network data must be compressed to a linear kernel for relevance vector regression (based on the number of ROIs relative to the sample size). See Figure 3.1 for a visual map.	49
4.1	Inter-individual variability in <i>OXTR</i> methylation predicts differences in the broad autism phenotype. A linear mixed-effects model demonstrated a significant inverse relationship between <i>OXTR</i> methylation and the broad autism phenotype. <i>T</i> -statistics and <i>p</i> -values obtained using the Satterthwaite approximation. Although there was not a significant interaction between sex and methylation, CpG site and sex-specific relationships are visualized in Figure 4.4	80

4.2 **RVR model fit: Default mode network.** Prediction accuracies (*RMSE*) are given for RVR models on dDMN and vDMN data (see **Figure 4.5** for weight maps corresponding to significant dDMN analyses). *P*-values derived from 1,000 iterations of nonparametric permutation testing are given in parentheses. 81

4.3 **RVR model fit: Salience network.** Prediction accuracies (*RMSE*) are given for RVR models on aSN and pSN data (see **Figure 4.6** for weight maps corresponding to significant aSN analyses). *P*-values derived from 1,000 iterations of nonparametric permutation testing are given in parentheses. 82

A.1 **Whole-brain RVR model fit: CpG site -934.** Model fit statistics (*prediction correlation* and *prediction error*) are given for each metric and network threshold. *P*-values derived from 1,000 iterations of nonparametric permutation testing are given in parentheses. 133

A.2 **Whole-brain RVR model fit: CpG site -860.** Relevance vector regression fit statistics (*prediction correlation* and *prediction error*) are given for each metric and network threshold. *P*-values derived from 1,000 iterations of nonparametric permutation testing are given in parentheses. . . 134

A.3 **Relevance probabilities: CpG site -934.** For each AAL node and network metric, we give the probability of inclusion across RVR models for CpG site -934. Metric-specific columns indicate the probability of nonzero weight across all network threshold levels; the far right column gives the mean. Starred (*) nodes were ultimately included in the 43-region subnetwork (relevant in over 75% of models for *either* CpG site -934 or CpG site -860). 135

- A.4 **Relevance probabilities: CpG site -860.** For each AAL node and network metric, we give the probability of inclusion across RVR models for CpG site -860. Metric-specific columns indicate the probability of nonzero weight across all network threshold levels; the far right column gives the mean. Starred (*) nodes were ultimately included in the 43-region subnetwork (relevant in over 75% of models for *either* CpG site -934 or CpG site -860). 136
- A.5 **Subnetwork RVR model fit: CpG site -934.** Fit statistics (*prediction correlation* and *prediction error*) from subnetwork relevance vector regression are given for each metric and network threshold. *P*-values derived from 1,000 iterations of nonparametric permutation testing are given in parentheses. 137
- A.6 **Subnetwork RVR model fit: CpG site -860.** Fit statistics (*prediction correlation* and *prediction error*) from subnetwork relevance vector regression are given for each metric and network threshold. *P*-values derived from 1,000 iterations of nonparametric permutation testing are given in parentheses. 138
- B.1 **Whole-brain BEMKL model fit.** Values indicate root mean squared error (*RMSE*) across CV folds; *p*-values from 1,000 iterations of nonparametric permutation testing are given in parentheses. 140
- B.2 **Medial frontal RVR model fit.** Values indicate root mean squared error (*RMSE*) across CV folds; *p*-values from 1,000 iterations of nonparametric permutation testing are given in parentheses. 140
- B.3 **Frontoparietal RVR model fit.** Values indicate root mean squared error (*RMSE*) across CV folds; *p*-values from 1,000 iterations of nonparametric permutation testing are given in parentheses. 140

B.4	Default mode RVR model fit. Values indicate root mean squared error (<i>RMSE</i>) across CV folds; <i>p</i> -values from 1,000 iterations of nonparametric permutation testing are given in parentheses.	141
B.5	Subcortical-cerebellum RVR model fit. Values indicate root mean squared error (<i>RMSE</i>) across CV folds; <i>p</i> -values from 1,000 iterations of nonparametric permutation testing are given in parentheses.	141
B.6	Motor RVR model fit. Values indicate root mean squared error (<i>RMSE</i>) across CV folds; <i>p</i> -values from 1,000 iterations of nonparametric permutation testing are given in parentheses.	141
B.7	Visual I RVR model fit. Values indicate root mean squared error (<i>RMSE</i>) across CV folds; <i>p</i> -values from 1,000 iterations of nonparametric permutation testing are given in parentheses.	142
B.8	Visual II RVR model fit. Values indicate root mean squared error (<i>RMSE</i>) across CV folds; <i>p</i> -values from 1,000 iterations of nonparametric permutation testing are given in parentheses.	142
B.9	Visual association RVR model fit. Values indicate root mean squared error (<i>RMSE</i>) across CV folds; <i>p</i> -values from 1,000 iterations of nonparametric permutation testing are given in parentheses.	142
B.10	Average whole-brain correlations between BOLD variability metrics. <i>Z</i> -scored mean correlation coefficients across all participants are given for each pairwise comparison. In general, entropy measures were significantly related to each other but not to any other metrics. Temporal and spectral variability measures (including LFP and fALFF) were also significantly correlated. Together, this suggests that entropy is capturing a unique functional characteristic of the BOLD signal relative to other standard measures of BOLD variability.	143

Acknowledgements

I wish to extend my deepest thanks to my friends and colleagues in the Social Neuroscience Lab at the University of Virginia. In particular, I would like to acknowledge Meghan Puglia for her careful work in generating the epigenetic data that were central to this work, and my advisors, Jamie Morris and Jess Connelly, for allowing me to relentlessly plumb the infinite depths of their patience.

To my mother, Wendy. The English language is woefully lacking in words to express my gratitude for her unending support. None of this would have been possible without her.

Chapter 1

Introduction

The human brain is a complex system in which numerous spatially-distributed networks interact to produce myriad mental states. These networks can broadly be characterized in a hierarchical fashion with increasing spatial resolution, such that *macroscale* cortical functions result from accumulated *microscale* events ranging from the cellular to the molecular levels. However, modern neuroimaging techniques are limited in the extent to which they can resolve these interactions. Functional magnetic resonance imaging (fMRI), for example, is able to measure metabolic events on the scale of millimeters—but each voxel itself contains hundreds of thousands of neurons. Furthermore, the molecular mechanisms governing inter-neuron communication are regulated by genetic and epigenetic factors that may be transient or otherwise impossible to measure in the living human brain. In the following experiments, we use the oxytocin system in social cognition as a foundation to demonstrate that such microscale-molecular factors can be *decoded* from macroscale functional network characteristics. Moreover, we show that these network features not only predict one's molecular makeup—they also inform social-behavioral phenotypes commonly associated with oxytocinergic action.

1.1 Oxytocin at a glance

Oxytocin (OT) is a nonapeptide with wide-reaching targets across both the brain and peripheral body¹⁻³. As a central neurotransmitter and neuromodulator, oxytocin has been associated with a number of neural phenomena in nonhuman animals, including anxiolysis⁴ and the adjustment of neural signal-to-noise ratios (SNR) during long-term potentiation^{5,6}. In humans, a growing body of research has demonstrated that intranasal administration of oxytocin acutely modulates the function of brain networks in support of social cognition⁷⁻¹².

The integral role of oxytocin in social behavior is without dispute^{2,13}. Commonly referred to as the “love hormone,” oxytocin has indeed been shown to promote feelings of trust^{14,15}, empathy¹⁶, and social closeness¹⁷ in humans. The intranasal administration of oxytocin also provides short-term benefits for emotion recognition and inference¹⁸, memory for faces¹⁹, biological motion detection²⁰, and even social behavior in psychiatric populations^{21,22}. However, oxytocin has evolutionarily-ancient roots, with variations appearing in all known vertebrate species^{2,23-26}—it is therefore dubious that oxytocin’s primary function in the brain is to promote human constructs such as trust or love. Rather, a more compelling alternative is that oxytocin aids in the development of distributed neurobiological systems that variously support complex social, emotional, and cognitive processes⁶.

1.2 The molecular and cellular bases of oxytocinergic action

Oxytocin is synthesized in the paraventricular (PVN) and supraoptic (SON) nuclei of the hypothalamus and released into the bloodstream via the posterior pituitary²⁷. Its action in the brain is facilitated through a single G-protein coupled receptor type

(hereafter referred to simply as the *OT receptor*)^{3,28}. However, structural similarities between oxytocin and a related nonapeptide, arginine vasopressin (AVP), have complicated efforts to develop a ligand selective for the OT receptor alone^{29,30}—thus, it has been historically difficult to characterize the distribution of OT receptors throughout the brain. Early work in mice and prairie voles demonstrated that OT receptors are abundant in the striatum, thalamus, and amygdala (components of the so-called “limbic system”)^{1,31–33}. These regions receive direct axonal projections from OT neurons in the hypothalamus and are associated with the various social-behavioral consequences of oxytocin action^{27,34–36}.

Importantly, the hypothalamic-limbic pathway of oxytocin signaling is only a small piece of the puzzle. Receptors have also been found in spatially-distant regions of the brain that do *not* receive direct projections from oxytocinergic neurons in the hypothalamus, such as the anterior cingulate cortex (ACC) and prefrontal cortex (PFC)²⁷. Oxytocin activity in these areas is a function of *paracrine* signaling processes, which are critical for the distributed central nervous effects of many neuropeptides^{37,38}. Through this mechanism, oxytocin is secreted from dendrites and axonal varicosities into the extracellular matrix where it can then travel across the brain. A key observation is that oxytocin has a remarkably long half-life compared to classical neurotransmitters (20 minutes vs. 5 milliseconds)^{37–39}, which suggests it is plausible for oxytocin to diffuse over vast neuronal distances and effect long-lasting changes in brain function and behavior.

1.3 Oxytocin as a neuromodulator

Perhaps a greater role for oxytocin lies not in its function as a primary neurotransmitter, but rather as a *neuromodulator*. In particular, two recent studies have highlighted the possibility that oxytocin is a key player in modulating neural SNR

and promoting neural plasticity during long-term potentiation (LTP)^{5,6}—a process classically associated with dopamine (DA), which is known to enhance learning via coordinated *gain modulation* (i.e. amplifying SNR across ensembles of neurons in response to relevant input signals)^{40–45}. These findings suggest that oxytocin and dopamine function may be intimately linked, a notion supported by animal work describing direct projections from OT neurons to DA-rich basal ganglia regions²⁷ and general co-expression of OT/DA receptors (both in hypothalamic-limbic regions and prefrontal areas not receiving direct OT projections)^{46–48}. Critically, one study demonstrated that blockading *either* OT or DA receptors in the striatum diminished social affiliative behaviors in voles—even when using an agonist to amplify the activity of the other neurotransmitter⁴⁷. Thus, it is becoming increasingly clear that joint-modulation of OT/DA systems is a critical facet of the neurobiology underlying social behavior^{13,49–54}. Moreover, because DA-rich subcortical areas heavily modulate the activity of widely-distributed cortical systems^{40–43}, this observation provides yet another (indirect) route through which oxytocin can drive changes in large-scale brain function.

1.4 Genetic and epigenetic regulation of the oxytocin system

Regardless of how oxytocin arrives at a given brain region—either via direct projection or paracrine diffusion—its potential for effect is limited by the availability of OT receptors. Consequently, a critical mediator of oxytocinergic action in the brain is the oxytocin receptor gene (*OXTR*; hg38, chr3: 8,750,409-8,769,614). Broadly-speaking, genetic variants in *OXTR* (single nucleotide polymorphisms, SNPs; and copy number variants, CNVs) have been linked to differences in brain structure^{55–57},

function^{50,57-61}, and may also provide an etiological basis for autism spectrum disorders (ASD)⁶²⁻⁶⁷. Frustrated efforts to replicate these associations⁶⁸⁻⁷⁰ or further solidify *OXTR*'s status as the "sociability gene"⁷¹ have often been attributed to within-group differences in factors such as gender and early life experience, which might confound links between genetics and behavior. A potential unifying explanation might instead be an oversight of *epigenetic* modifications along *OXTR* that further regulate the oxytocin system.

Although a number of epigenetic processes are known to occur in the genome, DNA methylation of 5'-Cytosine-phosphate-Guanine-3' (CpG) dinucleotide pairs is among the most studied in humans. Unlike a SNP, which often requires individuals to be dichotomized by allele, methylation on a CpG site can be measured as a continuous variable (0-100%), which offers more explanatory power with regard to tracking individual differences. Moreover, increased levels of DNA methylation have direct functional consequences by (typically) decreasing the expression of genes⁷². In the case of *OXTR*, the functions of associated allelic variants in humans have not been identified, nor have they been linked to transcriptional changes in the gene.

Several studies have begun to illuminate the potential functions of epigenetic modifications along *OXTR*. Early work showed that increased methylation indeed reduces transcription of the gene⁷², thereby limiting one's endogenous access to oxytocin. Later studies have shown that higher levels of *OXTR* methylation are associated with various psychiatric conditions, including autism^{63,73-76}. Critically, one report⁶³ demonstrated that methylation levels derived from peripheral sources (e.g. blood) reported on elevated levels in brain tissue. The persistence of *OXTR* methylation levels across tissue types raises the possibility that methylation may be established early in life, further validating its usefulness as a noninvasive biochemi-

cal marker in human adults.

1.5 Oxytocin and human brain function

A relatively-recent effort to elucidate the role of oxytocin in human brain systems is gaining momentum. In an effort to mimic pharmacological manipulations in animal research, most studies have relied on intranasal administrations of oxytocin. This methodology is rooted in fact that oxytocin and other large peptides are unable to cross the blood-brain barrier; intranasal administration, by contrast, allows for potential diffusion into cerebrospinal fluid (CSF) and consequently the brain (although there is dispute over the extent to which CSF and blood OT levels are amplified via intranasal administration)⁷⁷⁻⁷⁹. A number of studies using intranasal OT have shown that oxytocin, relative to placebo, modulates task-related BOLD (blood oxygen level dependent) activity across various regions comprising the “social brain”^{8,10,11,59,80}—these include areas such as the amygdala (AMG), medial PFC (mPFC), insula, fusiform gyrus (FG), superior temporal sulcus (STS), and inferior frontal gyrus (IFG), among others⁸¹⁻⁸³. Importantly, however, the effects of OT administration on regional brain function are *acute* and, in some cases, both regional- and context-dependent. For example, one study reported OT-induced *increases* in AMG activity when viewing *happy* faces and *decreased* AMG activity to *angry* faces⁸⁰. Similarly, another group reported (in women) *increased* activity in the AMG, FG, and superior temporal gyrus when viewing *fearful* faces, but activity was *decreased* in the IFG in response to *angry* and *happy* faces⁸⁴. Finally, a pair of studies suggested OT administration *decreased* the AMG response to infant crying *and* infant laughter; infant crying was further associated with *increased* insula and IFG activity, but this did not hold for laughter^{11,59}.

So, while oxytocin is without doubt central to social cognition, its functional

role in the brain is highly complex. One broad explanation is that OT increases the response to positively-valenced social information while decreasing the response to aversive or threatening social information—both would suggest that oxytocin enables various types of social reinforcement learning, and the latter phenomenon is in agreement with animal and human research suggesting an anxiolytic effect of oxytocin^{4,85–87}. That being said, there are clear examples of this dichotomy breaking down (e.g. work showing that oxytocin enhances feelings of jealousy and *schadenfreude*⁸⁸). A focus on regional activity (while a good place to start) also belies the true nature of the brain: complex social behaviors manifest from the concerted activity of distributed neural *systems*—not any single brain region.

A rapidly-growing set of studies have accordingly investigated the effects of intranasal OT on functional network connectivity. There are many methods available for modeling brain networks that are beyond the scope of the current discussion; here, we simply use *functional connectivity* in reference to any statistical dependence between two waveforms of brain activity. For example, a pair of regions who are oscillating “in-phase” (i.e. rising and falling in activity together over time) are said to be *functionally-coupled*—a group of functionally-coherent brain areas then comprise a *network*. Note that this does not *require* direct axonal connections between brain regions, but there is evidence that functional networks indeed reflect underlying structural connectivity^{89,90}.

In general, most evidence points to oxytocin administration enhancing functional coupling across the brain, both at rest and under task-positive states⁷. For example, intranasal OT commonly increases functional connectivity from the amygdala to areas such as the insula⁹¹, mPFC^{12,92,93}, anterior cingulate⁹², and a number of additional brain regions relevant for social perception⁹ and emotion regulation¹¹. OT administration may also enhance connectivity between mesolimbic

and prefrontal regions important for social motivation⁹ and social evaluation⁹⁴. Instances of *decreased* functional connectivity have been attributed to processes such as emotional dampening^{10,95,96} and modulation of approach-avoidance behaviors⁹⁷. Importantly, several of these reports suggested a potential therapeutic role for OT administration in cases of trauma⁹⁵, social anxiety⁹², and autism^{9,12,94}.

It is worth reiterating, however, that the effects of intranasal OT on brain function are *acute*—there is little evidence of any benefits persisting in the weeks or months following treatment. There also remains healthy debate over the mechanism of action for intranasal OT and the accuracy with which we can measure peripheral levels of the peptide itself^{78,98}. We propose that a focus on epigenetic modifications to *OXTR* may be a more reliable indicator of endogenous oxytocin action, as *OXTR* methylation directly mediates access to oxytocin (by regulating receptor expression). In other words, even if intranasal OT *does* increase central nervous concentrations, receptor availability puts a hard upper bound on its potential to modify brain function and behavior. Mounting evidence indicates that genetic/epigenetic variations in *OXTR* may specifically contribute to phenotypic differences in social behavior by modulating the functional neuroanatomy of a number of brain regions⁸³. Our own work among adult neurotypicals has supported this, demonstrating that increased *OXTR* methylation predicts increased regional BOLD responses during social cognition^{99,100}.

1.6 Towards a gene-brain-behavior model

An emerging hypothesis suggests that healthy social behavior is driven by a robust oxytocin system early in life, which enhances the neural mechanisms of social learning¹⁰¹. A related model similarly proposes that oxytocin facilitates social behavior via dopaminergic systems that form the biological basis of learning, motivation,

and reward^{13,49,51,52}. The logic of this hypothesis can be intuitively understood with a simple thought experiment:

Imagine you are sitting at work and you hear an eruption of laughter from a group of colleagues down the hall. Your brain's first task has already been completed effortlessly—you perceived the auditory input, oriented your attention to it, and tagged it as something socially relevant, perhaps with an additional positive emotional valence (if you aren't paranoid they might be laughing at your expense). You then decide to get up and investigate the commotion: this requires an internal push (*motivation*) and the development of a motor plan to engage in social interaction. Walking down the hall, you come upon your colleagues huddled around a computer watching videos of cats on the Internet. They invite you to join, you enjoy a few shared laughs, and you walk back to your desk, smiling. Again rather effortlessly, your brain engaged in a complex empathetic, joint-emotional experience and you left feeling *good* about it. And presumably this sort of reinforcement has happened before (i.e. it has been *learned*), otherwise you might not have been motivated to leave your desk in the first place!

All of these processes require coordinated activity across networks that are oxytocin and dopamine rich. On a mechanistic level, it implies that oxytocin works with dopamine to amplify the *salience* of social information in the environment, which can then be perceived and appropriately acted upon.

1.6.1 Social cognition is an inferential process

To further illustrate the putative function of this system, suppose you see a friend who appears to be very upset: she is sitting with her head cradled in her hands, and you can hear muffled cries slipping between her fingers.

This perceptual signal travels along a so-called “bottom-up” pathway through the brain. In parallel fashion, visual and auditory systems are activated in response to the scene before you. Autonomic nervous responses are also triggered in circuits densely-populated by OT receptors (e.g. the brainstem, basal ganglia, hypothalamus, and amygdala)^{1,31,34}. Thus, an *exteroceptive* social cue (your friend crying) forms an *interoceptive* response—an internal representation of a cognitive-emotional state that must be interpreted by higher-level cortical systems in order to make the correct behavioral response. For this to occur, your brain must integrate and compare these interoceptive signals against an *a priori* model of the world that is largely *embodied*. In other words, your brain attempts to simulate the scene in front of you from a self-perspective, asking: *What do these signals mean? If I were posed in such a manner, how would I be feeling? How would I expect another person to react?*^{102,103} A simulation of this type is known as a *generative model*; in this context, we might call it a generative model of the “social-emotional self,” as you are required to imagine both how *you* would feel and how you would expect *others* to respond.

Taking a step back from underlying mechanisms, this is clearly a neurobiological account of *empathy*. Formally, however, we refer to this process as *predictive coding*. Bottom-up environmental inputs are tested against a top-down hypothesis—an expectation about how the world *should* work based on your prior experience with it¹⁰⁴. Interestingly, this sort of embodied, emotional assessment and prediction is thought to rely on regions such as the insula, anterior cingulate, and mPFC^{105,106}, all of which have been previously associated with oxytocin action^{12,91–93,99,100}. UI-

tunately, you likely assess that your friend is in distress, and you respond by approaching and comforting her. This may be met with a positive response, thereby reinforcing your prior model of the world; alternatively, it may be resisted, which yields *prediction error*. The latter triggers a separate cascade of neural events that *updates* your model of the world, modifying your preponent behavioral response in order to avoid social reproach in the future.

1.6.2 Failures of inference

In many cases, this process is hidden to our conscious access. You don't *feel* or realize your brain is testing such a complex model because it happens so readily and effortlessly. As it were, this is a critical feature of the system. Drawing an emotional inference requires internally simulating the physiology of the emotional response itself, but in order to react appropriately, your outward expression of the response must be suppressed—you cannot help your friend if you become flustered yourself. A failure of suppression in this context is known as *emotional contagion*. Individuals with ASD commonly experience emotional contagion^{107,108}, suggesting they generate an internal representation of external emotional cues, but they lack the parasympathetic resources necessary to attenuate the autonomic, physiological response^{109–112}. Coupled with a vast body of evidence to suggest autistic individuals have a generally-decreased sense of self^{113–116}, this may explain why empathic deficits are a classical symptom of social-behavioral disorders¹¹⁷—the inability to ground internalized, autonomic responses within an embodied sense of the emotional self prohibits an appropriate behavioral response and effective updating following prediction error^{107,108}.

1.6.3 A “critical period” for oxytocin in social development?

It has been said that, “If you know one person with autism, you know *one person* with autism.” This underscores the notion that autism and its related phenotypes are extremely variable across the spectrum. However, ASD is commonly characterized by deficiencies in the oxytocin system^{63,118,119}—the work reviewed here suggests that early oxytocin dysfunction precludes the plasticity required to establish brain systems that support healthy social cognition. At the structural level, oxytocin has been shown to promote encephalization and neuronal growth *in vitro*¹²⁰. A pair of studies *in vivo* similarly demonstrated that oxytocin enhanced neurogenesis in the hippocampus^{121,122}.

It is well-known that dynamic structural changes in the hippocampus are central to learning and memory processes. This brand of neural plasticity (long-term potentiation) is classically taught to young psychologists using the mnemonic: *neurons that fire together, wire together*. In other words, the physical basis of learning requires persistent, coherent activity across ensembles of neurons. Precision in the timing of neural events further necessitates high signal-to-noise ratios—a function traditionally ascribed to dopamine^{40–45}, but for social learning, oxytocin likely plays a critical modulatory role. Indeed, animal research has shown that oxytocin enhances neural SNR and promotes hippocampal spike coupling⁶, ultimately leading to improvements in late-stage LTP⁵.

The joint effects of oxytocin and dopamine may therefore allow for efficient allocation of attentional and neural resources to learn salient social information early in the lifespan—likely starting mere days after birth. Infants who are several days old, for example, readily engage in shared attentional processes via mutual eye gaze¹²³. The ability to infer emotional states from the eyes is dependent on oxytocin¹⁸ and is arguably a cornerstone of the generative model defining one’s

social-emotional sense of self.

However, as aforementioned, the fine-tuning of top-down predictions is not possible without bottom-up prediction error. This requires considerable precision with respect to evaluating perceptual inputs from the environment. In other words, a number of emotional states may produce similar physiologic responses, and higher-level cognitive systems must nevertheless find a means of differentiating between feelings of fear, anger, and so on. Moreover, given the context, this physiologic simulation may require suppression in order to engage in the appropriate social behavior. Dopamine, gamma-aminobutyric acid (GABA), and other classical neurotransmitters have all been associated with modulating bottom-up inputs in order to facilitate accurate inference¹²⁴. Oxytocin interacts with all of these systems¹²⁵, modulating dopaminergic function in mesolimbic pathways central to gain modulation, motivation, and action^{50,51}, and GABA-ergic inhibition of autonomic emotional responses in the amygdala and hypothalamus^{126,127}. Oxytocin dysfunction in these feedback loops may therefore disrupt the fine-tuning of predictive models in two ways: 1) inaccurate labeling of internal physiologic states (causing a decreased sense of the emotional self), and 2) the inability to suppress simulated responses (causing emotional contagion but not empathy).

The common denominator between learning (model building) and updating (precision tuning) is the need for coordinated action across distributed neurobiological systems. We have discussed a role for oxytocin in modulating processes such as LTP, but more broadly, there is evidence to suggest that oxytocin initiates and fosters coherent activity across neural networks—both at the cellular level and macroscopic cortical level^{7,128}. Indeed, if cellular systems are *not* firing together (and consequently not wiring together), we would expect this level of disconnection to cascade upwards into higher-level networks, and recent evidence suggests this is

true for human brain systems¹²⁹. It is therefore unsurprising that ASD phenotypes are commonly associated with *hypoconnectivity* and generally “noisy brains”^{130–132}. Such low-fidelity signaling is likely a result of oxytocin dysfunction starting at the cellular level, prohibiting the robust coupling of large-scale networks in support of social perception, inference, learning, and motivation.

Because this implies an early developmental origin, it is plausible to suspect an underlying genetic cause. As aforementioned, the oxytocin receptor gene (*OXTR*) is a critical mediator of one’s endogenous access to oxytocin, and genetic variants in *OXTR* have frequently been associated with ASD phenotypes^{62–67}. However, identifying a genetic association does not necessarily inform our understanding of the gene’s *function* on a molecular level. In humans, variants in *OXTR* have been associated with differences in the brain^{50,55–61}, but there is no known effect of allelic variation on gene transcription or related signaling pathways. In contrast, epigenetic modifications such as DNA methylation *do* have direct functional consequences, limiting the expression of OT receptors across the brain⁷². Accordingly, *OXTR* methylation has been associated with autism spectrum disorders⁶³ and is thought to be sensitive to early life experiences¹³³.

If *OXTR* methylation *is* established in early stages of the lifespan, driving changes in the development of social behavior and its related neurobiological systems, a critical assumption for human neuroscience is that these epigenetic fingerprints persist and are detectable in adolescence and adulthood. Animal models suggest this assumption is likely to hold: there is evidence that early life experiences predict differential expression of *OXTR* and associated socio-sexual behaviors^{134–137}. Human research has also shown that *OXTR* methylation levels may persist across central and peripheral tissue sources⁶³, suggesting early-life modifications to the gene. Finally, we have demonstrated that *OXTR* methylation predicts differences in

adult brain function—both at the regional level and across a putative network for social-emotional information processing^{99,100}.

1.7 The present investigation

We endorse the notion that endogenous access to oxytocin, regulated by DNA methylation in *OXTR*, plays a critical role in the development of brain systems that support a wide array of social behaviors. However, to date, nearly all studies demonstrating associations between epigenetics and neural activity (or oxytocin and neural activity, more broadly) have focused on regional hypotheses or mass-univariate approaches to statistical modeling. This includes studies of functional connectivity, which have almost exclusively employed seed-based models that require strong anatomical assumptions and are blind to multivariate interactions across the whole network. Here, we utilize an entirely bottom-up, data-driven methodology, employing machine learning techniques across spatially-distributed (in some cases whole-brain) functional networks. This approach affords considerable conceptual and methodological advances over previous voxelwise/regional analyses, allowing us to tie complex network characteristics to differences in the fundamental, molecular foundations of the brain. Moreover, we demonstrate that the same network characteristics predicting *OXTR* methylation also inform individual differences in social-behavioral phenotypes. We describe several experiments toward these ends, building from the molecular level to behavioral outcomes.

Experiment 1: Identify epigenetic fingerprints in macroscale neural network architecture.

Hypothesis: Multivariate patterns of connectivity in task-related neural networks will predict variability in the epigenetic factors contributing to their development.

Understanding the molecular basis of human neural network function. While the links between brains and behavior are growing ever-stronger, the molecular mechanisms guiding and supporting functional network connectivity are only just beginning to be understood^{61,100,138–142}. Our approach employs data-driven machine learning techniques—so-called *multivariate pattern analyses* (MVPA)—to demonstrate that epigenetic information can be *decoded* from patterns of functional network architecture. This offers a means of reverse-engineering the brain from macroscale systems to underlying molecular makeup with relevance to disease processes such as ASD.

Experiment 2: Examine relationships between epigenetic factors and spontaneous BOLD dynamics.

Hypothesis: Multivariate patterns of BOLD variability will index DNA methylation on OXTR.

Extending animal literature to human subjects. Recent work in animals has highlighted the neuromodulatory role of oxytocin in adjusting neural SNR^{5,6}. However, to date, no studies have been conducted in humans to examine this relationship. We therefore employ resting-state fMRI (rs-fMRI) to determine how individual differences in baseline system dynamics index the epigenetic factors that regulate oxytocin action, particularly within networks previously implicated in social cognition (e.g. the default mode network, DMN)¹⁴³. Notably, while **Experiment 1**

is concerned with the *spatial topology* of functional brain networks, **Experiment 2** explores spatial patterns of *variability* in the BOLD signal.

Experiment 3: Bridge epigenotypes and behavioral phenotypes through patterned network dynamics.

Hypothesis: Patterns of dynamic functional connectivity offer a unifying neural endophenotype that explains both underlying molecular makeup and phenotypic outcomes.

Building comprehensive gene-brain models for social behavior. Autism spectrum disorders are highly variable, complex phenotypes that are characterized by oxytocin deficiencies, hypoconnectivity, and generally “noisy brains”^{63,130–132}. Our dataset is comprised of molecular, neural, and behavioral measures (the broad autism phenotype, BAP¹⁴⁴) that are uniquely suited to assess these common facets of ASD simultaneously. We propose a model in which hypoconnectivity is not truly an indicator of disconnected brain regions, but rather noisy, transient connections that flicker in and out of the network over time. Oxytocin deficiencies (indexed by increased *OXTR* methylation) are offered as an explanatory underlying mechanism: oxytocin dysfunction reduces neural SNR in response to social information, precluding the development of robust functional networks for social cognition. As modern neuroscience and psychology move forward, complex phenotypes (from healthy behavior to disease states) will inevitably be understood through constellations of factors realized at multiple levels of the system in question. Here we propose a strong first step towards that direction in our conception of social behavior.

Chapter 2

Experiment 1

There is increasing evidence to suggest that genetic and epigenetic regulation of the oxytocin system contributes to developmental differences in the neurobiology of social cognition. Our own work has previously shown that epigenetic variability in the oxytocin receptor gene explains individual differences in the neural processing of social information, both at the regional level^{99,100} and with respect to amygdalar functional connectivity¹⁰⁰. However, it remains unknown how *OXTR* methylation might affect the coupling of more widespread networks underlying social cognition.

We therefore hypothesized that social task-related network topologies are stamped with an epigenetic fingerprint of sorts, which should allow us to decode individual differences in *OXTR* methylation from spatial patterns of functional connectivity. To test this, we present a novel approach using statistical machine learning coupled with graph theoretic measures of network connectivity to predict inter-individual variability in *OXTR* methylation. We first describe the construction and validation of machine learning models on task-related network data using a large sample of healthy young adults. We then demonstrate that it is possible to generalize these models to a new set of individuals. Together, these results show that intrinsic network connectivity is an informative endophenotype for individual differences

at the epigenetic level.

2.1 Materials and Methods

2.1.1 Participants

We present data from two sets of healthy young adults who participated in these experiments for monetary compensation. Study 1 participants performed three social-cognitive tasks in the fMRI scanner; Study 2 participants completed a larger task battery in addition to resting state fMRI. Here, we focus on a social attribution task common across groups. Both provided blood samples for epigenotyping—in order to prevent population stratification artifacts with respect to epigenetic markers, only Caucasians (self-reported) were included in the present analyses. All individuals provided written informed consent for a protocol approved by the University of Virginia Institutional Review Board (Protocol 15051; Principal Investigator, Jessica J. Connelly).

Study 1 sample. The primary sample consisted of 150 individuals. Two participants were excluded for non-Caucasian descent; two individuals were excluded for providing incomplete methylation data; and an additional 19 were excluded for excessive head motion during the fMRI task (mean framewise displacement ≥ 0.50 mm and/or a single frame of motion ≥ 3 mm). The Study 1 sample was therefore comprised of 127 individuals (60 men, 67 women; $M_{age} = 22.13 \pm 2.98$ *SD*, range = 18-30).

Study 2 sample. Data from a second study (61 participants) were reserved for further model testing. One individual was excluded for non-Caucasian descent; one individual was excluded for providing incomplete methylation data; and an additional 11 were excluded for excessive head motion. Thus, the Study 2 sample

was comprised of 48 individuals similar in age and gender makeup to Study 1 (24 men, 24 women; $M_{age} = 20.94 \pm 2.85 SD$, range = 18-30).

2.1.2 Blood collection and DNA extraction

All individuals underwent venipuncture at the UVA Fontaine Research Park. Eight milliliters of blood were collected in mononuclear cell separation tubes (BD Vacutainer CPT with sodium citrate; BD Biosciences). Samples were immediately spun for 30 minutes at 1,800 relative centrifugal force to separate the mononuclear cell fraction (as per product protocol). The mononuclear cells were subsequently lysed, and DNA was extracted using the reagents supplied in the Gentra Puregene Blood Kit (Qiagen). DNA was stored at -20°C until further analysis.

2.1.3 Epigenotyping targets and procedures

We assessed percent DNA methylation on *OXTR* CpG sites -934 (hg38, chr3: 8,769,121) and -860 (hg38, chr3: 8,769,047). These targets were identified from prior work demonstrating differential methylation in autistics versus neurotypicals, both in peripheral blood mononuclear cells (PBMCs) and cortical tissue⁶³. Methylation at these sites has also been shown to directly impact gene expression⁷² and covary with BOLD activity in various social-cognitive tasks^{99,100}. Prior to epigenotyping, 200 ng of DNA were bisulfite converted for each participant (Kit MECOV50; Invitrogen), which allows for detection of methylated cytosines by converting all non-methylated cytosines to uracil. We then used 12 ng of bisulfite-treated DNA as templates for PCR amplification, performed in triplicate on three identical machines (C1000 Thermal Cycler; Biorad). Successful amplification was confirmed with agarose gel electrophoresis. Pyrosequencing was subsequently performed using Qiagen PyroMark Q24 Classic and Pyromark reagents per the manufacturer's

protocol; samples during this procedure were randomized to account for plate/run variability. Site-specific primer pairs and PCR/pyrosequencing conditions are given below (bolded nucleotides in primer sets indicate insertion of an A or C nucleotide at a variable C/T position due to a CpG site within the primer). All epigenotypes reported are an average of the three replicates.

CpG site -934. Sample amplification via PCR was performed using 0.20 μ M of primers TSL101F

(5'-TTGAGTTTTGGATTTAGATAATTAAGGATT-3') and TSL101R

(5'-biotin-AATAAAATACCTCCCACTCCTTATTCCTAA-3'). Thermal cycling conditions were: Step 1: (95 °C/15 min)/1 cycle; Step 2: (94 °C/30 s, 56 °C/30 s, 72 °C/30 s)/50 cycles; Step 3: (72 °C/10 min)/1 cycle; Step 4: 4 °C hold. Pyrosequencing was then performed using primer TSL101S (5'-AGAAGTTATTTTATAATTTTT-3'). On average, replicate variability deviated from the mean \pm 1.50%.

CpG site -860. Sample amplification via PCR was performed using 0.20 μ M of primers TSL104F

(5'-GTAGTTTAGAAAGTTTTGGAATTTTTGATT-3') and TSL104R

(5'-biotin-AATAAAATACCTCCCACTCCTTATTCCT-3'). Thermal cycling conditions identical to those used for CpG site -934. Pyrosequencing was performed using primer TSL104S (5'-AGTTTTGGAATTTTTGATTTG-3'). On average, replicate variability deviated from the mean \pm 1.55%.

2.1.4 Social attribution task

The present analyses used data from a social attribution paradigm^{145,146} performed in the fMRI scanner (one of several functional tasks in the full protocol, completed in a quasi-random, counterbalanced fashion). In this task, 16 animations were shown to participants for approximately 16 seconds each: these stimuli contained three

white geometric shapes (a triangle, a diamond, and a circle) and an empty white box centered on a black background. Half the stimuli presented the shapes as characters engaging in social, goal-directed behaviors (e.g. playing hide-and-seek, dancing, etc.); the other half displayed random motion, with the shapes bouncing around the screen like billiard balls. These “animate” and “random” stimuli alternated for the duration of the task. On average, overall motion vectors (speed and amount of motion) were conserved across conditions. Participants were simply instructed to observe the shapes as they moved along the screen—no overt responses were required, but debriefing confirmed that participants differentiated between stimulus types and attempted to infer the shapes’ behaviors during animate trials.

2.1.5 fMRI acquisition and preprocessing

All imaging procedures were conducted on a 3T Siemens Magnetom Tim Trio MRI system using a standard 12-channel head coil at the UVA Fontaine Research Park. In an effort to minimize participant motion, the head was secured using plastic paddles on each side of the coil; foam cushions were additionally inserted into the remaining space around the shoulders and neck. Functional MR data were acquired via T_2^* -weighted single shot gradient echo, echo planar imaging sequences sensitive to the BOLD contrast (TR = 2 s; TE = 40 ms; FA = 90°) with generalized autocalibrating partially parallel acquisitions (GRAPPA). Whole-brain coverage was collected in 28 interleaved slices (4.2 mm slice thickness; 3 × 3 mm in-plane resolution) parallel to the AC-PC line. The social attribution task consisted of 118 volumes plus several dummy scans to allow for steady-state magnetization. High-resolution anatomical images were collected using a T_1 -weighted magnetization prepared rapid gradient echo (MPRAGE) sequence (TR = 1.9 s; TE = 2.53 ms; FA = 9°; 176 slices; 1 mm thickness).

Initial preprocessing was performed using the Statistical Parametric Mapping 8 software (SPM8, Wellcome Trust Centre for Neuroimaging, London) in Matlab. Functional data were first realigned and unwarped to correct for participant head motion. The mean motion-corrected image was then coregistered to the high-resolution anatomical image. All scans were normalized to the Montreal Neurological Institute template (MNI152) using both affine and nonlinear transformations; functional volumes were resampled to $3 \times 3 \times 3$ mm voxels and were registered according to the transformation parameters derived from the anatomical normalization. An 8 mm full-width at half-maximum (FWHM) isotropic Gaussian kernel was subsequently applied to smooth the functional data.

Prior to functional connectivity analyses, additional preprocessing was performed using in-house Matlab scripts. We first applied global signal scaling (median = 1,000) to account for transient fluctuations in signal intensity across space/time. We then extracted the residual BOLD signal from each voxel after removing the effect of head motion. Motion was modeled based on the Friston-24 approach, which includes six translation/rotation parameters, their temporal derivatives, and the squares of each set¹⁴⁷. This allowed us to account for both time-lagged and nonlinear effects of motion on the BOLD signal.

2.1.6 Functional connectivity estimation

Functional network nodes were defined by parcellating the cerebrum into 90 anatomically defined regions of interest according to the widely-used automated anatomical labeling (AAL) atlas¹⁴⁸. Given that some AAL regions are large (and may therefore have highly-heterogeneous voxelwise responses), a summary timecourse was extracted for each region by taking the first eigenvariate within each functional volume^{149,150}. We then decomposed the timeseries into several frequency bands

using a maximal overlap discrete wavelet transform (MODWT): in accordance with previous uses of this filtering approach^{151,152}, the low-frequency fluctuations in wavelet scale two (0.06-0.12 Hz) were selected for subsequent connectivity analyses. Thus, each participant yielded a 118×90 matrix of regional timeseries, \mathbf{X} .

Next, we constructed a 90×90 functional association matrix, \mathbf{A} , where each element $A_{i,j}$ (i.e. a network edge) indicated the strength of association between regional timeseries \mathbf{x}_i and \mathbf{x}_j , computed as magnitude-squared coherence. Coherence is a method for estimating linear time-invariant relationships between signal timeseries. As a function of the cross-power spectrum between two signals, it offers several advantages: 1) estimation of frequency-specific covariances; 2) simple interpretability (values are normalized to the $[0, 1]$ interval); and 3) robustness to regional differences in the hemodynamic response function, which otherwise introduce time-lag confounds to connectivity estimates via Pearson correlation¹⁵³. At a given frequency, ω , the coherence between two regional timeseries, \mathbf{x}_i and \mathbf{x}_j , is:

$$\gamma_{\mathbf{x}_i\mathbf{x}_j}^2(\omega) = \frac{|\mathbf{S}_{\mathbf{x}_i\mathbf{x}_j}(\omega)|^2}{\mathbf{S}_{\mathbf{x}_i\mathbf{x}_i}(\omega)\mathbf{S}_{\mathbf{x}_j\mathbf{x}_j}(\omega)}. \quad (2.1)$$

Here, $\mathbf{S}_{\mathbf{x}_i\mathbf{x}_j}$ is the cross-spectral density between \mathbf{x}_i and \mathbf{x}_j , while $\mathbf{S}_{\mathbf{x}_i\mathbf{x}_i}$ and $\mathbf{S}_{\mathbf{x}_j\mathbf{x}_j}$ are the auto-spectral densities of \mathbf{x}_i and \mathbf{x}_j , respectively. These were estimated using the high-resolution minimum variance distortionless response (MVDR)^{154,155}. Ultimately, for each pair of regions, the mean coherence value was taken within our frequency band of interest (0.06-0.12 Hz). Accompanying p -values were computed using an F -distribution, according to convention¹⁵⁶. Because this pairwise estimation process involved a total of 4,005 comparisons, all association matrices were submitted to an FDR correction ($q < .05$). Any elements of \mathbf{A} that did not meet the multiple comparisons threshold were set to zero.

In addition to FDR thresholding, we applied a range of proportional thresholds to each association matrix, examining the top 50% of network edges to the top 10%

of edges in 5% intervals (**Figure A.1**). Such thresholding practices are common in functional connectivity analyses to determine how the apparent topology of a network changes when filtering out weaker links^{157–159}. For our subsequent pattern analyses, this was especially important to consider: lower thresholds (e.g. the 50th percentile) may still contain noisy connections that artificially inflate our network metrics; conversely, more stringent thresholds (e.g. the top 10%) may deflate estimates across much of the brain, leaving little information for pattern identification. Network topology metrics and subsequent statistical models were therefore estimated for each threshold.

Brain network quantification. Whole-brain network topology was characterized using several common graph theoretic metrics included in the Brain Connectivity Toolbox (BCT)¹⁶⁰. We first obtained the *degree* of each node in the network. Nodal degree is simply the total number of nonzero edges connected to a node. We then computed nodal *strengths*, or the sum of all edge weights connected to a node. Finally, we estimated *eigenvector centrality* across nodes. In general, nodal “centrality” measures directly quantify the importance of each node in the system, such that highly central nodes act like hubs which variously direct or coordinate information flow across the network. Eigencentrality is formally defined via eigendecomposition of the thresholded association matrix, \mathbf{A} :

$$\mathbf{A}\mathbf{V} = \boldsymbol{\lambda}\mathbf{V}, \quad (2.2)$$

where $\boldsymbol{\lambda}$ is a diagonal matrix of eigenvalues and \mathbf{V} is a matrix of \mathbf{A} ’s right eigenvectors. The eigencentrality for each node is contained in the column eigenvector, \mathbf{v} , corresponding to the largest positive eigenvalue in $\boldsymbol{\lambda}$. Thus, similar to principal component reduction, nodes with high eigencentrality can be thought to explain more “variance” in global connectivity across the network by providing paths to other central nodes. *Network hubs* in this sense are therefore defined statistically

from the data—not based on prior functional/anatomical labels (e.g. default mode network regions).

It is worth noting that nodal degree, strength, and eigencentrality all attempt to characterize the presumptive influence of each brain region in the network (and are therefore likely to be positively correlated). Importantly, however, a node with many connecting edges (high degree) may have low overall strength if its numerous links are weak. Similarly, high nodal eigencentrality does not necessitate that a node is also high in degree and strength—a node may in fact have few edges linking it to other nodes, but it could nevertheless be considered central if those edges link to other highly-connected brain regions. Because the choice of network metric may produce nontrivially dissimilar characterizations of system topology, it is important to consider a number of measures when applying graph theory to functional connectivity data.

2.1.7 Multivariate pattern analysis: Relevance vector regression

In an effort to decode individual differences in *OXTR* methylation from multivariate patterns of network topology, we employed a sparse Bayesian learning technique: relevance vector regression (RVR), implemented in Matlab using the SparseBayes software, v2.0^{161,162}. A key advantage to RVR is its exploitation of the marginal likelihood to achieve a sparse solution to the prediction problem. Moreover, predictions are made by integrating over probability distributions, and model hyperparameters do not need to be optimized through computationally intensive cross validation routines; rather, they are learned directly from the data. Data from Study 1 were used in these analyses, and models were trained/tested per combination of $\{threshold, metric, CpG\}$.

For each model, training inputs were given as a set of *feature vectors*, $\{\mathbf{f}_n\}_{n=1}^N$, with

corresponding continuous *targets*, $\mathbf{t} = [t_1, \dots, t_N]^T$, where N was the total number of training examples. More specifically, feature vectors were comprised of network statistics (degrees, strengths, or eigencentralities) derived from the 90-region AAL atlas, and the target vector gave each participant's methylation level for a given CpG site. RVR formulates the target vector as the sum of an approximation vector, $\mathbf{y} = [y(\mathbf{f}_1), \dots, y(\mathbf{f}_N)]^T$, and an error vector, $\boldsymbol{\epsilon}$:

$$\mathbf{t} = \mathbf{y} + \boldsymbol{\epsilon} = \Phi \mathbf{w} + \boldsymbol{\epsilon}. \quad (2.3)$$

Notably, the approximation vector represents a linear combination of *weights*, $\mathbf{w} = [w_1, \dots, w_M]^T$, and an $N \times M$ design matrix, Φ , whose rows were comprised of feature vectors from each participant. M here refers to the number of nodes in the network. RVR treats the columns of Φ as a set of *basis functions*; thus, unlike many other machine learning methods, RVR is not inherently a dual-form kernel technique. Given our sufficiently large sample size, we elected to train models on the primal representation of Φ rather than compressing features to a linear kernel space, which compromises the sparseness of RVR.

Under the conventional assumption of independent and identically distributed errors (with variance σ^2), RVR specifies a multivariate Gaussian likelihood over the target data:

$$p(\mathbf{t}|\mathbf{w}, \sigma^2) = (2\pi)^{-\frac{N}{2}} \sigma^{-N} \exp \left\{ -\frac{\|\mathbf{t} - \mathbf{y}\|^2}{2\sigma^2} \right\}. \quad (2.4)$$

A vector of *hyperparameters*, $\boldsymbol{\alpha} = [\alpha_1, \dots, \alpha_M]^T$, modulates the prior distribution over \mathbf{w} (also Gaussian in form):

$$p(\mathbf{w}|\boldsymbol{\alpha}) = (2\pi)^{-\frac{M}{2}} \prod_{m=1}^M \sqrt{\alpha_m} \exp \left(-\frac{\alpha_m w_m^2}{2} \right). \quad (2.5)$$

Put differently, the value of a hyperparameter, α_m , models uncertainty about the corresponding weight parameter value, w_m . Given the target data, \mathbf{t} , and the hyperparameters, $\boldsymbol{\alpha}$, Bayes' rule allows us to represent the posterior conditional

distribution over \mathbf{w} :

$$p(\mathbf{w}|\mathbf{t}, \boldsymbol{\alpha}, \sigma^2) = \frac{p(\mathbf{t}|\mathbf{w}, \sigma^2)p(\mathbf{w}|\boldsymbol{\alpha})}{p(\mathbf{t}|\boldsymbol{\alpha}, \sigma^2)}. \quad (2.6)$$

The weight posterior is multivariate Gaussian with covariance

$$\boldsymbol{\Sigma} = (\mathbf{H} + \sigma^{-2}\boldsymbol{\Phi}^T\boldsymbol{\Phi})^{-1} \quad (2.7)$$

and mean

$$\boldsymbol{\mu} = \sigma^{-2}\boldsymbol{\Sigma}\boldsymbol{\Phi}^T\mathbf{t}, \quad (2.8)$$

where \mathbf{H} is a diagonal matrix containing model hyperparameters, $\boldsymbol{\alpha}$.

The goal of RVR is to identify “most-probable” point estimates, $\boldsymbol{\mu}_{MP}$, for the parameters, \mathbf{w} . This is accomplished by maximizing the (log) marginal likelihood of the posterior conditional with respect to model hyperparameters (i.e. type-II maximum likelihood estimation):

$$\begin{aligned} \mathcal{L}(\boldsymbol{\alpha}) &= \log p(\mathbf{t}|\boldsymbol{\alpha}, \sigma^2) = \log \int_{-\infty}^{\infty} p(\mathbf{t}|\mathbf{w}, \sigma^2)p(\mathbf{w}|\boldsymbol{\alpha})d\mathbf{w} \\ &= -\frac{1}{2} (N \log(2\pi) + \log |\mathbf{C}| + \mathbf{t}^T \mathbf{C}^{-1} \mathbf{t}), \end{aligned} \quad (2.9)$$

where covariance $\mathbf{C} = \sigma^2\mathbf{I} + \boldsymbol{\Phi}\mathbf{H}^{-1}\boldsymbol{\Phi}^T$ (\mathbf{I} gives the identity matrix). The algorithm initializes by identifying a “best aligned” basis function—this is the column vector (network node) in $\boldsymbol{\Phi}$ with the largest normalized projection onto \mathbf{t} . The crux of RVR and sparse Bayesian learning is then a sequential addition/deletion of network nodes to the model until the likelihood objective converges. For each iteration, a candidate node, ϕ_m , is selected and model *quality* (q_m^2) and *sparsity* (s_m) parameters are updated. In short, these represent a tradeoff between error reduction (quality) and redundancy (sparsity). The gradient of the marginal likelihood at α_m is reflected by the “relevance factor,” θ_m :

$$\theta_m \triangleq q_m^2 - s_m. \quad (2.10)$$

If the relevance factor is positive (i.e. the increase in fit outweighs the cost in sparsity), ϕ_m may be added to the model or retained if it is already present; conversely, if the criterion is zero or negative (i.e. the cost in sparsity matches or outweighs the increase in fit), ϕ_m will be deleted or left out. We then update the noise parameter estimate (σ^2) along with model-level statistics and repeat until convergence. Critically, any basis function may be re-added or deleted at any step if doing so improves the marginal likelihood. In this way, we continually increase model evidence while also ensuring that we identify the network nodes most relevant to the final prediction function. Once this optimal solution has been converged upon, we derive μ_{MP} for the weight vector via Equations 2.7 and 2.8 and may estimate the most-probable value for new target data, t_* (given a new vector of inputs, ϕ_*):

$$t_* = y_* = \phi_* \mu_{MP}. \quad (2.11)$$

The ability of RVR to predict percent methylation on *OXTR* was tested using leave-one-subject-out cross-validation (LOSO-CV). For each fold of LOSO-CV, an individual row vector of network statistics was removed from Φ (along with the corresponding target value in \mathbf{t}). Data were mean-centered according to the remaining training examples, the model was fit, and a predicted methylation level was obtained for the left-out subject. This ultimately yielded a vector of predicted methylation values, \mathbf{t}_* .

We quantified accuracy across CV folds using two measures: 1) the correlation between actual and predicted methylation values (*prediction correlation*) and 2) average model loss (root mean squared error; *RMSE*). These performance statistics were each compared against empirical distributions of plausible accuracies, generated through 1,000 iterations of nonparametric permutation testing. For each iteration, the target vector was randomly permuted, the entire LOSO-CV procedure was performed, and accuracy statistics were recorded. For prediction correlation,

p -values were given as the fraction of cases in which permuted model accuracy was higher than the “true” model; for $RMSE$, p -values reflected the fraction of cases in which permuted model error was lower.

Subnetwork identification. Because RVR performs automatic feature selection, we sought to determine whether a core “subnetwork” of brain regions was consistently identified as relevant to predicting *OXTR* methylation. For each model $\{threshold, metric, CpG\}$, weight vectors were averaged across CV folds and unit normalized. We then collected all model weight vectors for a given $\{metric, CpG\}$ and computed “relevance probabilities” for each region (i.e. the probability of nonzero weight across all 10 threshold levels). Regional relevance probabilities were averaged across network metrics within each methylation site, allowing us to determine which regions were consistently deemed relevant across all threshold levels and network metrics. In order to avoid bias toward either methylation site, a subnetwork was conservatively identified by selecting nodes which were relevant over 75% of the time for either CpG -934 or CpG -860—this pared down the original 90-region network to a 43-region subnetwork. We then re-estimated network metrics based solely on connectivity across these areas and re-ran the RVR procedure above (still based on the large Study 1 sample).

Independent generalization. After confirming the subnetwork improved overall predictive performance, the data from Study 2 were used for further model testing. We applied each model’s average weight vector (derived from Study 1 participants) to the Study 2 data. Thus, we could directly assess the generalizability of our models to an independent sample of participants. Model error ($RMSE$) was recorded and significance was determined via 1,000 iterations of nonparametric permutation testing.

2.1.8 Brain data visualization

Multivariate weight maps from each model were averaged over CV folds and unit normalized. These were projected onto a cortical surface using the Surf Ice software (<https://www.nitrc.org/projects/surfice/>). Subnetwork regions were mapped using the BrainNet Viewer (<https://www.nitrc.org/projects/bnv/>)¹⁶³.

2.2 Results

2.2.1 DNA methylation on *OXTR*

Percent DNA methylation was assessed at *OXTR* CpG sites -934 and -860. Within each site, there were no significant differences in methylation between the two samples (**Figure 2.1**). Collapsing across samples, methylation was generally much higher on CpG -934 ($M = 46.88 \pm 6.27$ *SD*) relative to CpG -860 ($M = 25.99 \pm 5.73$ *SD*), $t(174) = 38.23, p < .0001$, two-tailed; however, there was still a positive association between sites, $r(173) = 0.28, p = .0002$, two-tailed. Consistent with previous work, we observed a sex effect on CpG -934 such that women ($M = 48.26 \pm 6.88$ *SD*) were significantly more methylated on average than men ($M = 45.39 \pm 5.19$ *SD*), $t(173) = 3.10, p = .002$, two-tailed. No such differences were observed on CpG -860: $t(173) = 1.41, p = .162$, two-tailed. Age was not a significant predictor of methylation on either CpG -934 [$r(173) = -0.04, p = .623$, two-tailed] or CpG -860 [$r(173) = -0.02, p = .832$, two-tailed]. Finally, and importantly, participant head motion (mean framewise displacement) did not correlate with methylation on either CpG -934 [$r(173) = -0.10, p = .169$, two-tailed] or CpG -860 [$r(173) = -0.004, p = .961$, two-tailed], which suggests that associations between connectivity and methylation are unlikely to be an artifact of motion-corrupted imaging data¹⁶⁴.

2.2.2 Multivariate pattern analyses

A first pass using the full 90-region network demonstrated that multivariate patterns of network topology significantly predicted *OXTR* methylation. This held for all three network metrics, although prediction success varied depending on methylation site and network threshold (**Figure 2.2**; see also **Tables A.1 and A.2**). Performance was highly significant for CpG site -860 across several thresholds ranging from the top 35% to the top 20%, with peak performance at the 30% threshold. Models also significantly predicted methylation on CpG site -934 with performance peaking between the top 40% and top 35% thresholds.

Subnetwork modeling. A visual inspection of the multivariate weight maps derived from the models above demonstrated remarkable consistency in the regions selected by RVR (**Figure A.2**). This was despite clear changes in overall network topology (the degree distribution) across threshold levels (**Figure A.1**). We therefore calculated the probability of each node being included across models (**Figure 2.3A**; see also **Tables A.3 and A.4**) and defined a 43-region subnetwork: these core nodes were relevant in over 75% of the models for either CpG site -934 or CpG site -860 (**Figure 2.3B**).

Following subnetwork definition, we then re-calculated network metrics based on subnetwork connectivity and re-ran the RVR procedure. Feature reduction generally offered increased performance relative to the full 90-region network: CpG -934 enjoyed the largest benefit in overall error reduction, but CpG -860 continued to yield the highest accuracies overall (**Figure 2.4**; see also **Tables A.5 and A.6**). Unlike the whole-brain models, however, it was less clear which thresholds offered peak predictive performance (**Figures 2.2, 2.4**). A number of network metrics still saw an increase in predictive power around the top 30% and top 25% thresholds; however, some metrics (e.g. strengths for CpG -860) yielded significant prediction

performance for weak and stringent thresholds alike. For all metrics and both methylation sites, RVR revealed a widely-distributed network of nodes ranging from dorsal anterior regions of the brain to ventral posterior regions (**Figure 2.5**). Interestingly, some regions selected by RVR were lateralized by methylation site (e.g. the negative weights over postcentral gyrus, see **Figure 2.5**), but the non-independence of multivariate weights precludes extensive local inference.

Model testing on independent data. Finally, we sought to directly test generalizability of the subnetwork models by applying them to an independent dataset. Weight vectors for each model $\{threshold, metric, CpG\}$ were applied to the corresponding subnetwork data obtained from the smaller Study 2 sample. Given the inevitably-vast amount of individual variation in brain data, most models did not significantly generalize to new examples. However, eigencentality continued to significantly predict OXTR methylation on CpG site -934 (**Figure 2.6**). This was largely threshold-invariant (**Table 2.1**), but the best-generalizing thresholds also yielded the highest performance for eigencentality in the original subnetwork models (**Figure 2.4**), suggesting that processes such as DNA methylation may play a critical role in shaping the spatial organization of task-related network hubs.

2.3 Discussion

In this experiment, we used a combination of imaging epigenetics and statistical machine learning to demonstrate that inter-individual variability in social task-related network architecture reflects epigenetic variation in *OXTR*. We presented this first in a large sample using cross validation before demonstrating that it is possible to generalize these models to an independent set of individuals. Although we have previously shown that *OXTR* methylation covaries with regional BOLD activity and seed-based connectivity during social-cognitive tasks^{99,100}, to our knowledge, this is

Network threshold	$RMSE$ (p)
FDR	6.83 (.051)
Top 50%	6.75 (.035)
Top 45%	6.75 (.031)
Top 40%	6.67 (.017)
Top 35%	6.70 (.016)
Top 30%	6.76 (.020)
Top 25%	6.73 (.011)
Top 20%	6.87 (.062)
Top 15%	7.29 (.298)
Top 10%	7.50 (.585)

Table 2.1: Independent model fit: Eigencentality on CpG site -934. Model error ($RMSE$) after applying Study 1 subnetwork models to Study 2 data (p -values derived from 1,000 iterations of nonparametric permutation testing).

the first study to show that individual differences at the microscale molecular-level can be *decoded* from patterns of macroscale network connectivity. The Bayesian learning approach used here allowed us to probe these relationships without forcing prior anatomical or regional assumptions on the data (cf. seed-based connectivity).

2.3.1 Functional relevance of subnetwork regions

Automated feature selection is central to relevance vector machine learning. This process was highly-reliable in our analyses, with RVR consistently identifying a subnetwork of regions across threshold levels and network metrics. However, given that many AAL partitions cover relatively large anatomical areas, it is critical to assess the *functional* relevance of our subnetwork nodes. The regions selected by RVR largely comprised a network of areas commonly implicated in various types of social information processing, including the insula, fusiform gyrus, superior temporal sulcus, temporoparietal junction, and inferior frontal gyrus^{82,145,165}. More recent work has extended this network to include other regions found in our subnetwork, such as the caudate, premotor cortex, and precuneus¹⁶⁶. Thus, the

feature selection implemented by RVR successfully identified regions that are functionally relevant for social cognition. While it is possible we would have observed more nuanced weight distributions (or a more nuanced subnetwork) with a more fine-grained atlas, our method of signal extraction (taking the first eigenvariate within an ROI) can mitigate anatomical/functional variability across individuals by capturing the spatial dimension along which maximal variance in signal is accounted for. In other words, it is unlikely that task-related activations will be expressed in precisely the same way for each individual, and the eigenvariate will return the principal signal component regardless of where, exactly, those voxels are in the ROI.

With respect to our earlier studies relating *OXTR* methylation to social task-related activity^{99,100}, we find considerable overlap between those clusters and our subnetwork nodes—these include many of the areas listed above as well the amygdala and dorsal anterior cingulate. Although we hesitate to draw overly-localized inferences from our multivariate maps, it is worth noting that many (but *not all*) of these regions are weighted *negatively*, such that decreased connectivity predicts higher methylation. This offers an interesting perspective on our previous work, which consistently demonstrated *positive* relationships between *OXTR* methylation and regional BOLD activity: increased levels of task-related activity may, in certain cases, reflect weaker connectivity to other network nodes (as a function of endogenous access to oxytocin), requiring these areas to “work harder” on their own.

2.3.2 Network threshold and metric considerations

In general, most models suffered declines in performance at very weak (e.g. raw FDR) and very stringent (e.g. top 10%) network thresholds. In the former case, this

is likely a result of too much noise across the network; in the latter case, connectivity density may have been too low for RVR to detect informative patterns. For both the 90-region network and 46-region subnetwork, a “sweet spot” in performance tended to emerge around the top 30% threshold. At these levels, the degree distribution of the network began to reflect a power-law form characteristic of so-called “small-world” organization, where most nodes have few direct connections to one another, instead relying on central hubs to quickly propagate information across the network. Many biological systems—including the brain—indeed demonstrate small-world organization¹⁶⁷⁻¹⁷¹. Thus, thresholding the network to an increasingly small-world state effectively optimized our ability to find relationships between connectivity and methylation, removing superfluous, noisy edges that clouded the identification of underlying topological patterns. Although higher thresholds (e.g. top 10%) appear most similar to classical small-world networks, we suspect that RVR was unable to find informative patterns when most nodes were disconnected from one another.

With regard to graph theoretic metrics, nodal degree tended to predict methylation better than nodal strength and eigencentrality, both in the whole-brain 90-region network and the 46-region subnetwork. Degree is ostensibly a crude measure of connectivity (simply a count of connected links, without considering weight), but prior work has shown that nodes with high degree also tend to correspond with central hub-like nodes: the knockout of these high-degree nodes in the brain compromises network function and may directly contribute to a number of psychopathological states^{167,172,173}. Although a wealth of research has sought to identify functional and structural hubs in brain networks¹⁷⁴, in the present study, we defined hubs in a data-driven, empirical fashion using nodal eigencentrality—this allowed us to identify central nodes that emerged purely as a function of our task.

Given that hubs are generally thought to enable efficient communication across network components, it is perhaps not coincidental that eigencentality was the only metric able to generalize to an independent dataset. We suggest that individual variation in DNA methylation may mediate the spatial development of a functional network, including the extent to which various regions are integrated with one another. These results further bolster an exciting, emerging body of research showing network connectivity to be a stable intrinsic trait within individuals (across tasks, rest, etc.)¹⁷⁵⁻¹⁷⁷: here, system architecture—or the topology of network hubs—offers an informative endophenotype for one's underlying molecular makeup, which together translate into the complex phenotypes that define us as individuals.

2.3.3 Implications for oxytocin action and social behavior

It is well-established that oxytocin is critical for a number of social and affiliative behaviors. However, mounting evidence suggests that genetic/epigenetic variation in *OXTR* may specifically contribute to individual differences in social-behavioral phenotypes by modulating the functional neuroanatomy of a number of brain regions⁸³. Such a mechanism is supported by recent work showing that cellular-level networks display similar organization to macroscale cortical networks¹²⁹. Thus, the cytoarchitectural effects of genetic/epigenetic variation may cascade upwards to large-scale functional network organization. Currently the full downstream consequences of methylation on CpG sites -934 and -860 are unknown: more molecular work is needed to elucidate their specific functions. While the observed differences in weight maps may indicate non-overlapping roles for these sites, prediction success in both CpG -934 and CpG -860 suggests they are each likely to contribute to differences in multiscale network topology.

A compelling hypothesis suggests that social deficit disorders (such as the

autism spectrum) are due to early-life dysfunction of the oxytocin system, which otherwise supports social learning¹⁰¹. In this view, oxytocin amplifies the salience of social information in the environment, allowing individuals to construct generative models of the social self—this, in turn, enables the predictive coding mechanisms necessary to engage in social inference and effectively navigate the social world. Indeed, animal research has shown that oxytocin enhances neural signal-to-noise and promotes neural plasticity through long-term potentiation^{5,6}. In autistic children, a recent study has further shown that intranasal oxytocin acutely strengthens seed-based connectivity from the amygdala and ventral striatum to networks supporting social perception and motivation⁹. There is also evidence that differential expression of *OXTR* is predicted by early life experiences¹³⁵. Together, these studies suggest that early oxytocin dysfunction obstructs the development of brain systems that support healthy social cognition. We therefore suggest that our ability to decode *OXTR* methylation from social task-related network architecture may reflect variable neurodevelopmental trajectories, spurred by epigenetic limits on oxytocin's action. The predictive value of nodal centrality in particular further indicates that oxytocin may support the coupling of brain networks that predispose individuals to social behavior. Again, this is of special relevance to autism spectrum disorders which are commonly characterized by higher levels of *OXTR* methylation⁶³ and hypoconnectivity in functional brain networks^{131,132}—however, because the present study included only neurotypical adults, future longitudinal work is needed to clarify the role of *OXTR* methylation in brain network development and social behavior over time.

2.4 Figures

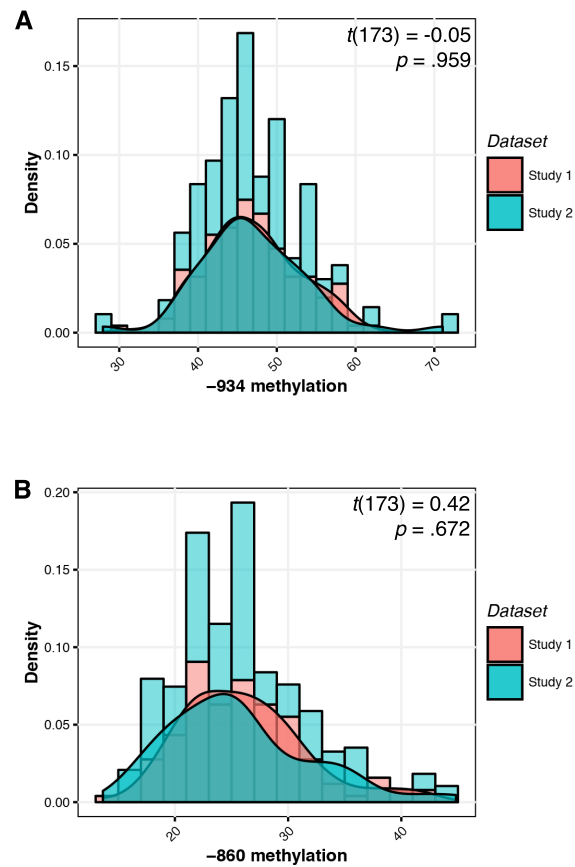


Figure 2.1: OXTR methylation by CpG site and sample. **A**, Distribution of percent methylation values for CpG site -934. **B**, Distribution of percent methylation values for CpG site -860. In both **A** and **B**, Study 1 samples ($N = 127$) are shown in light red while Study 2 samples ($N = 48$) are shown in light blue. No differences in mean methylation were observed between samples.

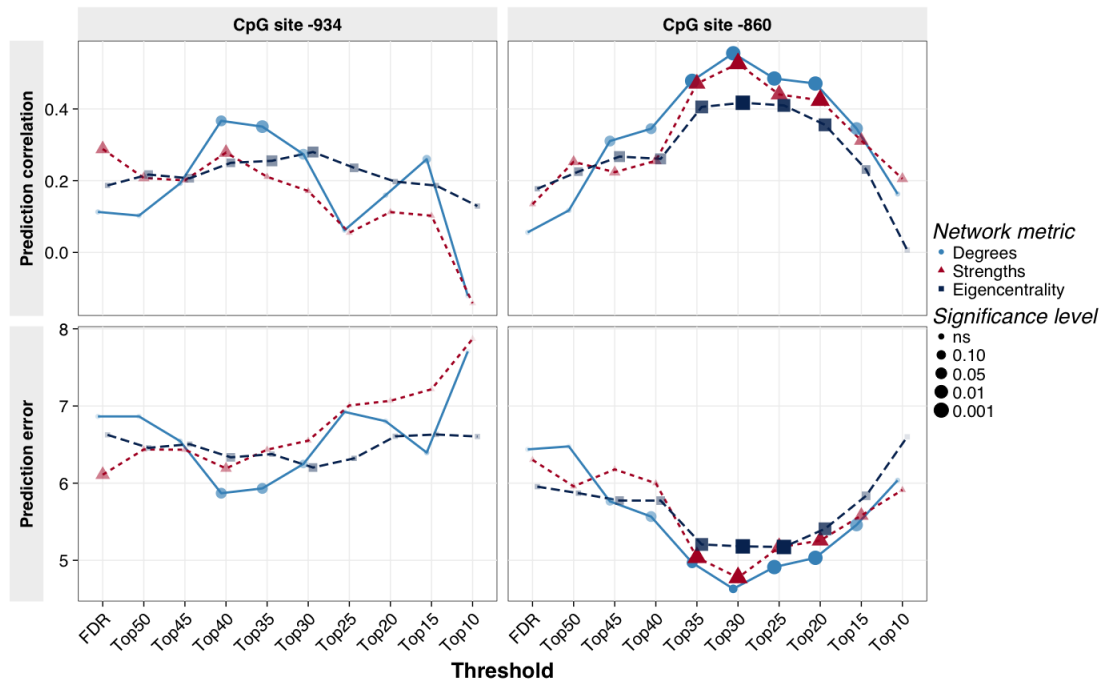


Figure 2.2: Results of relevance vector regression by threshold, metric, and CpG site. Model performance for the full 90-region network (see also **Table S1**), trained/tested on the Study 1 sample ($N = 127$). Left panels give prediction accuracies for CpG site -934; right panels give accuracies for CpG site -860. Performance summarized using both Pearson correlations (actual vs. predicted methylation; *top*) and model error (*RMSE*; *bottom*). Point size indicates significance derived from 1,000 iterations of nonparametric permutation testing; similarly, darker shading indicates smaller p -values (shading is scaled by $-\log(p)$).

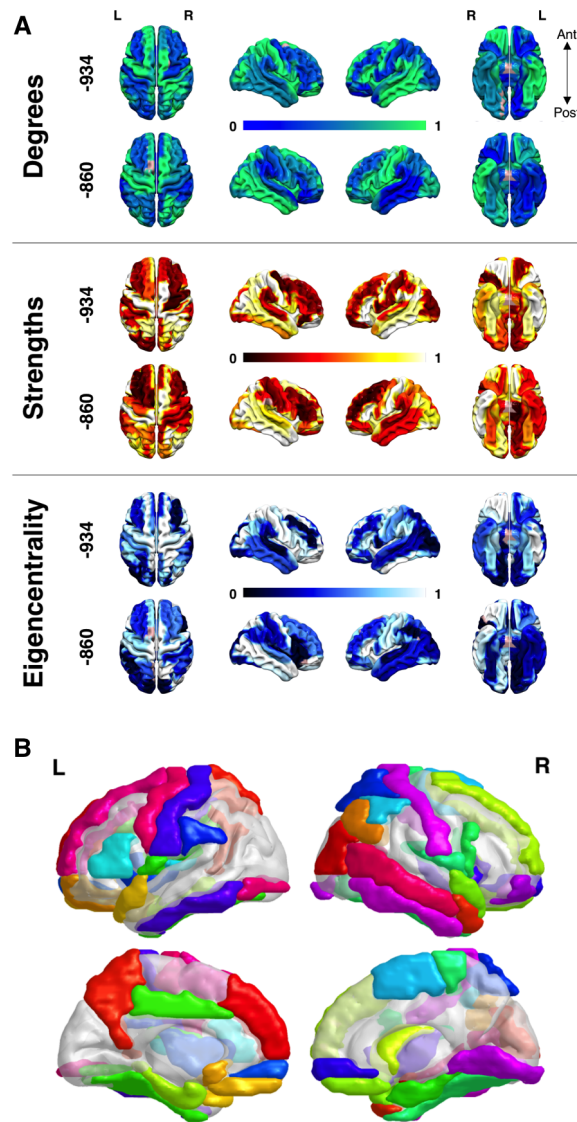


Figure 2.3: Relevance probabilities and subnetwork map. **A**, Regional relevance probabilities for each network metric and methylation site (models trained/tested on Study 1 data). Brighter colors indicate higher probabilities of model inclusion across all 10 threshold levels. **B**, Reduced subnetwork of anatomically-defined nodes, relevant in more than 75% of all models for either site.

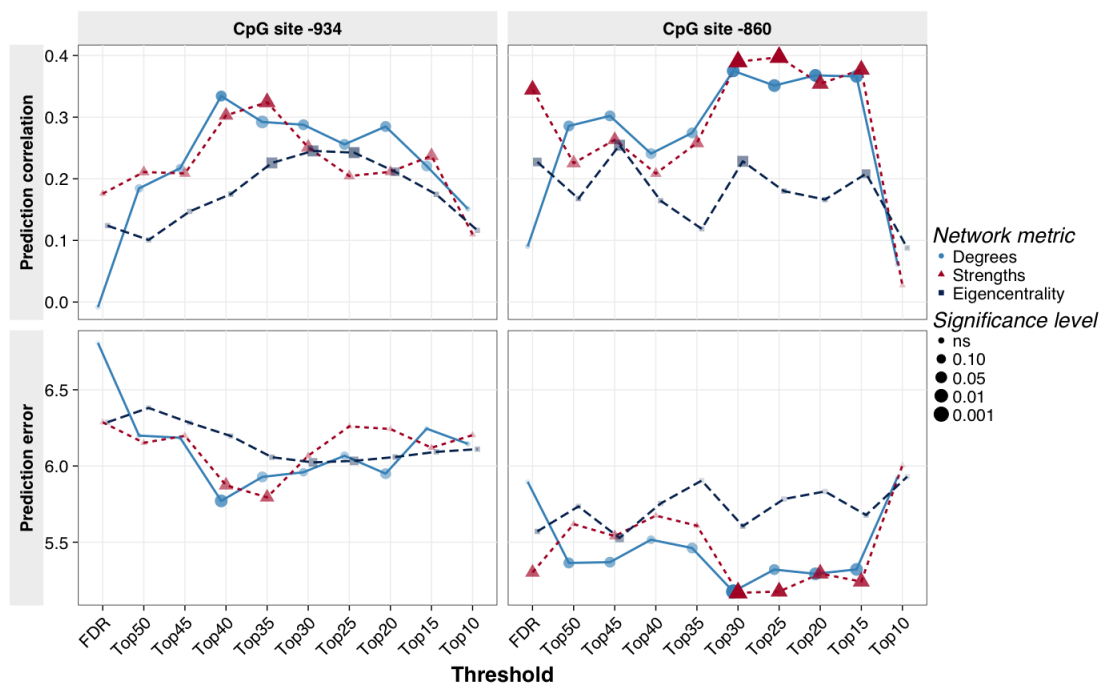


Figure 2.4: Subnetwork RVR performance. Model performance (prediction correlation, *top*, and prediction error, *bottom*) for the 43-region subnetwork (see also **Table S3**), trained/tested on the Study 1 sample. Point size and shading schemes are identical to **Figure 2.2**.

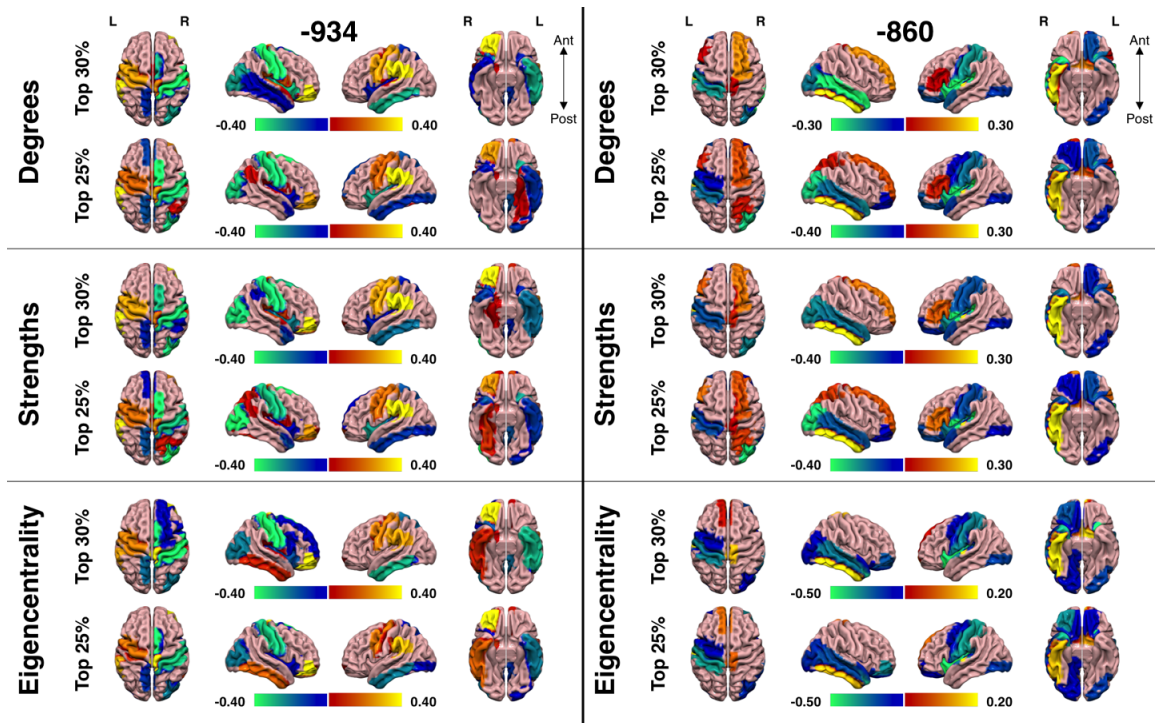


Figure 2.5: Multivariate weight maps derived from subnetwork relevance vector regression models. Relevance vector regression analyses on the 43-region subnetwork revealed spatially-distributed sets of brain regions relevant for predicting individual differences in *OXTR* methylation. Models were trained and tested using data from Study 1 ($N = 127$). For both CpG site -934 (*left*) and CpG site -860 (*right*), weight maps are provided at the top 30% and top 25% connectivity thresholds. Values reflect average weights across CV folds (with unit normalization). Note that exact local inference is inappropriate given the non-independence of multivariate weights—nevertheless, “hot” colors push the prediction function towards higher expected methylation (with increased connectivity) while “cool” colors indicate the reverse.

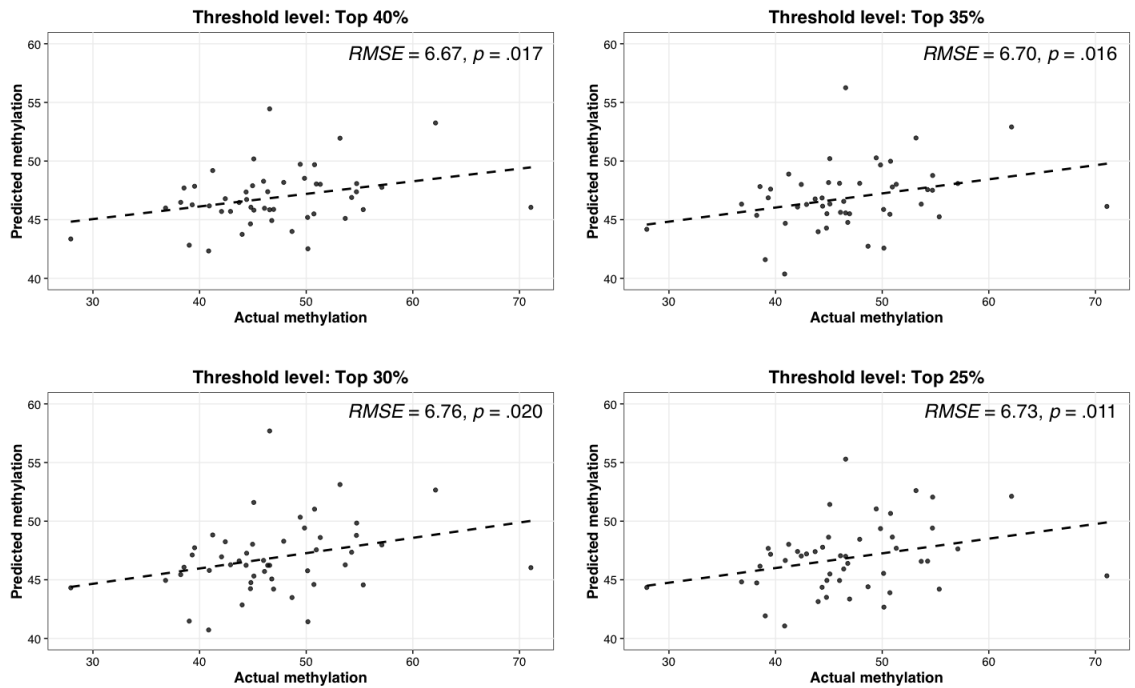


Figure 2.6: Subnetwork eigencentality models generalize to new data. Applying the subnetwork models derived from Study 1 to data from Study 2 ($N = 48$) significantly predicted *OXTR* methylation on CpG site -934—this was largely threshold-invariant, but we provide the four best-fitting thresholds here. Prediction accuracy is given as model error ($RMSE$), and p -values were derived through 1,000 iterations of nonparametric permutation testing.

Chapter 3

Experiment 2

While Experiment 1 focused on task-related associations with *OXTR* methylation, we now shift our focus to the resting state. Recently, variability intrinsic to the BOLD signal has received attention as an informative measure in its own right^{178–180}. Studies on the effects of intranasal OT have suggested that oxytocin may enhance synchronous temporal variability⁷ (i.e. functional connectivity), but to date, no research has specifically examined how oxytocin might modulate baseline signal fluctuations themselves—whether in terms of variability, power, or other signal processing characteristics. Animal models, however, have identified a key role for oxytocin in modulating neural SNR in the rodent hippocampus, simultaneously amplifying signal and decreasing spontaneous background firing⁶. Thus, the primary aim of this study was to explore the potential relationships between intrinsic BOLD dynamics and endogenous access to oxytocin in humans.

We hypothesized that multivariate patterns of BOLD variability—particularly within networks relevant for social cognition (e.g. the default mode network—will index DNA methylation on *OXTR*. Given that there is no previous research relating intrinsic BOLD dynamics to molecular markers, we consider a host of variability metrics ranging across temporal, spectral, and information theoretic domains. We

also employ both whole-brain and network-specific machine learning models to examine spatial heterogeneity in the relationships between BOLD variability and *OXTR* methylation. Results provided mixed support for our hypothesis: the best-performing models were localized to subcortical-cerebellum and higher-order visual processing networks, *not* systems classically associated with overt social behavior. Nevertheless, we find that endogenous access to oxytocin may indeed modulate baseline oscillatory patterns across the whole-brain and within specific networks.

3.1 Materials and Methods

3.1.1 Participants

For the current analyses, data were drawn from 61 participants previously referred to as the Study 2 sample (**Section 2.1.1**). One individual was excluded for non-Caucasian descent; one individual was excluded for providing incomplete methylation data; and an additional 9 were excluded for excessive head motion during the resting-state fMRI scan (mean framewise displacement ≥ 0.50 mm and/or a single frame of motion ≥ 3 mm). The sample was therefore comprised of 50 individuals (24 men, 26 women; $M_{age} = 20.78 \pm 2.64$ *SD*, range = 18-30). All participants provided written informed consent for a protocol approved by the University of Virginia IRB (Protocol 15051; Principal Investigator, Jessica J. Connelly).

3.1.2 Blood collection and epigenotyping

We again report percent DNA methylation on *OXTR* CpG sites -934 and -860. Blood collection, DNA extraction, and epigenotyping procedures were identical to those described in Experiment 1 (see **Section 2.1.2** and **Section 2.1.3**).

3.1.3 Resting-state fMRI acquisition and preprocessing

All imaging procedures were conducted on a 3T Siemens Magnetom Tim Trio MRI system using a standard 12-channel head coil at the UVA Fontaine Research Park. In an effort to minimize participant motion, the head was secured using plastic paddles and foam cushions within the head coil. High-resolution anatomical images were collected using a T_1 -weighted magnetization prepared rapid gradient echo (MPRAGE) sequence (TR = 1.9 s; TE = 2.53 ms; FA = 9°; 176 slices; 1 mm thickness). Prior to collecting task-related functional MR data (not the focus of this experiment), we collected resting-state fMRI via a T_2^* -weighted multiband echo planar imaging (mbEPI) sequence sensitive to the BOLD contrast (TR = 1 s; TE = 32 ms; FA = 90°; acceleration factor = 4). Whole-brain coverage was collected in 40 interleaved slices (3 mm slice thickness; 3 × 3 mm in-plane resolution). A total of 500 volumes were acquired over approximately 8.5 minutes: during this time, participants were simply instructed to lay still with their eyes open—a fixation cross was presented on a projector screen in the back of the scanner, but participants were otherwise free to let their minds wander.

We performed standard preprocessing procedures using the SPM8 software in Matlab. Steps were identical to those described in Experiment 1 (**Section 2.1.5**), including motion correction (realignment/unwarping), coregistration, normalization, and smoothing.

Resting-state fMRI is particularly susceptible to motion and other MR signal artifacts. Thus, like a connectivity analysis, additional preprocessing is necessary before estimating BOLD variability. Importantly, however, we have previously shown that relationships between BOLD variability and individual difference measures are heavily influenced by different techniques used to deal with motion¹⁸⁰. Our pipeline took a conservative approach to addressing this problem. We first

applied global signal scaling (median = 1,000) to account for transient fluctuations in signal intensity across space/time. The voxelwise BOLD timeseries were then demeaned and detrended to correct for linear signal drift. Next, we employed wavelet despiking—a cutting-edge technique that identifies spectral signatures of head motion and removes them from the signal¹⁸¹. As a final effort to ensure our data were not contaminated by motion artifacts, time-lagged and nonlinear effects of head motion were estimated and removed from voxelwise BOLD timeseries using the Friston-24 approach¹⁴⁷.

3.1.4 Brain parcellation and timeseries extraction

In order to test whether relationships between BOLD variability and *OXTR* methylation are heterogeneous across different functional networks, we partitioned the brain into 268 regions according to the Shen atlas^{176,182–184}. Unlike the anatomically-defined AAL atlas used in Experiment 1, Shen atlas regions are *functionally*-defined and pre-labeled according to one of eight networks (**Table 3.1; Figure 3.1**). In general, this affords a more fine-grained parcellation than the AAL atlas; however, because voxelwise responses within a region are still not guaranteed to be homogeneous, we extracted a summary timecourse per node by taking the first eigenvariate at each timepoint^{149,150}. No subsequent temporal filtering was performed—this ensures that variability estimates are not biased by a limited band of information in the signal.

3.1.5 Quantifying BOLD dynamics

Recent efforts to model intrinsic BOLD variability have employed a number of techniques for quantifying dynamic fluctuations in signal. These can broadly be characterized in terms of *temporal variability*, *spectral variability*, and *dynamic*

Network	N regions	Kernel?
Medial frontal	29	N
Frontoparietal	34	N
Default mode	20	N
Subcortical-cerebellum	90	Y
Motor	50	Y
Visual I	18	N
Visual II	9	N
Visual association	18	N

Table 3.1: Networks of the Shen atlas. Network labels with corresponding numbers of nodes. The far right column indicates whether network data must be compressed to a linear kernel for relevance vector regression (based on the number of ROIs relative to the sample size). See **Figure 3.1** for a visual map.

complexity. Due to the lack of prior investigation into the relationship between these factors and molecular level-variation, we consider the full range of metrics below.

Temporal variability. To assess BOLD dynamics in the time domain, we simply computed the standard deviation (σ_t) of each regional timeseries in accordance with previous work^{178–180,185}.

Spectral variability. Measures of spectral variability rely on Fourier decompositions of the BOLD signal, allowing us to probe the proportion of signal energy represented across different frequencies^{185–187}. According to Parseval’s theorem, for a zero-mean timeseries, \mathbf{x} , realized at timepoints, t :

$$\int x^2(t)dt = \int |\mathcal{F}(\omega)|^2 d\omega, \quad (3.1)$$

where $\mathcal{F}(\omega)$ is the Fourier transform of $x(t)$ at frequency, ω . Variance in the frequency domain, σ_ω^2 , is then given by the following set of equalities:

$$\sigma_\omega^2 = \lim_{T \rightarrow \infty} \frac{1}{T} \int_{-\frac{T}{2}}^{\frac{T}{2}} x^2(t)dt = \lim_{T \rightarrow \infty} \frac{1}{T} \int |\mathcal{F}(\omega)|^2 d\omega = \int \Phi(\omega)d\omega. \quad (3.2)$$

Here, $\Phi(\omega)$ is the *power spectral density* of the signal at frequency, ω . We can therefore take the integral over the entire range of frequencies as a general measure of spectral variance (this is equivalent to estimating the *total spectral power* of the BOLD signal).

Additional measures of spectral variability commonly focus on low-frequency ranges (e.g. 0.01-0.10 Hz) thought to reflect intrinsic network function^{185,186,188}. Evaluating the integral of $\Phi(\omega)$ over this band yields an estimate of *low-frequency power* (LFP). Higher estimates of regional LFP (relative to the total power of the signal) would suggest that BOLD fluctuations carry neurally-relevant information—this ratio is known as the *fractional amplitude of low-frequency fluctuations* (fALFF) and is thought to index neural signal-to-noise¹⁸⁷.

In the present analyses, we estimated the full spectral variance (σ_{ω}^2) of regional BOLD timeseries, LFP, and fALFF. In concordance with connectivity analyses in Experiments 1 and 3, LFP (and consequently fALFF) was derived from low frequency fluctuations in the range of 0.06-0.12 Hz.

Dynamic complexity. Finally, we considered the *entropy* of regional BOLD signals. Entropy is commonly understood in colloquial terms as “disorder” or “chaos”—in this context, entropy is a statistical phenomenon that quantifies the amount of *information* in a signal over time. Nevertheless, it can be conceptualized along similar lines. Like chaotic physical systems, complex signals carry an inherent degree of uncertainty: knowledge of previous system states may not guide expectations for present states (vs. a sine wave which is perfectly predictable given sufficient information about its past states). It then follows (perhaps counterintuitively) that stable, predictable signals have *low* information content; greater uncertainty/complexity increases the information in a signal and thus its entropy.

The entropy of physiological timeseries can be quantified using measures such as *approximate entropy* (ApEn) its extension, *sample entropy* (SampEn)—the technical

minutiae of each have been previously described in detail^{189–191}. In short, both measures rely on a *window parameter* (m) and a *tolerance parameter* (r). These transform the timeseries into a set of discrete matched (1) and mismatched (0) states over time—states “match” if patterns of activity across contiguous windows (defined by m) are similar within some distance criterion (r). Entropy is then the probability of similar patterns of activation over time. There is some evidence that SampEn provides more stable estimates of entropy regardless of timeseries length^{189,191}; however, both measures have successfully been used to characterize the complexity of neural signals over time^{192–194}.

We estimate both ApEn and SampEn using parameter settings recommended in prior work—specifically, we set $m = 2$ and $r = 0.25 \times MAD$ (where MAD is the *median absolute deviation* of the regional timeseries)^{189,191–194}.

3.1.6 Multivariate pattern analysis: Bayesian efficient multiple kernel learning

To examine the relationships between *OXTR* methylation and patterns of whole-brain BOLD variability (measured using the metrics defined above), we used Bayesian efficient multiple kernel learning (BEMKL)^{195,196}, implemented in Matlab—this approach allowed us to specify whole-brain models while determining the relative importance of BOLD variability in each network of the Shen atlas. Similar to the relevance vector analyses described in Experiment 1 (see **Section 2.1.7**), BEMKL can be used to obtain probabilistic, sparse solutions to the prediction problem; however, BEMKL differs from RVR in two important respects. First, while RVR does not require the use of kernels, BEMKL necessitates compressing data into a kernelized feature space. Second, BEMKL does not encode sparsity through automated relevance detection—rather, it is manually manipulated via a

priori hyperparameter settings. Models were trained and tested using standard cross-validation and permutation procedures per combination of $\{metric, CpG\}$.

For a given BOLD variability measure, data were partitioned into M individual $N \times P_m$ feature matrices, $\{\mathbf{X}_m\}_{m=1}^M$, corresponding to each of the eight Shen networks (N gives the number of training examples and P_m indicates the number of regions that comprised a given network, m). We then computed a simple $N \times N$ linear kernel for each feature matrix:

$$\mathbf{K}_m = \mathbf{X}_m \mathbf{X}_m^T. \quad (3.3)$$

where each element $K_{m|i,j}$ indicated the similarity (i.e. the dot product) between two feature vectors, $\mathbf{x}_{m|i}$ and $\mathbf{x}_{m|j}$.

The decision function is formally defined using a multi-kernel extension of classic dual-form machine learning:

$$\mathbf{t} = \boldsymbol{\alpha}^T \left(\sum_{m=1}^M \beta_m \mathbf{K}_m \right) + b. \quad (3.4)$$

Here, \mathbf{t} is an $N \times 1$ vector of continuous *targets* (i.e. methylation values for a given CpG site); $\boldsymbol{\alpha}$ is an $N \times 1$ vector of *sample weights* (invariant across kernels); β_m is a *kernel weight* describing the contribution of \mathbf{K}_m ; and b is a *bias* term.

While BEMKL specifies a fully-conjugate probabilistic model for the data, exact inference is analytically intractable (again in contrast to RVR). Estimation is instead performed using a deterministic variational approximation that places a lower bound on the marginal likelihood, factoring out posterior distributions for each parameter in an effort to model their joint distribution. The mathematics underlying this procedure are dense and described in detail elsewhere^{195,196}; therefore, we omit a complete description here.

Before model estimation, however, BEMKL requires setting a series of hyperparameters that define prior distributions over the weight parameters. We denote

the prior over sample weights using $\gamma \sim \mathcal{G}(\gamma)$ and the prior over kernel weights using $\omega \sim \mathcal{G}(\omega)$. Note these are gamma-distributed, which allows for simulating either ℓ_1 (sparse) or ℓ_2 (nonsparse) norms over the weights by manipulating the shape and scale parameters of the prior distribution. Given our relatively-small sample size, we specified a nonsparse prior over the sample weights to retain as much information from each input as possible: $\gamma = (1 \times 10^{-10}, 1 \times 10^{-10})$. Sparsity was instead encoded into kernel weights in an effort to identify networks most strongly driving the final prediction function: $\omega = (1 \times 10^{-10}, 1 \times 10^{10})$.

Each BEMKL model was trained and tested using leave-one-subject-out cross-validation (LOSO-CV). For each fold, one individual was removed from the multi-kernel and reserved for testing. The remaining data were then centered and unit normalized to account for differences in the number of ROIs contributing to each kernel. After the model was fit, an approximate-Gaussian predictive distribution was obtained for the left-out data^{195,196}—the mean of this distribution was taken as the maximum-likelihood estimate of methylation for that individual. Overall prediction accuracy was quantitated as model loss (root mean squared error; *RMSE*) over all CV folds. We compared the “true” *RMSE* against an empirical distribution of error, generated over 1,000 iterations of nonparametric permutation testing. As in Experiment 1, this involved shuffling the target vector, performing the full LOSO-CV procedure, and recording the resulting *RMSE*. *P*-values thus reflected the proportion of cases in which permuted model error was lower.

3.1.7 Multivariate pattern analysis: Relevance vector regression

Following whole-brain BEMKL, we used relevance vector regression (implemented in Matlab using SparseBayes, v2.0) to model network-specific relationships between BOLD variability and *OXTR* methylation. We elected to make a second pass with

RVR for two reasons: 1) some networks are small enough so as to not require a kernel (potentially allowing for more sensitive mappings of regional variability to methylation), and 2) whole-brain BEMKL, despite using sparse kernel loadings, may still have been hampered by uninformative features clouding pattern identification.

Of the eight networks in the Shen atlas, only two required computation of a linear kernel (**Table 3.1**): the subcortical-cerebellum network (90 regions) and the motor network (50 regions). Data from the remaining networks were kept in primal form. All models were fully cross-validated (LOSO-CV) and evaluated using nonparametric permutation tests per combination of $\{network, metric, CpG\}$. We have previously described the specification and estimation of RVR models in detail (see **Section 2.1.7**); however, in brief, BOLD variability measures from a given network were used as training inputs while methylation values (from either CpG site -934 or CpG site -860) served as targets for prediction. Regardless of whether inputs were kernelized, a sparse parameter set was derived using sequential type-II maximum likelihood estimation—in this procedure, individual features (i.e. columns of the input matrix) were iteratively tested to determine whether their inclusion in the model improved the overall likelihood of the data. The decision to include or exclude a feature was determined by a “relevance factor,” which captured the tradeoff between error reduction and redundancy relative to other features presently in the model. The critical observation is that we are guaranteed a monotonic increase in model evidence at each step, ultimately yielding a subset of features that are most informative to the prediction problem.

The correspondence between actual methylation values and predictions from LOSO-CV was quantified using *RMSE*. To determine whether model fit was significantly better than chance, we performed 1,000 iterations of nonparametric permutation testing—*p*-values again indicated the probability of “random” models

outperforming the true model.

3.1.8 Brain data visualization

Kernel weights from BEMKL and dual-form RVR were reverse-transformed back into the original space of the data per CV fold, averaged, and unit normalized; primal-form RVR weights were simply averaged and normalized. The resulting multivariate maps from both BEMKL and RVR were projected onto a cortical surface using the Surf Ice software (<https://www.nitrc.org/projects/surface/>). Shen atlas regions were mapped using the BrainNet Viewer (<https://www.nitrc.org/projects/bnv/>)¹⁶³.

3.2 Results

3.2.1 DNA methylation on *OXTR*

Percent DNA methylation was assessed at *OXTR* CpG sites -934 and -860. Results were largely consistent with Experiment 1 (see **Section 2.2.1**). Within-subjects, methylation was significantly higher on CpG -934 ($M = 46.62 \pm 6.93$ *SD*) relative to CpG -860 ($M = 25.93 \pm 6.32$ *SD*), $t(49) = 17.95, p < .0001$, two-tailed. However, there was *not* a significant linear relationship between sites, $r(48) = 0.25, p = .086$, two-tailed. We observed a smaller (albeit significant) sex effect on CpG -934 such that women ($M = 48.54 \pm 7.48$ *SD*) were more methylated on average than men ($M = 44.55 \pm 5.72$ *SD*), $t(48) = 2.10, p = .041$, two-tailed. There was no sex effect on CpG -860: $t(48) = 0.84, p = .406$, two-tailed. Age was also not a significant predictor of methylation on either CpG -934 [$r(48) = -0.08, p = .575$, two-tailed] or CpG -860 [$r(48) = -0.21, p = .143$, two-tailed], and again, participant head motion (mean framewise displacement) did not correlate with methylation on either CpG

-934 [$r(48) = -0.17, p = .252$, two-tailed] or CpG -860 [$r(48) = -0.15, p = .306$, two-tailed].

3.2.2 Whole-brain BEMKL

BEMKL largely failed to identify patterns of BOLD variability that were predictive of *OXTR* methylation (see **Supplementary Table B.1** for the full set of model fit statistics). However, multivariate patterns of spectral variance (σ_{ω}^2) significantly predicted methylation on CpG site -934 ($RMSE = 7.42, p = .047$; **Figure 3.2**). Regional weights were entirely negative, such that more variability predicted decreased methylation. Interestingly, at the kernel level, the model was most strongly driven by variance in the subcortical-cerebellum network ($\beta = 0.50$), which is chiefly comprised of regions that are dopamine-rich (e.g. basal ganglia structures). This was followed by the medial frontal network ($\beta = 0.41$) and the default mode network ($\beta = 0.39$)—both of which span a number of areas relevant for mentalizing and social information processing. The networks with the lowest loadings were mainly sensory (visual I, $\beta = 0.27$, and visual II, $\beta = 0.23$), but the frontoparietal network was also a weak contributor to the decision function ($\beta = 0.26$). Motor regions ($\beta = 0.35$) and visual association regions ($\beta = 0.35$) contributed equally in the mid-range of network loadings.

For CpG site -860, multivariate patterns of fALFF—rather than the full spectral variance, σ_{ω}^2 —significantly predicted methylation ($RMSE = 6.36, p = .006$; **Figure 3.3**). Here, regional weights were almost exclusively positive. This was unexpected given that fALFF is thought to index SNR in the BOLD signal: our model suggests that higher SNR generally predicts increased *OXTR* methylation (i.e. decreased access to endogenous oxytocin). The strongest network loadings were in line with those observed for σ_{ω}^2 on CpG -934, such that subcortical-cerebellum regions

($\beta = 0.54$) and medial frontal regions ($\beta = 0.47$) were the greatest contributors to the decision function. However, unlike the previous model, the default mode network yielded one of the weakest loadings ($\beta = 0.17$), ranking only above the visual association network ($\beta = 0.02$). The frontoparietal network ($\beta = 0.37$), motor network ($\beta = 0.34$), and primary/secondary visual networks (visual I, $\beta = 0.34$, and visual II, $\beta = 0.30$) were all modest contributors.

3.2.3 Network-specific RVR

A more focal examination of network-specific variability yielded a mixed set of results. Most models were not able to accurately predict *OXTR* methylation regardless of metric or CpG site; sensory networks, however, demonstrated relatively strong performance across several metrics within CpG -934. We summarize performance for each network below.

Medial frontal (primal RVR). Although the medial frontal network was highly-weighted in successful BEMKL analyses, models of variability in the primal network space failed to yield significant prediction accuracy across all combinations of $\{metric, CpG\}$ (**Supplementary Table B.2**).

Frontoparietal (primal RVR). Similarly, patterns of frontoparietal variability in primal space did not index *OXTR* methylation on either CpG site (**Supplementary Table B.3**).

Default mode (primal RVR). We also observed no significant relationships between BOLD variability metrics and *OXTR* methylation in the primal space of the default mode network (**Supplementary Table B.4**).

Subcortical-cerebellum (dual RVR). Despite loading the strongest on significant BEMKL models, network-specific analyses across subcortical-cerebellum regions

largely failed to predict *OXTR* methylation (**Supplementary Table B.5**). However, multivariate patterns of low-frequency power accurately predicted percent methylation on CpG site -860 ($RMSE = 6.03, p = .016$; **Figure 3.4**). Weights were positive across the network such that greater LFP was associated with higher levels of methylation—this was similar to the above BEMKL model which associated a *greater proportion* of LFP (fALFF) with increased methylation on CpG -860. Here, fALFF trended towards significance but was outperformed by LFP alone ($RMSE = 6.39, p = .071$).

Motor (dual RVR). Baseline variability across the motor network did not predict methylation on either CpG site (**Supplementary Table B.6**).

Visual I (primal RVR). The primary visual network additionally yielded null performance for each metric and CpG site (**Supplementary Table B.7**).

Visual II (primal RVR). Multivariate patterns of dynamic complexity in the secondary visual network—both approximate and sample entropy—significantly predicted *OXTR* methylation on CpG site -934 (**Figure 3.5; Supplementary Table B.8**). ApEn ($RMSE = 6.55, p = .007$) fit slightly better than SampEn ($RMSE = 6.63, p = .016$). Notably, both models were exceedingly sparse: RVR selected two regions as relevant for ApEn and one region as relevant for SampEn (out of nine in the network). For ApEn, predictions were driven by variability in the left lingual gyrus and right middle occipital gyrus—both negatively weighted, such that increased variability predicted decreased methylation. Similarly, SampEn was driven by a negative weight in the right middle occipital gyrus.

Low-frequency power also significantly predicted percent methylation on CpG site -934 (**Figure 3.6**); however, the effect was weaker than that of entropy ($RMSE = 6.82, p = .049$).

Visual association (primal RVR). Finally, multivariate patterns of temporal and

spectral variability (σ_t and σ_ω^2 , respectively) were significantly associated with *OXTR* methylation on CpG -934 (**Supplementary Table B.9**). Fit was trivially better for σ_ω^2 ($RMSE = 6.20, p = .001$; **Figure 3.7**) relative to σ_t ($RMSE = 6.30, p = .002$; **Figure 3.8**). Interestingly, the regions selected by RVR were primarily right-lateralized, which follows previous work suggesting hemispheric asymmetries in social perception—specifically, that non-verbal social cues are dominantly processed in the right hemisphere¹⁹⁷.

3.3 Discussion

The purpose of this experiment was to explore potential associations between BOLD dynamics and epigenetic variability in the oxytocin system, using a number of common metrics across distributed functional networks. Previous animal models have suggested that oxytocin modulates neural signal-to-noise⁶—perhaps in concert with dopaminergic systems that regulate the gain of neural signals^{27,41,42,44}. However, until now, no studies have attempted to determine whether oxytocin is related to SNR or baseline functional dynamics more broadly in humans. In part, this may be due to measurement uncertainty: it is unclear how accurately we can quantify peripheral concentrations of the peptide itself⁹⁸. We suggest that epigenetic markers such as *OXTR* methylation may circumvent this issue, providing a measure of endogenous access to oxytocin independent of actual peptide levels. Moreover, given that social deficit disorders are commonly associated with OT receptor deficiencies⁶³ and “noisy brains,”¹³⁰ the current investigation offered a means of linking these observations together, identifying which functional systems might be impacted by decreased access to oxytocin.

Our data-driven approach employed whole-brain and network-specific machine learning models in an effort to identify spatial patterns of variability that informed

epigenetic differences. While an increasing number of studies have suggested that BOLD variability is more than mere noise^{178–180,185}, few models were able to identify consistent, patterned structure in the data, yielding only partial support for our hypothesis that *OXTR* methylation might impact baseline system dynamics at the macroscale. There are several reasons why this may have occurred.

First, we have previously shown that associations between BOLD variability and individual difference measures are highly influenced by different preprocessing pipelines¹⁸⁰. It is possible that some of our methods (e.g. wavelet despiking) removed relevant variability from the signal; however, an exhaustive comparison of different preprocessing pipelines was beyond the scope of the current analyses. Second, the BOLD signal is a crude measure relative to cellular-level electrophysiology—consequently, the effects of oxytocin on neuronal SNR may be muddled when measuring a broad, vascular process such as BOLD. Third, the nature of this experiment was to model *noise*, which is theoretically random and normally-distributed across the brain (according to the assumptions of many statistical analysis techniques in neuroimaging). While there may be focal, regional associations between BOLD variability and individual difference measures, an attempt to find coherent, spatially-distributed structure may simply be an uphill battle. Nevertheless, we observed a number of significant relationships between measures of BOLD dynamics and *OXTR* methylation, both at the whole-brain and network-specific level, suggesting that endogenous access to oxytocin may indeed modulate the baseline functioning of macroscale networks.

3.3.1 Evidence for oxytocin-dopamine interactions

Although it was not possible for us to directly measure levels of dopaminergic activity in the brain, several of our models demonstrated strong associations between

OXTR methylation and spectral variability in the subcortical-cerebellum network. The nodes of this system are densely packed across regions that are both dopamine-rich and innervated by oxytocin neurons, such as the ventral striatum and other basal ganglia structures^{27,34}. Thus, our ability to decode *OXTR* methylation from this network may reflect differences in baseline oscillatory function, driven by interactions between oxytocin and dopamine. The strongest effects were observed within CpG site-860, but methylation on both sites may still have downstream consequences for the function of this network.

A landmark study in nonhuman primates demonstrated that spontaneous, low-frequency BOLD fluctuations were strongly correlated with underlying neuronal spike patterns¹⁹⁸. Perhaps not surprisingly then, metrics accounting for low-frequency dynamics (LFP and fALFF) were the most predictive of *OXTR* methylation, but general spectral variance may also be a relevant measure. A broad class of dopaminergic neurons exhibit tonic firing patterns absent of stimulation, but afferent modulation of these systems can shift firing modes into phasic or burst states^{199,200}. There is increasing evidence to suggest that stimulation of mesolimbic oxytocin causes downstream stimulation of dopaminergic cells, inducing dopamine release and driving socio-sexual behaviors associated with joint oxytocin-dopaminergic action⁵¹; however, to our knowledge, there is limited electrophysiological work detailing how oxytocin might modulate the firing states of dopaminergic neurons. A pair of studies have shown that oxytocin modulates tonic and bursting firing patterns of dopaminergic neurons in the hypothalamus, but these effects were primarily in service of lactation^{201,202}.

Nevertheless, it remains a possibility that *OXTR* methylation affects the extent to which oxytocin modulates firing in dopaminergic neurons. Suppose that greater endogenous access to oxytocin enables more diffuse regulation of baseline firing

states: this might produce more variability in the expression of tonic vs. bursting vs. phasic firing across mesolimbic dopamine neurons. As a consequence, we might expect more variability in the power spectrum of the BOLD signal across these regions (assuming that spontaneous BOLD fluctuations do, in fact, reflect neuronal spike patterns¹⁹⁸). This would be in line with our BEMKL model which associated increased spectral variability with decreased *OXTR* methylation. However, if oxytocin generally serves to promote synchronous activity^{6,7,128}, the opposite trend is likely to emerge: rather than more variable spike patterns, oxytocin may encourage time/phase-locked spiking in a specific frequency range. Whole-brain BEMKL and subcortical-cerebellum RVR models suggested that greater degrees of LFP and fALFF predicted higher levels of *OXTR* methylation—but according to animal research, oxytocin may actually *decrease* slow, spontaneous spiking and enhance synchronous fast-spiking activity⁶, consistent with our observations (which associated low-frequency fluctuations with decreased access to oxytocin).

3.3.2 Oxytocin, social perception, and predictive coding

Contrary to expectation, networks classically associated with social cognition (e.g. the medial frontal and default mode networks) did not predict *OXTR* methylation on their own. The best predictors in network-specific RVR models—aside from subcortical-cerebellum regions—were instead associated with higher-level visual processing. Approximate and sample entropy in the secondary visual network both significantly predicted epigenetic variability on CpG site -934; similarly, temporal and spectral variability in the visual association network also predicted methylation on CpG -934. On average, whole-brain entropy measures were not correlated with either temporal or spectral variability measures (**Supplementary Table B.10**), suggesting that they capture unique functional characteristics of the BOLD signal

(temporal and spectral variability, by contrast, were very highly correlated).

The small size of the secondary visual network (nine regions) and extreme sparsity of the resulting models (driven by a mere one or two regions) means results should be interpreted with caution. Perhaps more interesting was the strongly right-lateralized effect observed in the visual association network. In general, higher-order visual areas in the right hemisphere are thought to support processing of nonverbal social cues¹⁹⁷. Previous work has also associated *OXTR* polymorphisms with differential activity in lateral occipital cortex during emotional face processing²⁰³, and we have further shown that lateral occipital activity covaries with methylation on CpG site -934 when viewing emotional faces¹⁰⁰.

The regions selected by RVR extended from lateral occipital cortex into ventral temporal regions—components of the “visual *what* stream” associated with rapid processing of visual emotional stimuli²⁰⁴. We suggest that our results reveal differences in the baseline function of predictive coding systems underlying emotional inference and social cognition. Recall that social-emotional inputs from the environment travel in a bottom-up fashion through sensory systems before being integrated and interpreted by top-down cortical networks—in order to avoid prediction error, the bottom-up system is required to generate a *precise* neural representation of the external stimulus^{104,124}. We previously posited that oxytocin plays a central role in coordinating activity to generate such a representation: therefore, individual differences in oxytocin action may modulate stimulus-free “preparatory” states, similar to tonic firing of dopamine neurons. Maintaining a coherent baseline then makes it possible for high-fidelity information transfer given stimulus-evoked excitation of the system—another putative function of oxytocin^{6,128}. This hypothesis could be illuminated in future studies using more temporally-sensitive measures such as electrophysiology, providing higher-resolution estimates of the relationship

between *OXTR* methylation, baseline variability, and task-evoked processing of social-emotional information.

3.4 Figures

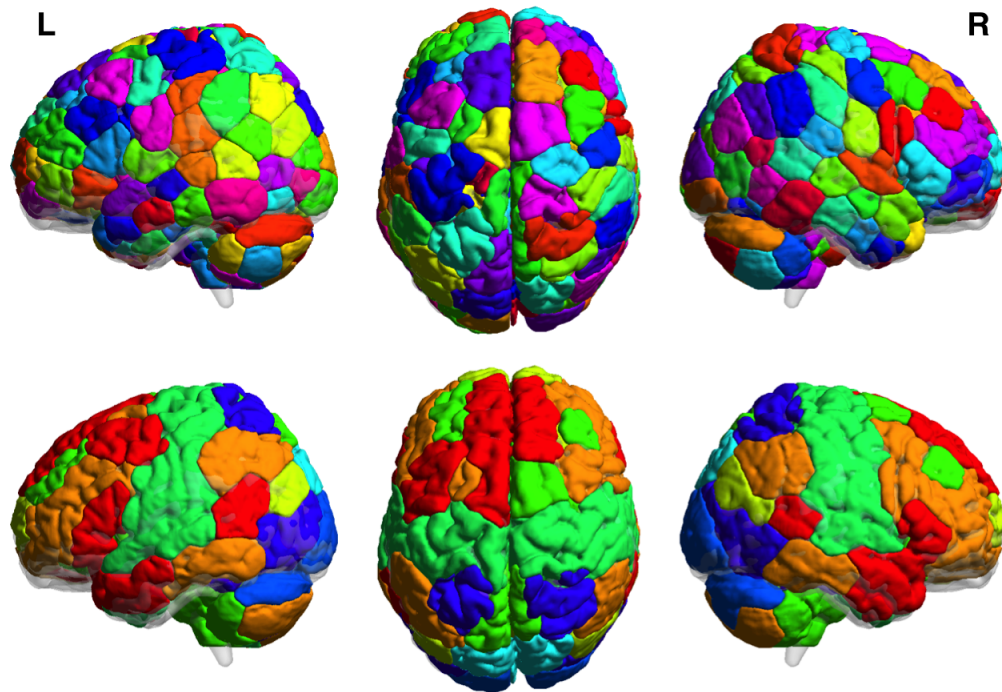


Figure 3.1: Shen atlas partitions. The 268 individual regions of the Shen atlas (*top*) are further partitioned into 8 functional networks (*bottom*). See **Table 3.1** for network labels and sizes (i.e. number of nodes).

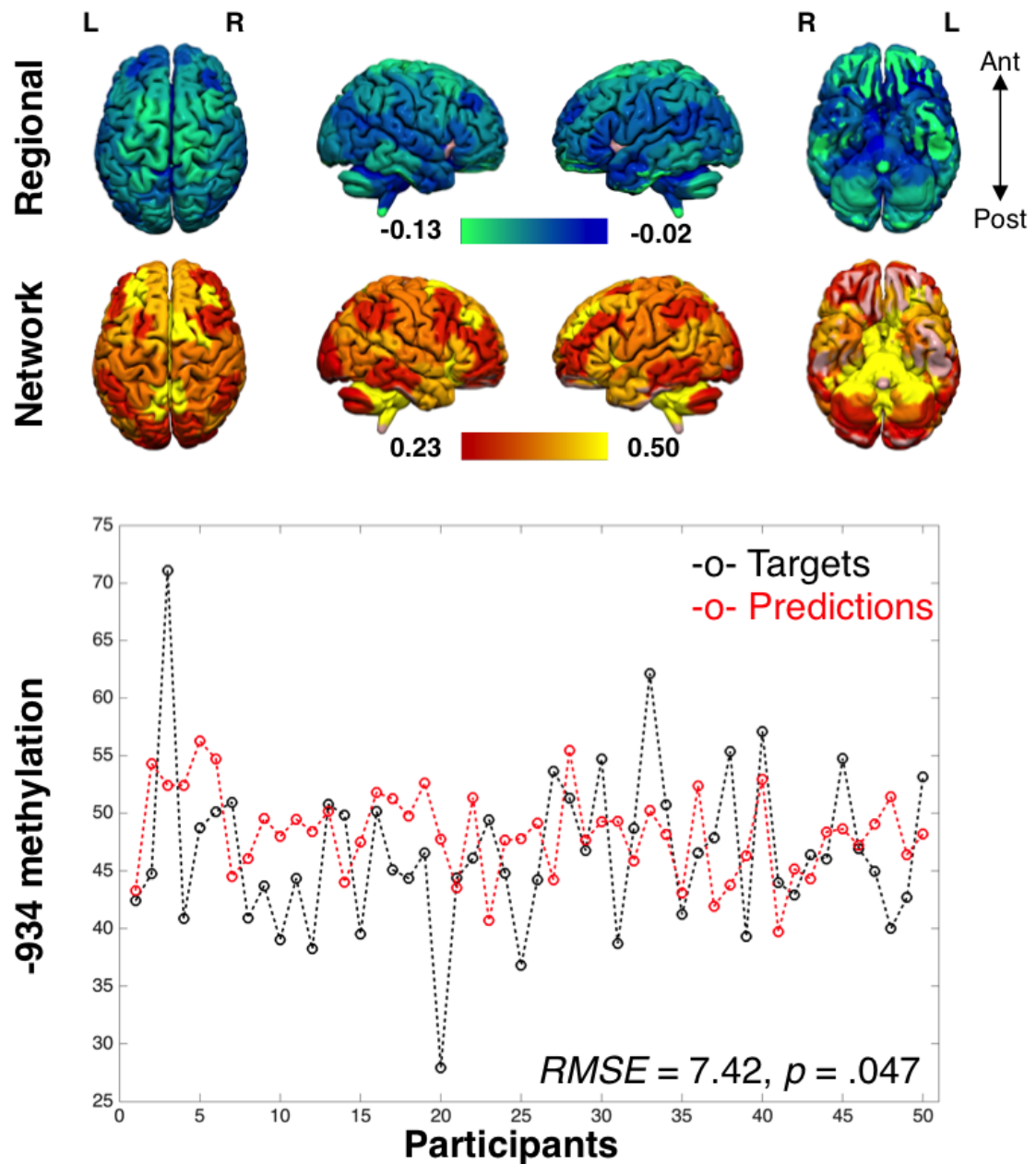


Figure 3.2: Multivariate patterns of spectral variance across the whole brain predict *OXTR* methylation on CpG site -934. Average, unit-normalized weight maps from whole-brain BEMKL analyses are given for individual regions (*top*) and networks (*middle*). In general, increased spectral variability predicted decreased methylation. The bottom panel displays the correspondence between actual methylation values (*black*) and model predictions values (*red*). See **Table B.1** for a full summary of model fit for all variability metrics at the whole-brain level.

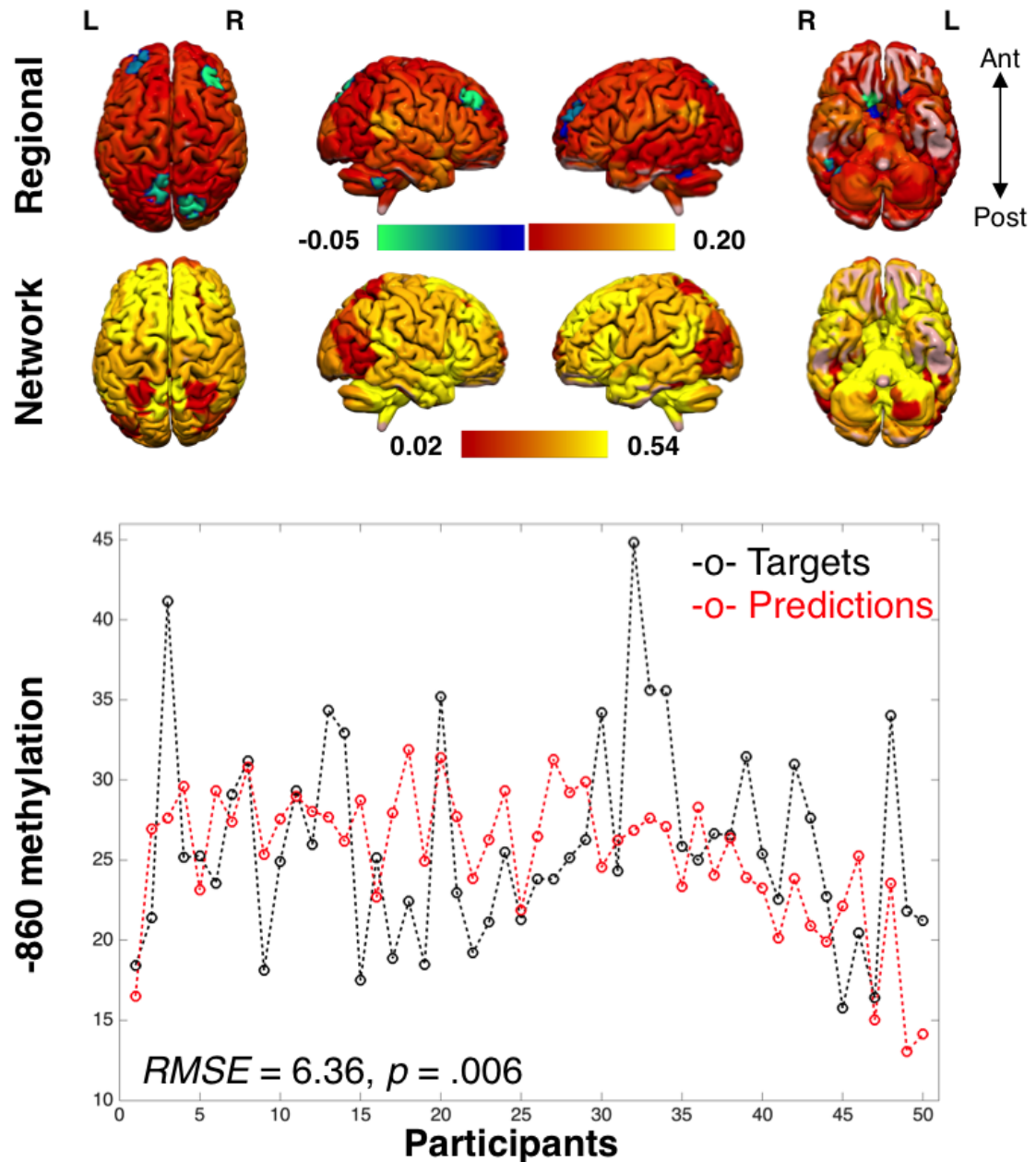


Figure 3.3: Multivariate patterns of fALFF across the whole brain predict *OXTR* methylation on CpG site -860. Average, unit-normalized weight maps from whole-brain BEMKL analyses are given for individual regions (*top*) and networks (*middle*). Although some regions were weighted negative,, an increased proportion of low-frequency power across the brain (relative to the full signal power spectrum) generally predicted increased methylation. The bottom panel displays the correspondence between actual methylation values (*black*) and model predictions (*red*). See **Table B.1** for a full summary of model fit for all variability metrics at the whole-brain level.

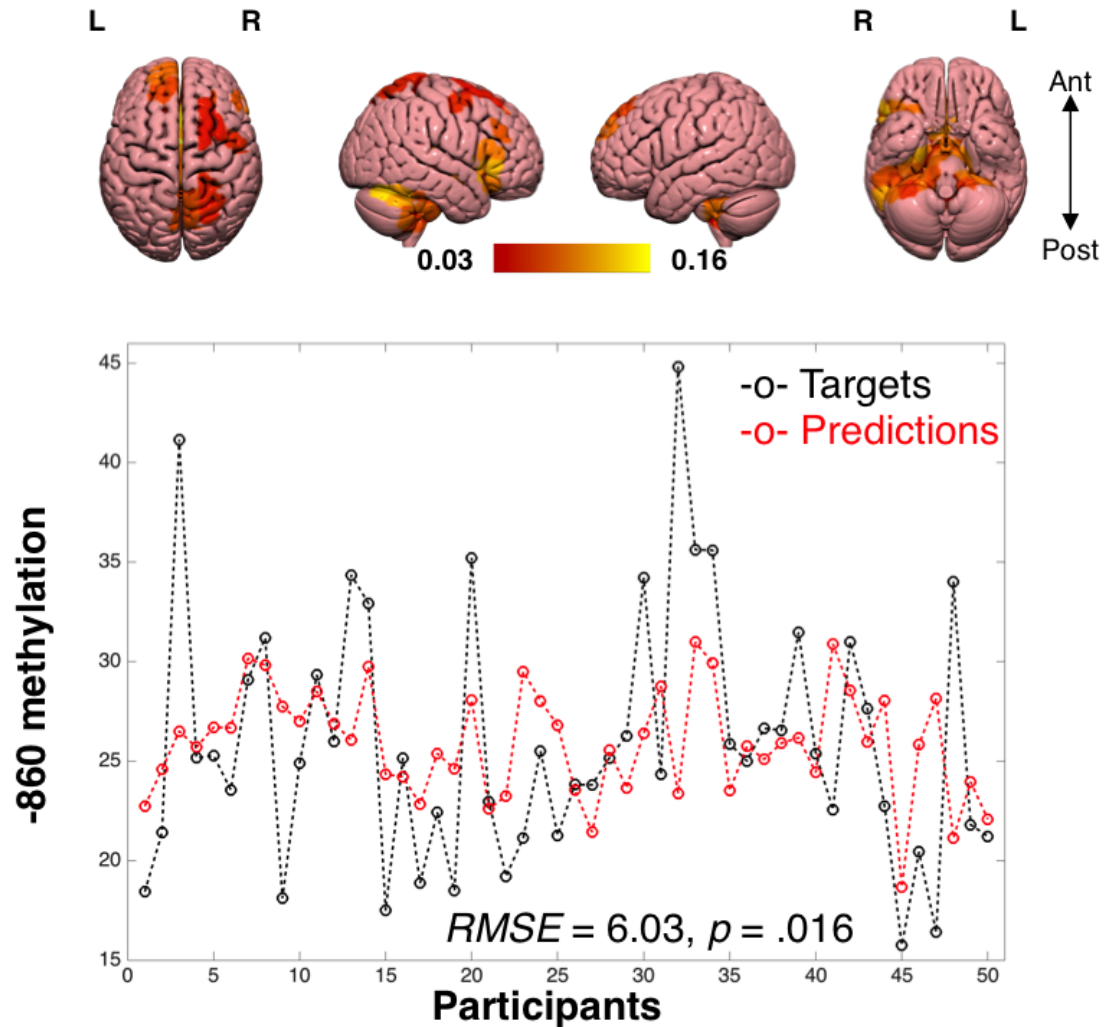


Figure 3.4: Multivariate patterns of LFP in the subcortical-cerebellum network predict *OXTR* methylation on CpG site -860. Network-specific RVR in the subcortical-cerebellum network suggested that greater levels of low-frequency power were associated with increased methylation (weight maps, *top*, are averaged and unit-normalized). The bottom panel displays the correspondence between actual methylation values (*black*) and model predictions (*red*). See **Table B.5** for a full summary of model fit for all variability metrics in subcortical-cerebellum analyses.

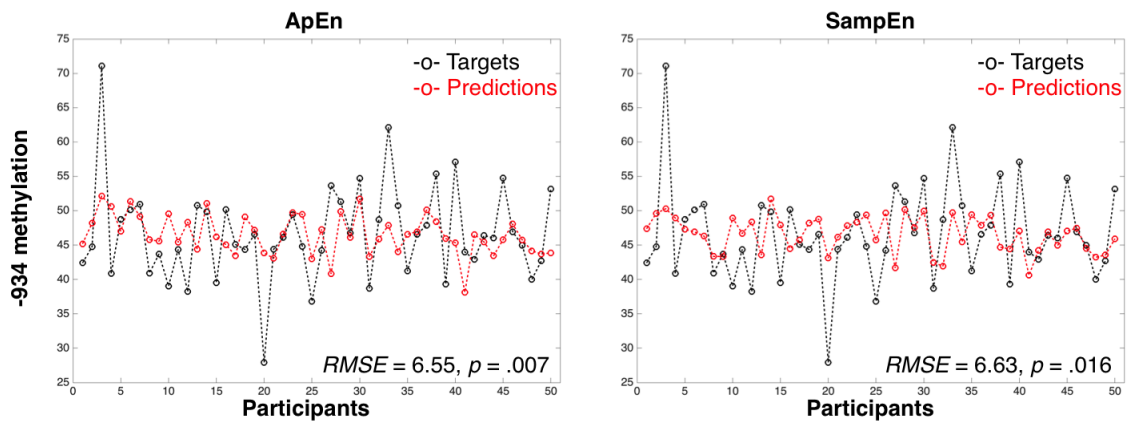


Figure 3.5: Multivariate patterns of entropy in the secondary visual network predict *OXTR* methylation on CpG site -934. Both approximate entropy (*left*) and sample entropy (*right*) were significantly associated with methylation on CpG -934. We omit multivariate weight maps due to the extreme sparsity of each RVR model—ApEn was driven by a mere two regions while SampEn was driven by one region. We therefore recommend cautious interpretation of these findings. See **Table B.8** for a full summary of model fit for all variability metrics in secondary visual analyses.

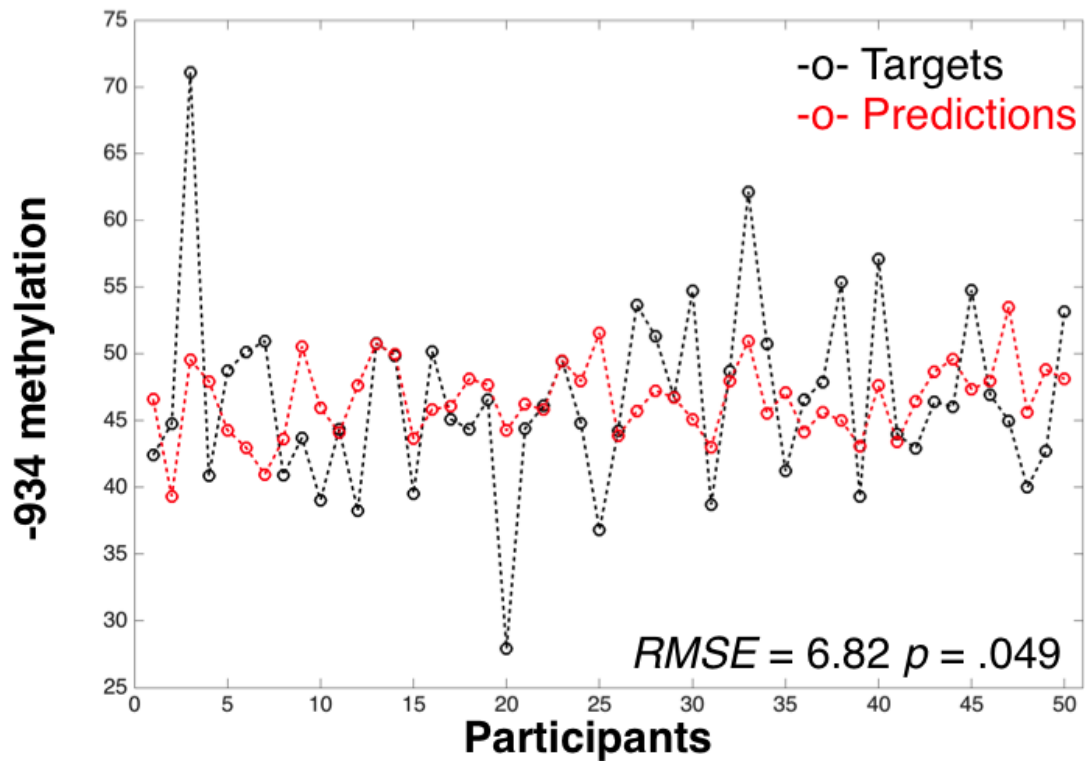


Figure 3.6: Multivariate patterns of LFP in the secondary visual network predict *OXTR* methylation on CpG site -934. Low-frequency power in the secondary visual network was a weak predictor of *OXTR* methylation on CpG site -934. See **Table B.8** for a full summary of model fit for all variability metrics in secondary visual analyses.

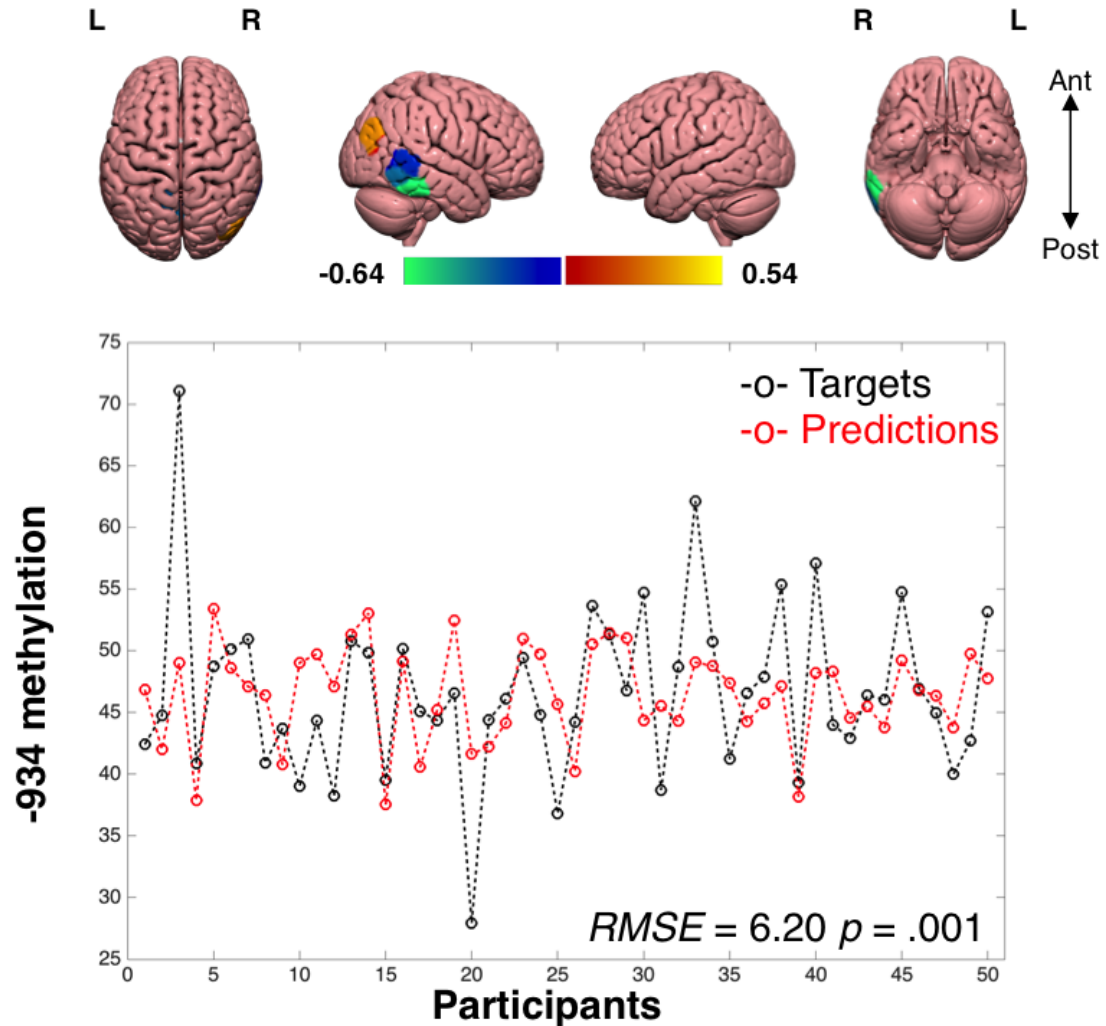


Figure 3.7: Multivariate patterns of temporal variability (σ_t) in the visual association network predict *OXTR* methylation on CpG site -934. RVR analyses in the visual association network revealed a right-lateralized set of regions whose variability over time significantly predicted methylation (weight maps, *top*, are averaged and unit-normalized). The bottom panel displays the correspondence between actual methylation values (*black*) and model predictions (*red*). See **Table B.9** for a full summary of model fit for all variability metrics in visual association analyses.

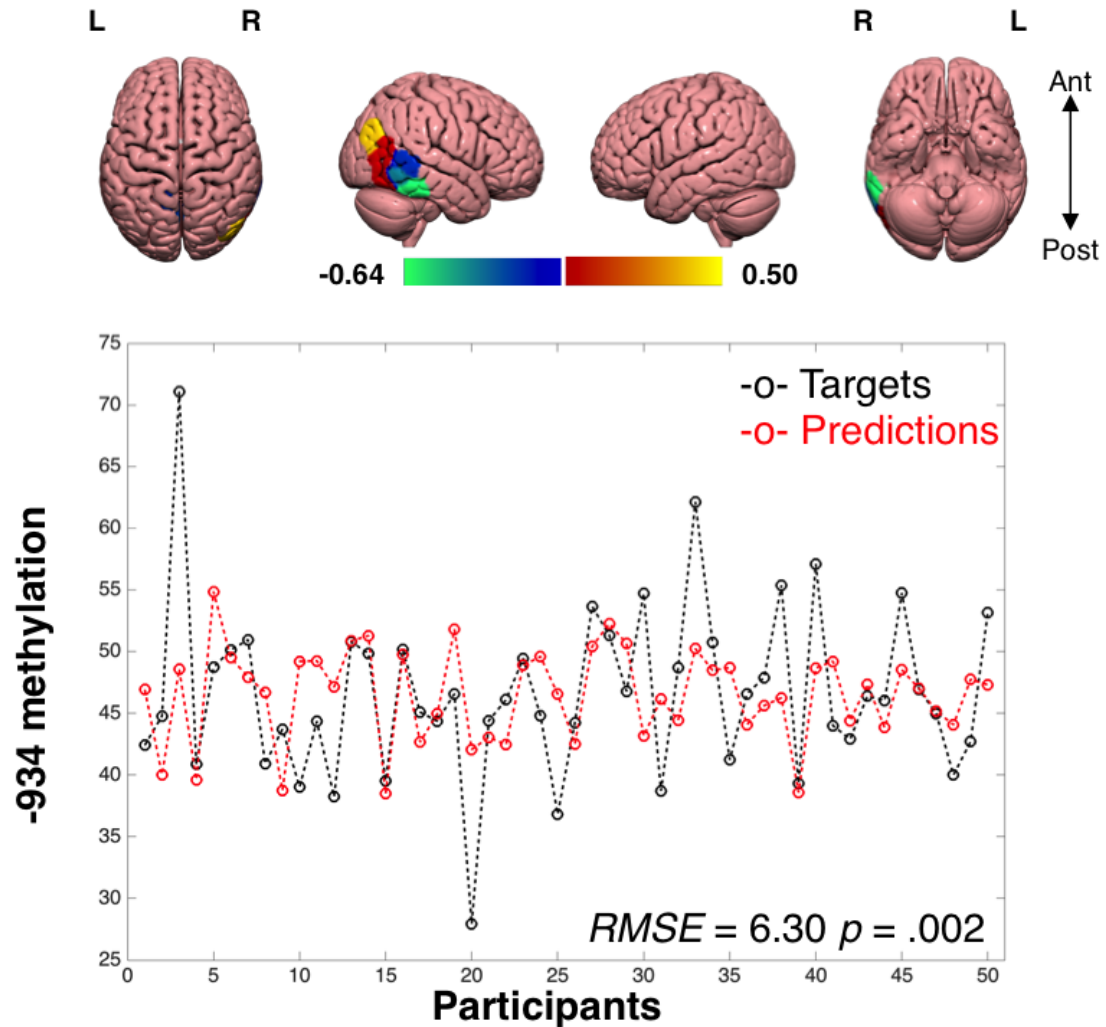


Figure 3.8: Multivariate patterns of spectral variability (σ_{ω}^2) in the visual association network predict *OXTR* methylation on CpG site -934. RVR analyses in the visual association network demonstrated that spectral variability across a right-lateralized set of regions significantly predicted methylation (weight maps, *top*, are averaged and unit-normalized). The bottom panel displays the correspondence between actual methylation values (*black*) and model predictions (*red*). See **Table B.9** for a full summary of model fit for all variability metrics in visual association analyses.

Chapter 4

Experiment 3

Thus far, we have provided evidence that *OXTR* methylation is associated with the topology of task-related functional networks (Experiment 1) and the intrinsic dynamics of the resting brain (Experiment 2). Experiment 3 therefore aimed to combine these approaches in an effort to determine whether spontaneous dynamics in baseline functional connectivity index epigenetic variability along *OXTR*. We were further motivated by the observation that autism spectrum phenotypes are associated with oxytocin receptor deficiencies, hypoconnectivity, and “noisy brains”^{63,130–132}. Our results from the previous experiment suggest that *OXTR* methylation modulates resting BOLD fluctuations. Rather than *hypoconnectivity*, then, it is possible that connectivity is simply more *transient* as a function of decreased oxytocin signaling (which otherwise supports robust synchronous activity^{6,128}). Moreover, because ASD-like traits exist across a wide spectrum in the population, we can usefully model these potential relationships in our sample of neurotypical young adults.

We therefore hypothesized that patterns of dynamic functional connectivity offer a unifying neural endophenotype that explains both underlying molecular makeup and the extent to which one expresses autistic like traits. To quantify

moment-to-moment stability in network coupling, we describe a novel application of entropy to continuous connectivity estimates. Machine learning models are used in an effort to predict *OXTR* methylation and autistic-like traits from patterns of connectivity entropy. We show that network stability within a subsystem of the default mode network (commonly associated with social cognition) indeed predicts both epigenetic and behavioral variability; network stability within a subsystem of the salience network (involved in top-down interpretation of emotional stimuli) also predicts individual differences in methylation. These results highlight functional differences between default mode and salience network components and further validate the use of network endophenotypes as a link between genes and behavior.

4.1 Materials and Methods

4.1.1 Participants

The sample used in the following analyses was identical to that in Experiment 2 (Section 3.1.1): we present data from 50 self-identified Caucasians (24 men, 26 women; $M_{age} = 20.78 \pm 2.64 SD$, range = 18-30) with complete methylation data and acceptable head motion during resting-state fMRI. All individuals provided written informed consent for a protocol approved by the University of Virginia Institutional Review Board (Protocol 15051; Principal Investigator, Jessica J. Connelly).

4.1.2 Blood collection epigenotyping

As in Experiments 1 and 2, we report percent DNA methylation on *OXTR* CpG sites -934 and -860. Blood collection, DNA extraction, and epigenotyping procedures were identical to those described in Experiment 1 (see Section 2.1.2 and Section 2.1.3).

4.1.3 Behavioral assessment: The broad autism phenotype

We obtained estimates of the *broad autism phenotype* (BAP) using the 50-item Autism-Spectrum Quotient (AQ)¹⁴⁴. The AQ is a self-report assay quantifying the extent to which individuals express autistic-like traits over five subscales: social skill, attention switching, attention to detail, communication, and imagination. Subscale scores were summed to obtain a total out of 50 (with 32 as a potential clinical cutoff¹⁴⁴). Although not a diagnostic scale *per se*, the AQ was demonstrated to be a reliable indicator of BAP expression in neurotypical controls and individuals with Asperger Syndrome and high-functioning autism¹⁴⁴.

4.1.4 Resting-state fMRI acquisition and preprocessing

Image acquisition and preprocessing procedures followed those described in Experiment 2 (Section 3.1.3). Briefly, whole-brain resting-state fMRI was collected using a high-speed mbEPI sequence. Data underwent standard preprocessing using SPM8 in Matlab. We additionally performed voxelwise global signal scaling, linear detrending, wavelet despiking, and nuisance regression of motion parameters.

4.1.5 Network selection and timeseries extraction

Due to the computational complexity of dynamic connectivity analyses, we limited our focus to individual networks and their subsystems rather than whole-brain models. Specifically, we examined functionally-distinct components of the default mode network (DMN) and salience network (SN) as defined by an adapted version of the Willard atlas¹³⁹. We modified the original atlas because Willard regions were initially defined using independent component analysis—component clusters near the midline often spanned both hemispheres, requiring them to be split in two for the present analyses.

The DMN was partitioned into a *dorsal* (dDMN) component and a *ventral* (vDMN) component (**Figure 4.1**). The dDMN largely corresponds to what others have termed the *dorsal medial subsystem*—these regions, primarily spanning the posterior cingulate and medial PFC, are frequently associated with empathetic processes such as mentalizing and perspective-taking^{205,206}. Accordingly, connectivity across these regions is compromised in ASD^{207,208}. The vDMN is relatively intact, by contrast—it comprises a *medial temporal subsystem* that is primarily associated with mental time-travel and other autobiographical memory-related functions^{205,206}. Consequently, we expect that *OXTR* methylation and BAP expression will be associated with networks dynamics in the dDMN, *not* the vDMN.

Similarly, the SN was partitioned into an *anterior* (aSN) component and a *posterior* (pSN) component (**Figure 4.2**). Nodes of the aSN (e.g. the anterior insula, dorsal anterior cingulate, and dorsomedial PFC) are associated with a host of functions, including attentional orienting, cognitive control, and various empathetic/emotional processes, such as top-down assessment of emotional signals in predictive coding models; the pSN is primarily linked to bottom-up, autonomic responses to externally- and internally-generated signals^{105,106,209,210}. Although there is evidence to suggest autistic individuals have difficulties regulating autonomic responses, aSN deficits are most commonly associated with ASD^{211,212}. We therefore suspect a similar dissociation between SN subsystems to emerge, such that aSN dynamics predict methylation and behavior to a greater extent than pSN dynamics.

4.1.6 Dynamic functional connectivity estimation

We estimated dynamic connectivity between network nodes using *multiplication of temporal derivatives* (MTD)^{213–215}. Similar to other dynamic connectivity techniques, MTD is dependent on a *window parameter*, w . However, *unlike* the standard win-

dowed cross-correlation approach—which uses w to define a series of discrete, non-overlapping temporal windows—MTD uses this parameter to define the width of a one-dimensional temporal smoothing operator (a *simple moving average*). Thus, MTD yields a time-resolved, continuous estimate of moment-to-moment connectivity.

As the name implies, MTD is based on a pointwise multiplication of velocity vectors (i.e. first derivatives) for a pair of BOLD timeseries. Let w denote the width of the smoothing window and d_i and d_j denote the temporal derivatives of two regional timeseries, x_i and x_j (with length, T , and standard deviations of velocity, σ_i and σ_j)—the MTD estimate of connectivity at time, t , is then:

$$MTD_{i,j}(t) = \frac{1}{w} \sum_t^{t+w} \frac{d_i(t)d_j(t)}{\sigma_i\sigma_j}. \quad (4.1)$$

Put differently, MTD yields a normalized estimate of similarity in rates of change between two signals. Like a Pearson correlation, it can be positive (suggesting “in-phase” coupling) or negative (suggesting “anti-phase” coupling). The smoothing window serves to protect against high-frequency noise; thus, it is typically set within a range comparable to the temporal filter applied to the BOLD signal. We set $w = 10$ seconds per prior recommendations^{213–215}, which corresponds to ~ 0.10 Hz. The end result is an $N \times N \times (T - w - 1)$ matrix, \mathbf{A} , of continuous, dynamic connectivity estimates, where N is the number of network nodes and $(T - w - 1)$ is the number of timepoints (reduced from the original total, T , due to taking a derivative and applying smoothing). We left \mathbf{A} for each network *unthresholded*, as there is no parametric null distribution from which to estimate significance. Moreover, the temporal smoothing applied to each network edge hampers the ability to compute p -values via surrogate or permutation testing, as connectivity estimates over time are necessarily non-independent of one another.

Connectivity entropy. Given that each edge in \mathbf{A} is itself a timeseries, we computed

the approximate entropy ($m = 2, r = 0.25 \times MAD$) for each pairwise connection in the network. Similar to ApEn as discussed in **Section 3.1.5**, this offers a means of estimating the complexity or stability of interregional connectivity over time: relatively-constant connections would yield low entropy while highly-dynamic connections would be characterized by high entropy. Modeling edgewise variability in this way is preferable to possible alternatives such as the standard deviation, because a regularly-oscillating signal can nevertheless cover a wide range in amplitude. Connectivity entropy, by contrast, directly quantifies the probability of similar connectivity states in a temporally-evolving network. Thus, we can test whether *OXTR* methylation might be associated with high-fidelity connectivity and whether these network characteristics additionally explain behavioral outcomes.

4.1.7 Multivariate pattern analysis: Relevance vector regression

We next sought to determine whether multivariate patterns of network stability might jointly predict both *OXTR* methylation and the extent to which one expressed autistic-like traits. Relevance vector regression was again performed using the SparseBayes software (v2.0) in Matlab. Edgewise connectivity entropy estimates for a particular network (either dDMN, vDMN, aSN, or pSN) served as training inputs; *OXTR* methylation values and BAP scores were given as targets for prediction. Although we previously attempted to model network data in its primal representation whenever possible, the number of features (i.e. edges) in each network consistently exceeded the number of training examples—thus, all network data were compressed into a linear kernel space. We omit a complete description of RVR estimation here as we have described it previously (see **Section 2.1.7**).

Models were trained and tested using leave-one-subject-out cross-validation (LOSO-CV). At each step, one subject was removed from the kernel, the remaining

data were centered, and the model was fit, yielding a sparse vector of kernel hyperparameters. These were applied to the left-out feature vector to obtain a predicted methylation value; root mean squared error (*RMSE*) was computed over all folds as a measure of accuracy. Finally, we used 1,000 iterations of nonparametric permutation testing to determine whether models were performing above chance. We report *p*-values indicating the probability of permuted models yielded lower error than the “true” model.

4.1.8 Brain data visualization

Kernel weights were projected back into the original space of the data, averaged over CV folds, and unit normalized. Network regions and their multivariate maps were visualized using the BrainNet Viewer (<https://www.nitrc.org/projects/bnv/>)¹⁶³.

4.2 Results

4.2.1 *OXTR* methylation and the broad autism phenotype

We previously reported general methylation-related results for this sample in Experiment 2 (see **Section 3.2.1**). In line with the notion that ASD traits are still expressed along a continuum in the neurotypical population, we observed a normal distribution of BAP scores (although none exceeded the clinical cutoff; **Figure 4.4**). We subsequently used a linear mixed effects model to determine whether BAP scores significantly differed by sex and *OXTR* methylation. Methylation was entered as a random effect whose slope varied freely by CpG site. Because it is nontrivial to compute degrees of freedom in mixed models, we used a Satterthwaite approximation to test against the null hypothesis of no effect for each parameter

(model-level statistics are collated in **Table 4.1**). Although men ($M = 18.92 \pm 4.64$ SD) tended to be higher on BAP than women ($M = 15.27 \pm 5.50$ SD), there was not a main effect of sex ($\beta = 2.27, SE = 3.14; t = 0.72, p = .472$). Percent methylation was significantly associated with BAP scores, such that higher methylation predicted lower expression of the broad autism phenotype ($\beta = -0.20, SE = 0.08; t = -2.49, p = .046$). There was no further interaction between sex and methylation ($\beta = .02, SE = 0.08; t = 0.28, p = .780$); however, see **Figure 4.4** for sex and CpG-specific relationships between *OXTR* methylation and BAP.

Parameter	Estimate	SE	t (p)
Intercept	22.87	4.14	5.52 (.081)
Sex	2.27	3.14	0.72 (.472)
Methylation	-0.20	0.08	-2.49 (.046)
Sex \times Methylation	0.02	0.08	0.28 (.780)

Table 4.1: Inter-individual variability in *OXTR* methylation predicts differences in the broad autism phenotype. A linear mixed-effects model demonstrated a significant inverse relationship between *OXTR* methylation and the broad autism phenotype. T -statistics and p -values obtained using the Satterthwaite approximation. Although there was not a significant interaction between sex and methylation, CpG site and sex-specific relationships are visualized in **Figure 4.4**.

A more focal analysis demonstrated that the effect of methylation was primarily driven by CpG site -934 [$r(48) = -0.40, p = .004$, two-tailed]. CpG -860 was not significantly correlated with BAP [$r(48) = -0.25, p = .078$, two-tailed]. We also observed no correlation between BAP scores and participant head motion [$r(48) = .004, p = .978$, two-tailed].

4.2.2 Connectivity entropy: Default mode network

As hypothesized, multivariate patterns of connectivity entropy within the dorsal DMN predicted *OXTR* methylation and the extent to which individuals expressed autistic like traits (**Figure 4.5**)—this did not hold in the ventral DMN (**Table 4.2**).

Specifically, dDMN entropy informed individual differences on CpG site -860 ($RMSE = 5.69, p = .011$) and BAP ($RMSE = 4.99, p = .022$); methylation on CpG -934 was poorly-predicted in comparison ($RMSE = 8.50, p = .961$). The weights learned by RVR generally pushed expected methylation and BAP in opposite directions, such that higher entropy across the dDMN was associated with increased methylation and decreased BAP scores. This follows the inverse relationship described between *OXTR* methylation and BAP above, although CpG site -860 was not significantly correlated with autistic-like traits. Nevertheless, these results suggest that *OXTR* methylation may contribute to the baseline stability of networks related to social cognition, ultimately translating into behavioral variability.

Component	CpG -934	CpG -860	BAP
dDMN	8.50 (.961)	5.69 (.011)	4.99 (.022)
vDMN	7.89 (.526)	6.80 (.257)	6.12 (.595)

Table 4.2: RVR model fit: Default mode network. Prediction accuracies ($RMSE$) are given for RVR models on dDMN and vDMN data (see **Figure 4.5** for weight maps corresponding to significant dDMN analyses). P -values derived from 1,000 iterations of nonparametric permutation testing are given in parentheses.

4.2.3 Connectivity entropy: Salience network

Model performance in the salience network lent partial support to our hypothesis: multivariate patterns of connectivity entropy in the aSN significantly predicted *OXTR* methylation on both CpG sites, but it did not predict behavior. Entropy in the pSN was not associated with methylation or behavior (**Table 4.3**). For aSN models, accuracy was trivially better for CpG -934 ($RMSE = 6.56, p = .019$) relative to CpG -860 ($RMSE = 6.11, p = .040$)—the larger magnitude of $RMSE$ for site -934 merely reflects greater variability in percent methylation across individuals. Weights were positive across aSN edges for both methylation models, such that

more entropic networks predicted higher methylation (consistent with the dDMN weight distribution for CpG -860). It is possible that we may have predicted BAP scores with a larger sample ($RMSE = 5.49, p = .092$); nevertheless, the present findings demonstrate that *OXTR* methylation may modulate the baseline dynamics of salience network components involved in top-down evaluation of social-emotional information.

Component	CpG -934	CpG -860	BAP
aSN	6.56 (.019)	6.11 (.040)	5.49 (.092)
pSN	8.17 (.780)	7.78 (.958)	6.53 (.941)

Table 4.3: RVR model fit: Salience network. Prediction accuracies ($RMSE$) are given for RVR models on aSN and pSN data (see **Figure 4.6** for weight maps corresponding to significant aSN analyses). P -values derived from 1,000 iterations of nonparametric permutation testing are given in parentheses.

4.3 Discussion

In this experiment, we describe a novel approach to capturing the dynamics of functional brain networks, estimating the entropy of moment-to-moment connectivity between system components. Although previous research has associated ASD phenotypes with widespread hypoconnectivity^{131,132,207,208,211,212}, we hypothesized that “noisy brains” were a more plausible explanation—rather than being disconnected, individuals expressing autistic-like traits would exhibit transient, dynamic connectivity that might otherwise deflate “static” estimates over the course of a scan. We proposed increased *OXTR* methylation as an underlying mechanism, such that decreased access to endogenous oxytocin would produce less-robust functional connections. A series of machine learning models lent partial support to our hypothesis: patterns of connectivity entropy in the dDMN jointly predicted *OXTR* methylation on CpG site -860 in addition to variation in BAP scores, but

the direction of the behavioral effect was contrary to expectation (more entropy predicted decreased expression of the broad autism phenotype). Additionally, multivariate patterns of entropy in the aSN successfully predicted methylation on both CpG sites, but we did not obtain a significant effect of entropy on behavior.

4.3.1 Open questions about methylation-behavior relationships

We observed an unexpected negative relationship between *OXTR* methylation and behavior. This ran counter to previous research, which found higher levels of methylation in ASD relative to neurotypical controls⁶³. Of course, there are a number of plausible explanations why our sample of healthy young adults did not replicate the effect observed in a clinical population. One obvious possibility is that methylation-behavior associations are parabolic or nonlinear over the spectrum from healthy cognition to social deficit disorders—cross-sectional studies or those limited strictly to neurotypical or patient groups will therefore never fully capture the nuance of the relationship. However, obtaining an accurate estimate of the underlying latent function would require a massive effort to recruit individuals covering the full range of behavior. Another potential account is that healthy individuals possess compensatory mechanisms which insulate them against the deleterious effects of high *OXTR* methylation. For example, oxytocin and arginine vasopressin are known to promiscuously bind to one another's receptors—this was originally a major challenge for mapping OT receptors across the brain^{29,30}, and it opens up the possibility that one may be able to compensate for deficiencies in the other. Whenever possible, future work should consider molecular markers related to both peptides, especially within neurotypical populations. Finally, and perhaps most intriguingly, there may be differences related to “standard” methylation and *hydroxymethylation* between clinical and neurotypical populations. While DNA

methylation is traditionally associated with decreases in gene expression, hydroxymethylation has been tied to both *de*-methylation (as an intermediate step) and *increases* in gene expression^{216,217}. We did not explicitly measure hydroxymethylation here; thus, it is critical for later studies to attempt to differentiate between these processes. If neurotypicals are largely hydroxymethylated, this would explain the inverse relationship we observed—more methylation might instead indicate greater endogenous access to oxytocin, ultimately predicting decreases in BAP expression.

4.3.2 Functional networks and their subsystems

We hypothesized there would be a dissociation between DMN components and SN components, such that only one of their subsystems would predict *OXTR* methylation and behavior. Although we (and others) have characterized each subsystem as functionally-distinct, they are not functionally-*orthogonal*—dDMN and vDMN regions undoubtedly communicate with one another, as do components of the aSN and pSN. On a broader scale, the DMN and SN also interact. The decision to focus on subsystem connectivity was supported by previous work indicating specific deficits in ASD^{207,208,211,212}, but it was also largely practical due to the computational complexity of dynamic connectivity analyses.

Our results confirmed that *OXTR* methylation is associated specifically with networks that support social cognition. However, this only translated into behavioral variability through the dorsal DMN. We propose that these predictive differences highlight unique functional roles for the dDMN and aSN in social behavior. The dorsal DMN has previously been associated with effortful mentalizing processes (e.g. inferring goal states or the beliefs of others) and social abstraction, including the retrieval of social knowledge (e.g. norms of behavior)^{205,206}. Nodes of the aSN, by contrast, are often linked to attentional and emotional processes^{105,106,209,210}.

Therefore, the dorsal DMN may contribute more directly to overt social behaviors, while the anterior SN may be involved in signal detection and inference processes associated with predictive coding. This would explain why entropy in dDMN indexed both methylation and behavior while aSN dynamics only predicted methylation. In both cases, we suggest that endogenous access to oxytocin supports the coherence and stability of functional connectivity. However, the primary role of the aSN may be to integrate bottom-up signals with an internal model of the social-emotional self^{105,106}—this would indirectly affect behavior by generating a “hypothesis” that other systems (e.g. the dorsal DMN) apply and translate into action. Moreover, if endogenous access to oxytocin facilitates the precise, coordinated signaling required for active social inference (perhaps through mutual-modulation of dopamine systems)^{6,104,124,128}, this would explain why higher levels of methylation were consistently associated with more entropic brains (particularly in the aSN).

4.3.3 Entropy and the search for a gene-brain-behavior model

Entropy itself is a dimensionless quantity that reflects the uncertainty inherent in a system. More specifically, in the present analyses, it quantifies the extent to which a network edge exhibits predictable patterns of connectivity over time. Decreases in entropy across a functional network may therefore imply metastable connectivity states, fluctuating around a robust neurobiological equilibrium²¹⁸. However, we note that our approach cannot quantify or test metastability *per se*—rather, entropy may simply quantify the *number* of metastable states (i.e. the proportion of accurately-predicted states). A more direct assessment of metastability would require: 1) an exhaustive search over the brain’s phase space to identify the “lowest-energy” connectivity state, and 2) a point-process analysis that identifies

concerted phase shifts from the low-energy state, both of which were beyond the scope of the present analysis.

Nevertheless, recent efforts to put forth a unified theory of brain function suggest that healthy cognition (and consciousness more broadly) depends on a sort of entropic “Goldilocks zone” in brain systems^{219–221}. In other words, normal waking consciousness is typically characterized by a suppression of entropy that allows the brain to organize itself into neatly-ordered hierarchical systems^{220,222}. These enable careful, structured sampling of the environment during predictive coding and active inference processes. However, at the same time, prediction error and subsequent hypothesis updating induce entropy and thus require flexibility and criticality (i.e. phase transitions) in brain systems. This has led some to suggest that the Goldilocks zone is a sort of “self-organized instability”—a delicate balance between order and entropy that facilitates optimal perceptual inference^{220,221}.

We show that tipping the scales towards entropy predicts deficiencies in epigenetic factors thought to support accurate social perception and inference (i.e. endogenous access to oxytocin). In the dorsal DMN, this also predicted behavioral differences, but not in the direction expected from neural entropy theories: increased entropy was associated with decreased expression of autistic-like traits. Still, if healthy cognition truly depends on an optimal level of entropy, it follows that *too little* entropy should also have adverse effects on behavior—our data suggested that low-entropy individuals indeed expressed higher levels of the broad autism phenotype (although we reiterate that none exceeded the traditional clinical threshold). Thus, it appears increasingly likely that there exists a complex nonlinear relationship between *OXTR* methylation, network entropy, and social-behavioral outcomes. We urge future studies to explore this possibility further. However, at present, these analyses provide a critical first step towards identifying a network

endophenotype that bridges the gap between genes and behavior.

4.4 Figures

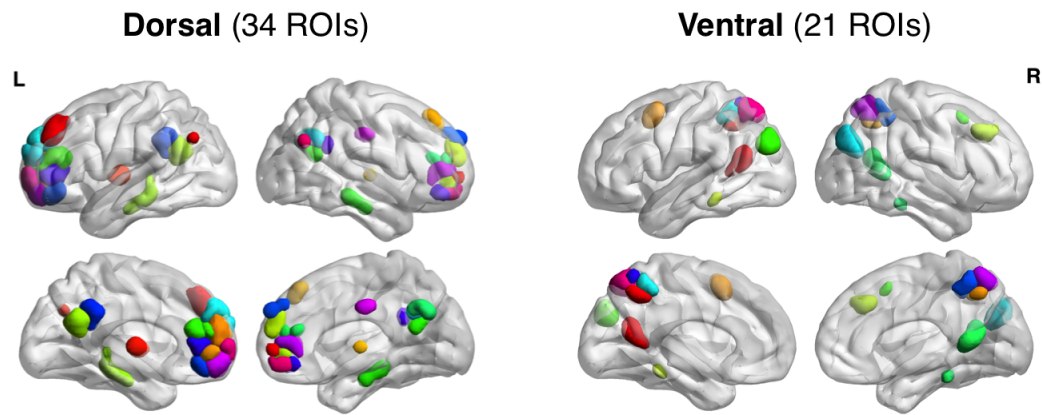


Figure 4.1: Subsystems of the default mode network. Dynamic connectivity was assessed in two functionally-distinct subdivisions of the default mode network, as defined by the Willard atlas: the dorsal component (*left*) and the ventral component (*right*).

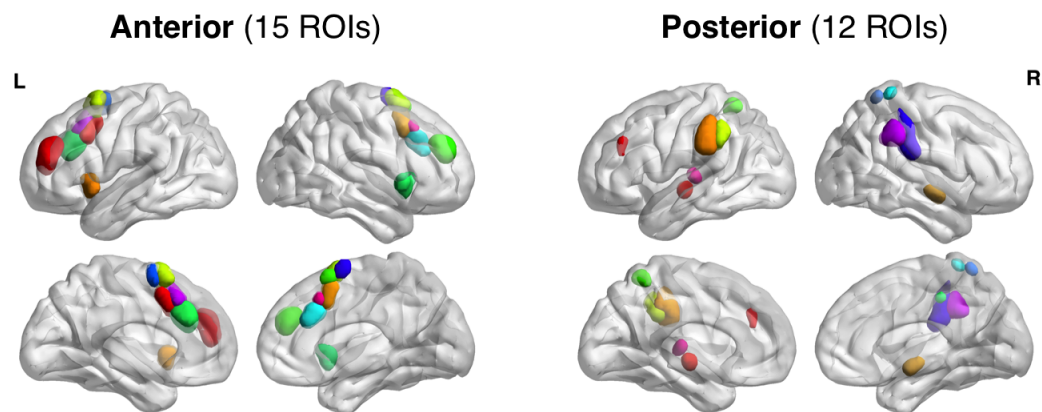


Figure 4.2: Subsystems of the salience network. Dynamic connectivity was assessed in two functionally-distinct subdivisions of the salience network, as defined by the Willard atlas: the anterior component (*left*) and the posterior component (*right*).

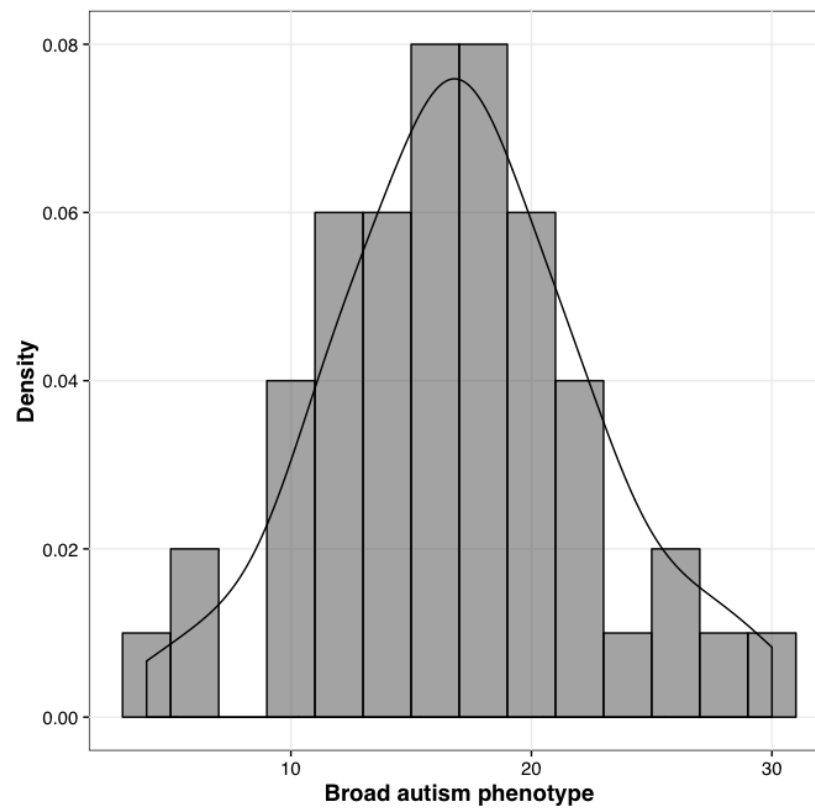


Figure 4.3: Distribution of broad autism phenotype scores. The extent to which individuals expressed autistic-like traits was normally-distributed in our sample ($N = 50$; $M = 17.02 \pm 5.38 SD$, range = 4-30). Note, however, that none exceeded the suggested clinical cutoff of 32.

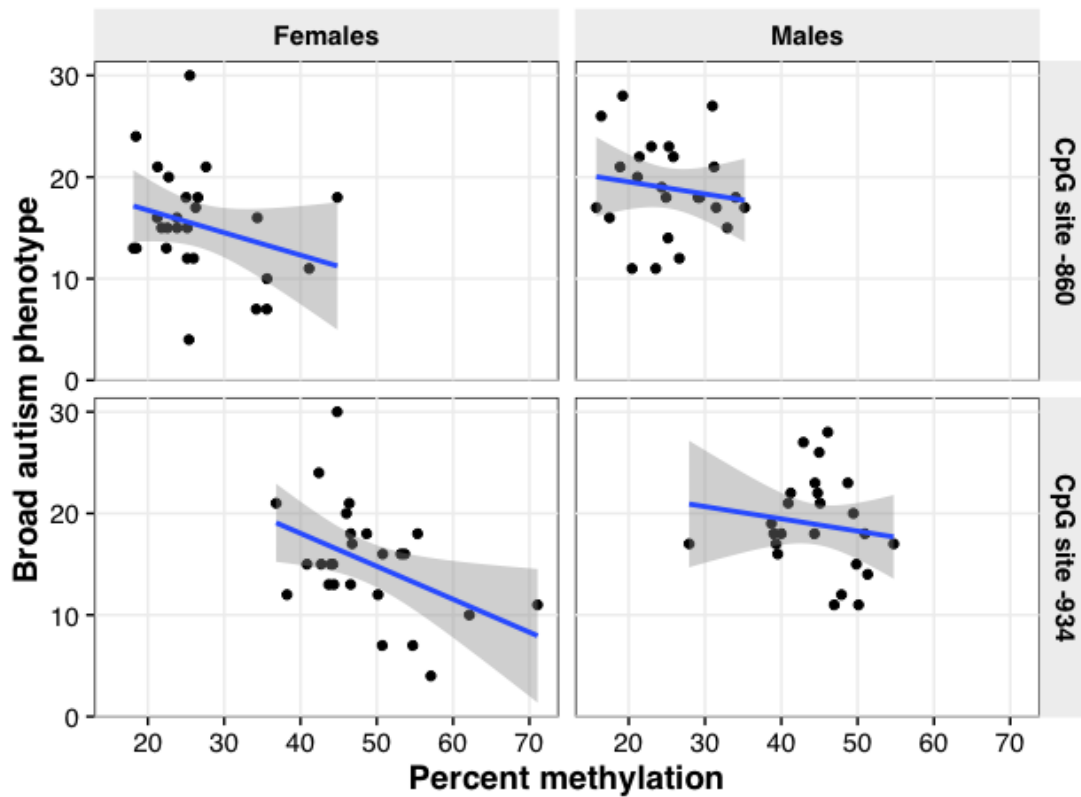


Figure 4.4: Relationships between BAP and *OXTR* methylation by sex and CpG site. In general, higher levels of methylation predicted lower expression of the broad autism phenotype, but there was not a significant effect of sex (nor an interaction between methylation and sex; see **Table 4.1** for parameter estimates from a linear mixed effects model).

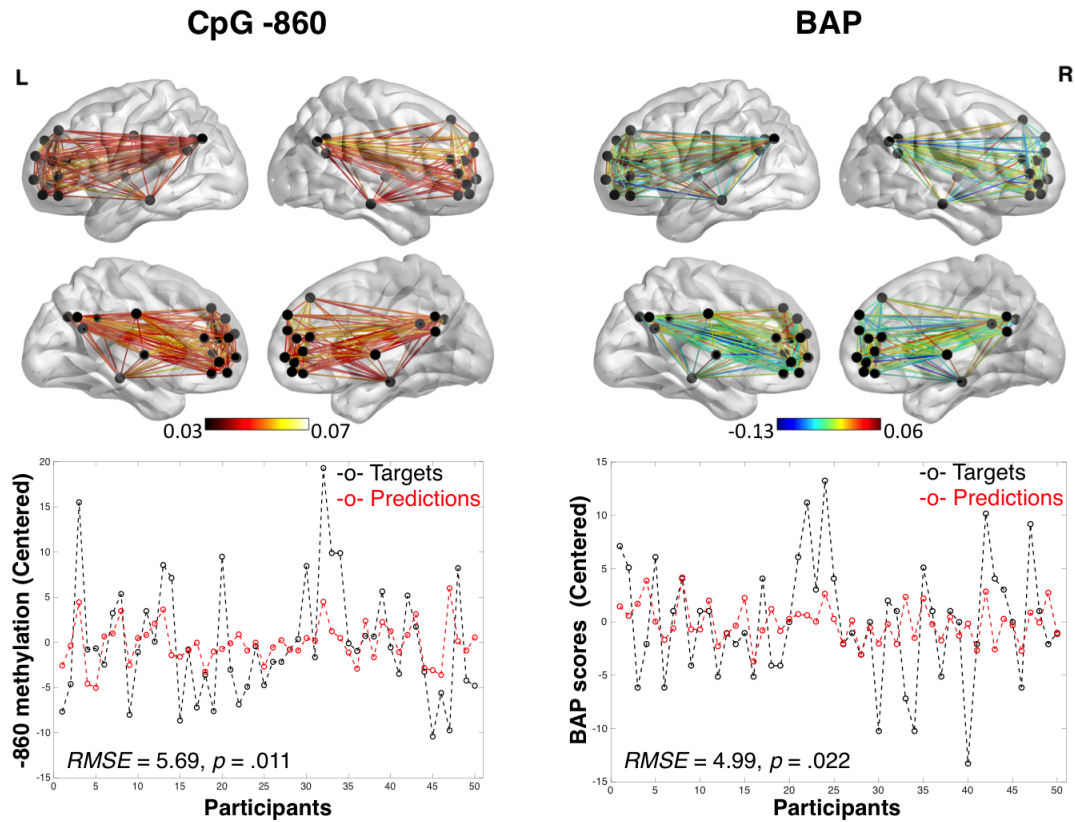


Figure 4.5: Connectivity entropy in the dorsal DMN predicts *OXTR* methylation and BAP scores. Multivariate weight maps for edgewise connectivity entropy are displayed for CpG site -860 (*left*) and BAP (*right*). Weights were exclusively positive for the methylation model, such that increased entropy across the network predicted increased levels of methylation; similarly, weights were almost entirely negative for the BAP model, such that more entropic brains were associated with lower levels of BAP. Bottom panels display the correspondence between target values (*black*) and relevance vector model predictions (*red*).

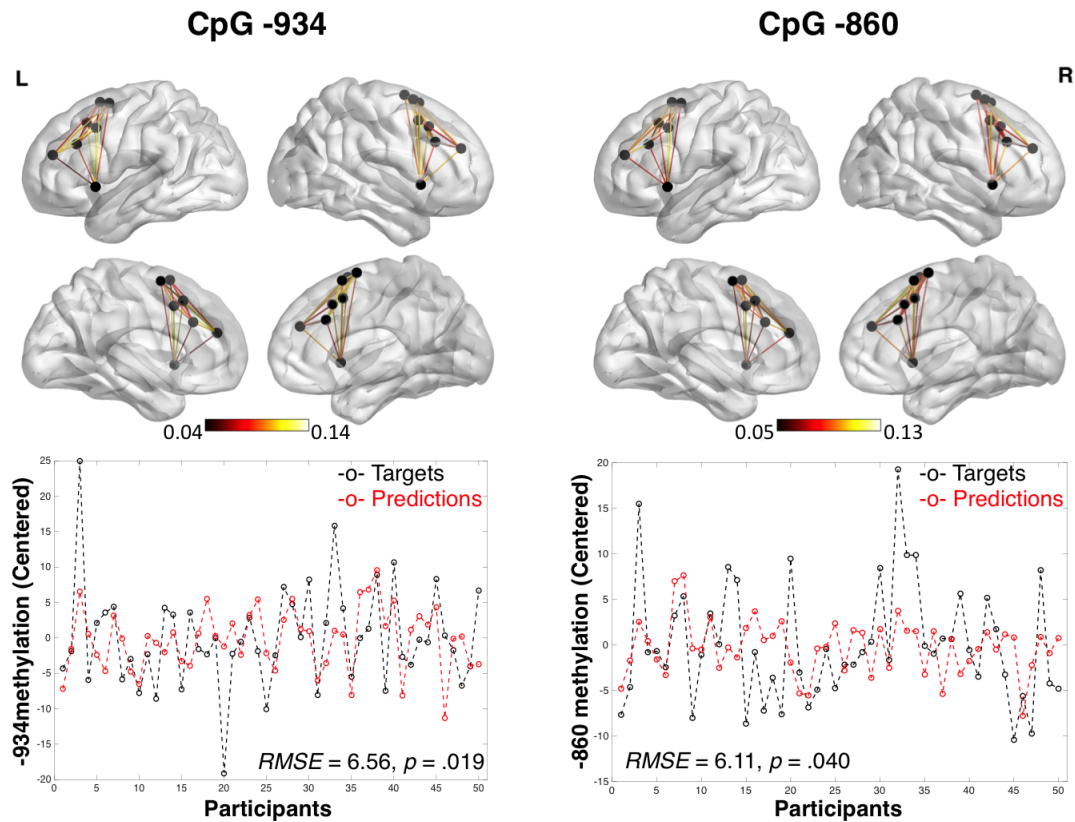


Figure 4.6: Connectivity entropy in the anterior SN predicts *OXTR* methylation. Multivariate weight maps for edgewise connectivity entropy are displayed for CpG site -860 (left) and CpG site-934 (right). Unlike the dorsal DMN, connectivity entropy did not predict behavior. For both models, weights were exclusively positive, such that increased entropy across the network predicted increased levels of methylation. Bottom panels display the correspondence between target values (black) and relevance vector model predictions (red).

Chapter 5

General discussion

The broad aim of this work was to develop a network-based endophenotype linking together genes and social-behavioral outcomes. We presented three studies toward that end, offering both novel applications of previously-existing methods and new means of quantifying dynamics in functional brain networks. Beginning with a consideration of task-related connectomes, we identified epigenetic fingerprints in the spatial topology of widely-distributed functional networks in service of social cognition. We then investigated the intrinsic dynamics of the resting brain. Our second experiment demonstrated that epigenetic variability was reflected across spatial patterns of spontaneous BOLD variability—both in subcortical networks that are dopamine-rich and networks that participate in higher-level social perception. Finally, we detailed the estimation and use of *connectivity entropy* to quantify stability within functional networks, providing evidence that network dynamics explain individual differences at the epigenetic and behavioral levels. Although we used oxytocin and social cognition as a model foundation, these methods have the potential to illuminate complex interactions across multiple levels of brain systems in numerous contexts, from social behavior and beyond.

5.1 Emergent phenomena and the evolution of network neuroscience

A wealth of past neuroimaging research has undoubtedly yielded critical insights into the biological bases of social cognition. Similarly, early applications of imaging genetics provided much needed tests of a hypothesis long-intuited to be true: that one's genetic makeup likely modulates the structure and function of the brain. Nevertheless, many of these previous studies have been slaves to the mean, searching for average differences in activity between task-related conditions or groups defined by genetic polymorphisms. In such *mass-univariate* approaches to fMRI data analysis, each voxel is treated as an independent statistical test under the general linear model (GLM)—it is consequently assumed (for statistical reasons) that there are no dependencies in activity across voxels or brain regions more generally. This has led to uncharitable critiques of fMRI as “blobology” or “neophrenology,” with researchers imagined as desperate mental gymnasts, attempting to reduce complex cognitive functions to splotches of activity on a brain.

Of course, the brain is not merely a collection of individual cogs, spinning freely on their own. There are complex feedback loops, time-dependent patterns of inhibition, excitation, and so on, such that one's ultimate conscious experience is supported by a vast network of neuroanatomical substrates. While the love affair between neuroimaging researchers and the GLM may truly last forever, the advent of multivariate pattern analyses (MVPA) in the last decade has invigorated a discussion over how information is represented across wide swaths of brainspace. However, MVPA alone *cannot* tell us how these brain regions interact over time, nor can it uncover the topology of neurobiological systems underlying a given behavior or function. This requires conceptualization of the brain as something like

a classical computer network, with “nodes” (brain regions) that communicate along “edges” connecting them. Although cognitive psychologists and neuroscientists have long described the brain colloquially as an information processing network, only recently have we been able to explicitly model functional neuroimaging data in this fashion.

Neuroscience as a field has been quick to embrace concepts derived from network science and complex systems theory. The explosion of network-based models of the brain has consequently led to powerful revelations about behavior and individual differences. Recent evidence has highlighted the notion that brain connectivity is a stable, intrinsic trait unique to an individual^{175–177}, and psychopathological states such as autism^{131,132,207,208,211,212,223}, schizophrenia²²², and Alzheimer’s dementia¹⁷² (among others¹⁷³) are increasingly associated with abnormalities in functional and structural networks. Moreover, the integration of these methods with the philosophy of mind has generated a number of fascinating insights into the relationship between mental processes and the physical brain²²⁴.

A key concept is that of *emergence* in complex systems. In short, a complex system is one whose overall behavior is greater than a mere sum of its parts. In other words, cognition and behavior are emergent phenomena that arise from components of the brain *interacting*. Thus, in order for us to understand the output of our system, we need to consider how different pieces of the machinery are functioning together; we cannot realistically hope to identify a 1:1 mapping between behavior and the brain. An ideal model would take into account *multiscale* interactions spanning molecular, cellular, and cortical system components. However, as neuroimaging researchers, we often cannot resolve events occurring at sub-millimeter spatial scales (or at millisecond temporal scales).

Therefore, one of the primary motivations for the current work was to circum-

vent these deficits in resolution and identify cortical-scale interactions that explain both molecular-level factors and behavioral outcomes. More specifically, we sought to identify potential molecular mechanisms that might guide or support differences in network function, ultimately translating into variation in behavior. While there is rising interest in the genetic and epigenetic bases of network connectivity^{61,100,138–142}, these factors remain poorly understood—especially given that many studies still turn to genetic polymorphisms that are merely associative, lacking clearly-defined functions. A major strength of our approach was our focus on epigenetic modifications to the oxytocin receptor gene—a molecular variable with known functional consequences, both in terms of gene transcription⁷² (thereby regulating endogenous access to oxytocin) and social behavioral phenotypes⁶³. Our experiments here offered proof of concept that such molecular-level information can be *decoded* from multiple modalities of macroscale brain network data; although this will not be possible for *all* genes (e.g. those which cannot be reliably measured in peripheral sources), we hope future studies will follow suit in attempting to model gene-brain interactions as they relate to behavior.

5.2 Epigenetic modulation of functional network architecture

Despite the controversy surrounding intranasal oxytocin research, a number of studies have consistently found that OT administration increases functional connectivity across regions relevant for social perception, motivation, and cognition more broadly^{9,11,12,91–94}. Still, these effects are highly-acute, and furthermore, it is unclear whether (or to what extent) baseline connectivity (i.e. pre-intranasal OT) in these systems was previously shaped by endogenous oxytocin function. If network

connectivity developed in absence of robust oxytocin input—perhaps due to high *OXTR* methylation—this may place an upper bound on the potential for exogenous OT to enhance interregional coupling. We previously demonstrated that *OXTR* methylation predicts differences in seed-based connectivity with the amygdala, such that increased methylation was associated with decreased connectivity. However, a shortcoming of seed-based connectivity is blindness to other multivariate interactions across the network.

Experiment 1 in the present report extended these findings to show that large-scale network topologies reflect differences in endogenous access to oxytocin. Critically, we demonstrated that models based on nodal centrality were generalizable to an independent sample of individuals. Centrality measures attempt to capture the hub-like behavior of nodes in the network—our metric of choice (eigencentrality) directly quantified the extent to which each node explained overall variance in connectivity. These results suggest that processes such as DNA methylation may mediate the spatial development of functional networks, including the distribution of central hubs. Interestingly, a general role proposed for oxytocin is the initiation of synchronous activity across networks¹²⁸—this sort of rapid, distributed action is most easily enabled via hubs, which coordinate information flow between distant network nodes¹⁷⁴. Thus, decreased access to endogenous oxytocin may result in less efficient network configurations. A consequence of weakened functional infrastructure might be increased regional activity, as disconnected nodes cannot coordinate with or rely on other regions to facilitate behavior. This interpretation fits nicely with our earlier work demonstrating increases in regional BOLD activity with higher levels of *OXTR* methylation^{99,100}. Importantly, many of the regions previously showing this association were weighted negatively in our current machine learning models, suggesting that lower levels of connectivity indeed predict

higher levels of methylation. In light of previous research demonstrating that functional network architecture is largely stable over time and task states in young adults^{175,176}, this again implies a role for *OXTR* methylation in early functional network development.

5.3 Epigenetic modulation of functional network dynamics

Recent work in animal models has suggested that oxytocin robustly amplifies neural signal-to-noise ratios⁶. This process is likely to involve interactions with dopaminergic systems, which overlap considerably with subcortical oxytocin pathways²⁷ and are known to act as gain modulators in the brain, increasing SNR in response to relevant external inputs^{41,42,44}. Given that behavioral deficits associated with oxytocin receptor deficiencies (e.g. ASD⁶³) are also characterized by noisy brains *dinstein2012*, this suggests that endogenous access to oxytocin might predict differences in baseline functional dynamics across various neural networks. We addressed this possibility in a pair of experiments. Experiment 2 sought to identify spatial patterns of variability that informed epigenetic differences in *OXTR*; Experiment 3 described an approach for associating spatiotemporal dynamics in connectivity with both epigenetic and behavioral differences.

Both whole-brain and network-specific analyses demonstrated that BOLD variability in subcortical-cerebellum regions indexed *OXTR* methylation. These predictions were driven exclusively by spectral variability measures such as low-frequency power (LFP) and the fractional amplitude of low-frequency fluctuations (fALFF). Notably, the vast majority of nodes in the Shen atlas subcortical-cerebellum network are localized to structures such as the basal ganglia, thalamus/hypothalamus, and

brainstem. These are all highly-populated by dopamine neurons and also receive direct projections along oxytocin pathways^{27,34}. Dopamine circuits in these regions are likely modulated by mesolimbic oxytocin, which may cause shifts between tonic, phasic, and bursty firing states^{51,201,202}. Thus, decreased endogenous oxytocin action may disrupt baseline oscillatory patterns expressed across these regions. Interestingly, *increases* in low-frequency dynamics were associated with higher-levels of methylation—power in these frequency bands is commonly thought to represent biologically-relevant information (as low-frequency fluctuations form the basis for intrinsic functional connectivity). However, some evidence suggests that oxytocin reduces spontaneous background firing and enhances higher-frequency synchrony⁶—it is unclear whether this translates well into physiologically-slow signals such as BOLD (particularly at the baseline resting state), but it may explain why decreased methylation corresponded to decreases in LFP and fALFF.

We also observed significant associations between *OXTR* methylation and temporal and spectral variability in higher-level visual processing networks. In particular, our models demonstrated a right-lateralized effect of BOLD variability on methylation in visual association regions. The areas selected by our model extended into ventral temporal areas that are associated with emotional information processing²⁰⁴, but on a broader scale, this fits with the notion that nonverbal social information is dominantly processed in the right hemisphere¹⁹⁷. We interpret these results as a function of baseline differences in bottom-up predictive coding systems—a more thorough discussion is contained in the section below.

Finally, with respect to dynamic connectivity, increases in entropy across dorsal DMN and anterior SN nodes predicted higher levels of methylation. Thus, decreased access to endogenous oxytocin was associated with more random patterns of connectivity. In the anterior salience network, these results might also indicate

baseline differences in predictive coding systems—this time from the top-down. Decreased entropy may further be related to metastable network states, which allow for the hierarchical organization necessary to engage in accurate active inference²²⁰. While oxytocin certainly may facilitate synchrony and stability in network connectivity, our approach cannot directly test the hypothesis that endogenous oxytocin action is related to genuine metastability. Nevertheless, in both the dDMN and aSN, increased entropy exclusively predicted increases in *OXTR* methylation, suggesting that noisy, low-fidelity connectivity may be spurred by decreased access to oxytocin.

5.4 Oxytocin and social inference

We previously argued that social cognition is an inherently inferential process. Recall that socially-relevant signals in the environment (e.g. an emotional facial expression) must first be salient enough for perception: after orienting your attention to this input, the signal travels in a bottom-up fashion through the brain's sensory pathways. Autonomic responses simultaneously help to form an interoceptive, internal representation of the exogenous stimulus (in this case, an emotional state), which is then tested against a top-down prediction generated from higher-level cortical systems. Critically, in order to avoid prediction error, the representation that reaches the top-down interpreter must be *precise*—this requires high SNR and coordinated signaling across forward-propagating circuits in the bottom-up system.

Our findings in Experiments 2 and 3 suggest that *OXTR* methylation may modulate the baseline functional dynamics of both bottom-up and top-down predictive coding systems. From the bottom-up, patterns of BOLD variability in right-lateralized visual association regions indexed one's endogenous access to oxytocin. Additionally, baseline dynamics in the dopamine-rich subcortical-cerebellum

network were associated with epigenetic variability in *OXTR*. It is likely that both of these networks interact to generate bottom-up representations of social information. For example, in the case of emotional inference, the autonomic systems that simulate the physiology of an emotional response are densely populated with oxytocin neurons^{1,31,34}. The precision of a physiologic representation is known to be heavily modulated by dopamine^{104,124}, which further interacts with mesolimbic oxytocin^{50,51}. In general, there is evidence to suspect that oxytocin coordinates synchrony between these components¹²⁸ and directly impacts firing states of dopaminergic neurons^{201,202}.

In the absence of stimulation, there is a large class of dopaminergic neurons that exhibit tonic firing patterns in preparation for stimulus-evoked activity^{199,200}. We suggest that oxytocin may similarly facilitate coherent, spontaneous “preparatory” states in visual association and subcortical components of bottom-up prediction coding pathways—given a relevant environmental input, oxytocin can then readily induce a phase shift that suppresses spontaneous background activity and enables high-fidelity transfer of information to higher-level cortical systems⁶.

From the top-down, entropy across the aSN was consistently associated with higher levels of *OXTR* methylation. Nodes of the aSN such as the anterior insula, anterior cingulate, and dorsomedial prefrontal cortex are putatively responsible for integrating bottom-up signals with an embodied model of the social-emotional self^{105,106}. However, for accurate predictions to emerge from this process, there is evidence that entropy in the brain must be suppressed—excessive disorder disrupts the hierarchical organization of predictive coding pathways and may introduce communication errors in feedback loops transmitting interoceptive signals and higher-order predictions^{220,221}. Although entropy is necessarily increased by prediction error, the brain uses this information to fine-tune its representations and thus

revert back to a state of low-entropy contentedness²²⁰. Our results suggest that a pervasive high-entropy baseline in networks supporting active social inference may be due to decreased access to oxytocin, which otherwise supports stable connectivity states. However, given that our analyses included only healthy young adults, it is not clear how these patterns of entropy and methylation might manifest in social deficit disorders.

5.5 Bridging the gap between genes and behavior

In our final experiment, we proposed an entropy-based network endophenotype that might jointly explain molecular and behavioral-level variability. It was hypothesized that increased levels of entropy would predict higher levels of methylation, and as a result, higher expression of the broad autism phenotype. Indeed, connectivity entropy in the dDMN successfully predicted both *OXTR* methylation and BAP scores; however, the celebration was short-lived. Rather than yielding a positive association between entropy and each measure, higher levels of entropy predicted greater methylation but *lower* expression of autistic-like traits. This reflected an unexpected inverse relationship between methylation and BAP—wholly counter to previous reports of increased methylation in ASD relative to neurotypicals⁶³. While unexpected, neurotypicals may not demonstrate the same effects as clinical ASD for a number of reasons. We considered several potential explanations: 1) a nonlinear relationship between methylation, entropy, and behavior over the full spectrum of individuals; 2) compensation via arginine vasopressin; and 3) increased instances of hydroxymethylation in neurotypicals, which would *amplify*, not decrease, *OXTR* expression and endogenous access to oxytocin.

Current accounts of the “Bayesian brain” in predictive coding suggest that the brain is constantly poised in a state of “self-organized instability”^{220,221}. Although

seemingly paradoxical, this hypothesis suggests that the brain balances itself between hierarchical order (necessary for accurate top-down predictions) and entropic flexibility (necessary to learn from prediction error). Accordingly, extended states of too little or too much entropy may spiral into pathology^{219–221}.

This notion of a sweet spot in brain entropic states (with respect to behavior) is most consistent with the idea of a nonlinear or parabolic relationship between methylation, entropy, and behavior—it follows from our data that neurotypicals who exhibit low degrees of entropy display more autistic-like traits. Individuals who are high in entropy predict the opposite behavioral outcome, but it is unclear *how high* these individuals truly are relative to those with actual social deficit disorders. What is high for neurotypicals may actually be in the mid-range of the full spectrum. Furthermore, a nonlinear relationship between entropy and behavior does not preclude the possibility that hydroxymethylation is still a factor. As is likely to be the case in nature, there may be an incredibly tangled web of associations between various flavors of methylation, entropy, and social behavioral phenotypes.

Although it may be a massive undertaking, our understanding of the paths between genes, brains, and behavior would benefit immensely from future work considering all of the above factors. We submit that we have barely scratched the surface of the true nature of these relationships; nevertheless, we hope these findings lay a useful foundation for the use of network endophenotypes in uncovering the molecular and neural roots of complex human behavior.

5.6 Conclusion

A major goal of modern neuroscience is to understand how individual differences in the brain contribute to the rich variety of phenotypes expressed across the popu-

lation. Unfortunately, we are often limited in the spatial resolution our methods allow, preventing us from acquiring a more complete picture of how various levels of the system might interact. Here we offer a novel approach to understanding the hierarchical nature of human brain systems, demonstrating that molecular-level information can be decoded from intrinsic and task-evoked characteristics of macroscale functional networks. Moreover, we show that the baseline dynamics of network connectivity may provide a unifying endophenotype between genes and behavior. Future efforts to illuminate complex interactions across molecular, cellular, and cortical-level system components will allow us to better target where and how these systems break down, offering new avenues for intervention and treatment of disease states.

Bibliography

- [1] Buijs, R. M. Intra- and extrahypothalamic vasopressin and oxytocin pathways in the rat. Pathways to the limbic system, medulla oblongata and spinal cord. *Cell Tissue Res.* **192**, 423–435 (1978).
- [2] Carter, C. S. Oxytocin pathways and the evolution of human behavior. *Annu. Rev. Psychol.* **65**, 17–39 (2014).
- [3] Kiss, A. & Mikkelson, J. D. Oxytocin—Anatomy and functional assignments: A minireview. *Endocr. Regul.* **39**, 97–105 (2005).
- [4] Windle, R. J., Shanks, N., Lightman, S. L. & Ingram, C. D. Central oxytocin administration reduces stress-induced corticosterone release and anxiety behavior in rats. *Endocrinology* **138**, 2829–2834 (1997).
- [5] Lin, Y.-T., Huang, C.-C. & Hsu, K.-S. Oxytocin promotes long-term potentiation by enhancing epidermal growth factor receptor-mediated local translation of protein kinase Mzeta. *J. Neurosci.* **32**, 15476–15488 (2012).
- [6] Owen, S. F. *et al.* Oxytocin enhances hippocampal spike transmission by modulating fast-spiking interneurons. *Nature* **500**, 458–462 (2013).
- [7] Bethlehem, R. A., van Honk, J., Auyeung, B. & Baron-Cohen, S. Oxytocin, brain physiology, and functional connectivity: A review of intranasal oxytocin fMRI studies. *Psychoneuroendocrinology* **38**, 962–974 (2013).

- [8] Domes, G. *et al.* Oxytocin attenuates amygdala responses to emotional faces regardless of valence. *Biol. Psychiatry* **62**, 1187–1190 (2007).
- [9] Gordon, I. *et al.* Intranasal oxytocin enhances connectivity in the neural circuitry supporting social motivation and social perception in children with autism. *Sci. Rep.* **6**, 35054EP (2016).
- [10] Kirsch, P. *et al.* Oxytocin modulates neural circuitry for social cognition and fear in humans. *J. Neurosci.* **25**, 11489–11493 (2005).
- [11] Riem, M. M. E. *et al.* No laughing matter: Intranasal oxytocin administration changes functional brain connectivity during exposure to infant laughter. *Neuropsychopharmacology* **37**, 1257–1266 (2012).
- [12] Sripatha, C. S. *et al.* Oxytocin enhances resting-state connectivity between amygdala and medial frontal cortex. *Int. J. Neuropsychopharmacol.* **16**, 255–260 (2012).
- [13] Gordon, I., Martin, C., Feldman, R. & Leckman, J. F. Oxytocin and social motivation. *Dev. Cogn. Neurosci.* **1**, 471–493 (2011).
- [14] Baumgartner, T., Heinrichs, M., Vonlanthen, A., Fischbacher, U. & Fehr, E. Oxytocin shapes the neural circuitry of trust and trust adaptation in humans. *Neuron* **58**, 639–650 (2008).
- [15] Kosfeld, M., Heinrichs, M., Zak, P. J., Fischbacher, U. & Fehr, E. Oxytocin increases trust in humans. *Nature* **435**, 673–676 (2005).
- [16] Bartz, J. A. *et al.* Oxytocin selectively improves empathic accuracy. *Psychol. Sci.* **21**, 1426–1428 (2010).
- [17] Scheele, D. *et al.* Oxytocin modulates social distance between males and females. *J. Neurosci.* **32**, 16074–16079 (2012).

- [18] Domes, G., Heinrichs, M., Michel, A., Berger, C. & Herpertz, S. C. Oxytocin improves “mind-reading” in humans. *Biol. Psychiatry* **61**, 731–733 (2007).
- [19] Rimmele, U., Hediger, K., Heinrichs, M. & Klaver, P. Oxytocin makes a face in memory familiar. *J. Neurosci.* **29**, 38–42 (2009).
- [20] Kéri, S. & Benedek, G. Oxytocin enhances the perception of biological motion in humans. *Cogn. Affect. & Behav. Neurosci.* **9**, 237–241 (2009).
- [21] Andari, E. *et al.* Promoting social behavior with oxytocin in high-functioning autism spectrum disorders. *Proc. Natl. Acad. Sci. U. S. A.* **107**, 4389–4394 (2010).
- [22] Woolley, J. D. *et al.* Oxytocin administration enhances controlled social cognition in patients with schizophrenia. *Psychoneuroendocrinology* **47**, 116–125 (2014).
- [23] Feldman, R., Monakhov, M., Pratt, M. & Ebstein, R. P. Oxytocin pathway genes: Evolutionary ancient system impacting on human affiliation, sociality, and psychopathology. *Biol. Psychiatry* **79**, 174–184 (2016).
- [24] Garrison, J. L. *et al.* Oxytocin/vasopressin-related peptides have an ancient role in reproductive behavior. *Science* **338**, 540–543 (2012).
- [25] Vargas-Pinilla, P. *et al.* Evolutionary pattern in the OXT-OXTR system in primates: Coevolution and positive selection footprints. *Proc. Natl. Acad. Sci. U. S. A.* **112**, 88–93 (2015).
- [26] Yamashita, K. & Kitano, T. Molecular evolution of the oxytocin-oxytocin receptor system in eutherians. *Mol. Phylogenet. Evol.* **67**, 520–528 (2013).

- [27] Meyer-Lindenberg, A., Domes, G., Kirsch, P. & Heinrichs, M. Oxytocin and vasopressin in the human brain: Social neuropeptides for translational medicine. *Nat. Rev. Neurosci.* **12**, 524–538 (2011).
- [28] Gimpl, G. & Fahrenholz, F. The oxytocin receptor system: Structure, function, and regulation. *Physiological Reviews* **81**, 629–683 (2001).
- [29] Chini, B. & Manning, M. Agonist selectivity in the oxytocin/vasopressin receptor family: New insights and challenges. *Biochem. Soc. Trans.* **35**, 737–741 (2007).
- [30] Manning, M. *et al.* Peptide and non-peptide agonists and antagonists for the vasopressin and oxytocin v1a, v1b, V2 and OT receptors: Research tools and potential therapeutic agents. In Neumann, I. D. & Landgraf, R. (eds.) *Advances in vasopressin and oxytocin—From genes to behaviour to disease.*, vol. 170 of *Prog. Brain Res.*, 473–512 (Elsevier, 2008).
- [31] Buijs, R. M., De Vries, G. J., Van Leeuwen, F. W. & Swaab, D. F. Vasopressin and oxytocin: Distribution and putative functions in the brain. *Prog. Brain Res.* **60**, 115–122 (1983).
- [32] Insel, T. R. & Shapiro, L. E. Oxytocin receptor distribution reflects social organization in monogamous and polygamous voles. *Proc. Natl. Acad. Sci. U. S. A.* **89**, 5981–5985 (1992).
- [33] Insel, T. R. & Shapiro, L. E. Oxytocin receptors and maternal behavior. *Ann. N. Y. Acad. Sci.* **652**, 122–141 (1992).
- [34] Otero-Garcia, M., Agustin-Pavon, C., Lanuza, E. & Martinez-Garcia, F. Distribution of oxytocin and co-localization with arginine vasopressin in the brain of mice. *Brain Struct. Funct.* **221**, 3445–3473 (2016).

- [35] Huber, D., Veinante, P. & Stoop, R. Vasopressin and oxytocin excite distinct neuronal populations in the central amygdala. *Science* **308**, 245–248 (2005).
- [36] Ross, H. E. *et al.* Characterization of the oxytocin system regulating affiliative behavior in female prairie voles. *Neuroscience* **162**, 892–903 (2009).
- [37] Landgraf, R. & Neumann, I. D. Vasopressin and oxytocin release within the brain: A dynamic concept of multiple and variable modes of neuropeptide communication. *Front. Neuroendocrinol.* **25**, 150–176 (2004).
- [38] Ludwig, M. & Leng, G. Dendritic peptide release and peptide-dependent behaviours. *Nat. Rev. Neurosci.* **7**, 126–136 (2006).
- [39] Mens, W. B., Laczi, F., Tonnaer, J. A., de Kloet, E. R. & van Wimersma Greidanus, T. B. Vasopressin and oxytocin content in cerebrospinal fluid and in various brain areas after administration of histamine and pentyletetrazol. *Pharmacol. Biochem. Behav.* **19**, 587–591 (1983).
- [40] Foote, S. L. & Morrison, J. H. Extrathalamic modulation of cortical function. *Annu. Rev. Neurosci.* **10**, 67–95 (1987).
- [41] Kroener, S., Chandler, L. J., Phillips, P. E. M. & Seamans, J. K. Dopamine modulates persistent synaptic activity and enhances the signal-to-noise ratio in the prefrontal cortex. *PLoS One* **4**, e6507 (2009).
- [42] Servan-Schreiber, D., Printz, H. & Cohen, J. D. A network model of catecholamine effects: Gain, signal-to-noise ratio, and behavior. *Science* **249**, 892–895 (1990).
- [43] Servan-Schreiber, D., Bruno, R. M., Carter, C. S. & Cohen, J. D. Dopamine and the mechanisms of cognition: Part i. a neural network model predicting dopamine effects on selective attention. *Biol. Psychiatry* **43**, 713–722 (1998).

- [44] Thurley, K., Senn, W. & Luscher, H.-R. Dopamine increases the gain of the input-output response of rat prefrontal pyramidal neurons. *J. Neurophysiol.* **99**, 2985–2997 (2008).
- [45] Wise, R. A. Dopamine, learning and motivation. *Nat. Rev. Neurosci.* **5**, 483–494 (2004).
- [46] Baskerville, T. A., Allard, J., Wayman, C. & Douglas, A. J. Dopamine-oxytocin interactions in penile erection. *Eur. J. Neurosci.* **30**, 2151–2164 (2009).
- [47] Liu, Y. & Wang, Z. Nucleus accumbens oxytocin and dopamine interact to regulate pair bond formation in female prairie voles. *Neuroscience* **121**, 537–544 (2003).
- [48] Smeltzer, M. D., Curtis, J. T., Aragona, B. J. & Wang, Z. Dopamine, oxytocin, and vasopressin receptor binding in the medial prefrontal cortex of monogamous and promiscuous voles. *Neurosci. Lett.* **394**, 146–151 (2006).
- [49] Baribeau, D. & Anagnostou, E. Oxytocin and vasopressin: Linking pituitary neuropeptides and their receptors to social neurocircuits. *Front. in Neurosci.* **9**, 335 (2015).
- [50] Love, T. M. *et al.* Oxytocin gene polymorphisms influence human dopaminergic function in a sex-dependent manner. *Biol. Psychiatry* **72**, 198–206 (2012).
- [51] Love, T. M. Oxytocin, motivation and the role of dopamine. *Pharmacol. Biochem. Behav.* **119**, 49–60 (2014).
- [52] Shamay-Tsoory, S. G. & Abu-Akel, A. The social salience hypothesis of oxytocin. *Biol. Psychiatry* **79**, 194–202 (2016).
- [53] Skuse, D. H. & Gallagher, L. Dopaminergic-neuropeptide interactions in the social brain. *Trends Cogn. Sci.* **13**, 27–35 (2009).

- [54] Young, L. J. & Wang, Z. The neurobiology of pair bonding. *Nat. Neurosci.* **7**, 1048–1054 (2004).
- [55] Furman, D. J., Chen, M. C. & Gotlib, I. H. Variant in oxytocin receptor gene is associated with amygdala volume. *Psychoneuroendocrinology* **36**, 891–897 (2011).
- [56] Inoue, H. *et al.* Association between the oxytocin receptor gene and amygdalar volume in healthy adults. *Biol. Psychiatry* **68**, 1066–1072 (2010).
- [57] Tost, H. *et al.* A common allele in the oxytocin receptor gene (OXTR) impacts prosocial temperament and human hypothalamic-limbic structure and function. *Proc. Natl. Acad. Sci. U. S. A.* **107**, 13936–13941 (2010).
- [58] Loth, E. *et al.* Oxytocin receptor genotype modulates ventral striatal activity to social cues and response to stressful life events. *Biol. Psychiatry* **76**, 367–376 (2014).
- [59] Riem, M. M. E., Pieper, S., Out, D., Bakermans-Kranenburg, M. J. & van Ijzendoorn, M. H. Oxytocin receptor gene and depressive symptoms associated with physiological reactivity to infant crying. *Soc. Cogn. Affect. Neurosci.* **6**, 294–300 (2011).
- [60] Wang, J. *et al.* Variant in OXTR gene and functional connectivity of the hypothalamus in normal subjects. *Neuroimage* **81**, 199–204 (2013).
- [61] Wang, J. *et al.* Relationship of a common OXTR gene variant to brain structure and default mode network function in healthy humans. *Neuroimage* **147**, 500–506 (2017).

- [62] Di Napoli, A., Warriar, V., Baron-Cohen, S. & Chakrabarti, B. Genetic variation in the oxytocin receptor (OXTR) gene is associated with Asperger Syndrome. *Molecular Autism* **5**, 1–7 (2014).
- [63] Gregory, S. G. *et al.* Genomic and epigenetic evidence for oxytocin receptor deficiency in autism. *BMC Med.* **7**, 62 (2009).
- [64] Hovey, D. *et al.* Antisocial behavior and polymorphisms in the oxytocin receptor gene: Findings in two independent samples. *Mol. Psychiatry* **21**, 983–988 (2016).
- [65] Jacob, S. *et al.* Association of the oxytocin receptor gene (OXTR) in Caucasian children and adolescents with autism. *Neurosci. Lett.* **417**, 6–9 (2007).
- [66] LoParo, D. & Waldman, I. D. The oxytocin receptor gene (OXTR) is associated with autism spectrum disorder: A meta-analysis. *Mol. Psychiatry* **20**, 640–646 (2015).
- [67] Skuse, D. H. *et al.* Common polymorphism in the oxytocin receptor gene (OXTR) is associated with human social recognition skills. *Proc. Natl. Acad. Sci. U. S. A.* **111**, 1987–1992 (2014).
- [68] Apicella, C. L. *et al.* No association between oxytocin receptor (OXTR) gene polymorphisms and experimentally elicited social preferences. *PLoS One* **5**, e11153 (2010).
- [69] Tansey, K. E. *et al.* Oxytocin receptor (OXTR) does not play a major role in the aetiology of autism: Genetic and molecular studies. *Neurosci. Lett.* **474**, 163–167 (2010).
- [70] Yrigollen, C. M. *et al.* Genes controlling affiliative behavior as candidate genes for autism. *Biol. Psychiatry* **63**, 911–916 (2008).

- [71] Bakermans-Kranenburg, M. J. & van Ijzendoorn, M. H. A sociability gene? Meta-analysis of oxytocin receptor genotype effects in humans. *Psychiatr. Genet.* **24**, 45–51 (2014).
- [72] Kusui, C. *et al.* DNA methylation of the human oxytocin receptor gene promoter regulates tissue-specific gene suppression. *Biochem. Biophys. Res. Commun.* **289**, 681–686 (2001).
- [73] Dadds, M. R. *et al.* Methylation of the oxytocin receptor gene and oxytocin blood levels in the development of psychopathy. *Dev. Psychopathol.* **26**, 33–40 (2014).
- [74] Grove, T. B. *et al.* Oxytocin receptor (OXTR) methylation and cognition in psychotic disorders. *Mol. Neuropsychiatry* **2**, 151–160 (2016).
- [75] Kim, Y.-R., Kim, J.-H., Kim, M. J. & Treasure, J. Differential methylation of the oxytocin receptor gene in patients with anorexia nervosa: A pilot study. *PLoS One* **9**, e88673 (2014).
- [76] Ziegler, C. *et al.* Oxytocin receptor gene methylation: Converging multilevel evidence for a role in social anxiety. *Neuropsychopharmacology* **40**, 1528–1538 (2015).
- [77] Born, J. *et al.* Sniffing neuropeptides: A transnasal approach to the human brain. *Nat. Neurosci.* **5**, 514–516 (2002).
- [78] Leng, G. & Ludwig, M. Intranasal oxytocin: Myths and delusions. *Biol. Psychiatry* **79**, 243–250 (2016).
- [79] Striepens, N. *et al.* Elevated cerebrospinal fluid and blood concentrations of oxytocin following its intranasal administration in humans. *Sci. Rep.* **3**, 3440 (2013).

- [80] Gamer, M., Zurowski, B. & Büchel, C. Different amygdala subregions mediate valence-related and attentional effects of oxytocin in humans. *Proc. Natl. Acad. Sci. U. S. A.* **107**, 9400–9405 (2010).
- [81] Adolphs, R. The social brain: Neural basis of social knowledge. *Annu. Rev. Psychol.* **60**, 693–716 (2009).
- [82] Brothers, L. The neural basis of primate social communication. *Motivation & Emotion* **14**, 81–91 (1990).
- [83] Haas, B. W., Anderson, I. W. & Smith, J. M. Navigating the complex path between the oxytocin receptor gene (OXTR) and cooperation: An endophenotype approach. *Front. Hum. Neurosci.* **7**, 801 (2013).
- [84] Domes, G. *et al.* Effects of intranasal oxytocin on emotional face processing in women. *Psychoneuroendocrinology* **35**, 83–93 (2010).
- [85] Labuschagne, I. *et al.* Oxytocin attenuates amygdala reactivity to fear in generalized social anxiety disorder. *Neuropsychopharmacology* **35**, 2403–2413 (2010).
- [86] Labuschagne, I. *et al.* Medial frontal hyperactivity to sad faces in generalized social anxiety disorder and modulation by oxytocin. *Int. J. Neuropsychopharmacol.* 1–14 (2011).
- [87] Neumann, I. D. & Landgraf, R. Balance of brain oxytocin and vasopressin: Implications for anxiety, depression, and social behaviors. *Trends Neurosci.* **35**, 649–659 (2012).
- [88] Shamay-Tsoory, S. G. *et al.* Intranasal administration of oxytocin increases envy and schadenfreude (gloating). *Biol. Psychiatry* **66**, 864–870 (2009).

- [89] Hermundstad, A. M. *et al.* Structural foundations of resting-state and task-based functional connectivity in the human brain. *Proc. Natl. Acad. Sci. U. S. A.* **110**, 6169–6174 (2013).
- [90] Hermundstad, A. M. *et al.* Structurally-constrained relationships between cognitive states in the human brain. *PLoS Comput. Biol.* **10**, e1003591 (2014).
- [91] Rilling, J. K. *et al.* Effects of intranasal oxytocin and vasopressin on cooperative behavior and associated brain activity in men. *Psychoneuroendocrinology* **37**, 447–461 (2012).
- [92] Dodhia, S. *et al.* Modulation of resting-state amygdala-frontal functional connectivity by oxytocin in generalized social anxiety disorder. *Neuropsychopharmacology* **39**, 2061–2069 (2014).
- [93] Ebner, N. C. *et al.* Oxytocin's effect on resting-state functional connectivity varies by age and sex. *Psychoneuroendocrinology* **69**, 50–59 (2016).
- [94] Watanabe, T. *et al.* Clinical and neural effects of six-week administration of oxytocin on core symptoms of autism. *Brain* **138**, 3400–3412 (2015).
- [95] Frijling, J. L. *et al.* Effects of intranasal oxytocin on amygdala reactivity to emotional faces in recently trauma-exposed individuals. *Soc. Cogn. Affect. Neurosci.* **11**, 327 (2016).
- [96] Kumar, J., Vollm, B. & Palaniyappan, L. Oxytocin affects the connectivity of the precuneus and the amygdala: A randomized, double-blinded, placebo-controlled neuroimaging trial. *Int. J. Neuropsychopharmacol.* **18** (2014).
- [97] Wittfoth-Schardt, D. *et al.* Oxytocin modulates neural reactivity to children's faces as a function of social salience. *Neuropsychopharmacology* **37**, 1799–1807 (2012).

- [98] McCullough, M. E., Churchland, P. S. & Mendez, A. J. Problems with measuring peripheral oxytocin: Can the data on oxytocin and human behavior be trusted? *Neurosci. Biobehav. Rev.* **37**, 1485–1492 (2013).
- [99] Jack, A., Connelly, J. J. & Morris, J. P. DNA methylation of the oxytocin receptor gene predicts neural response to ambiguous social stimuli. *Front. Hum. Neurosci.* **6**, 280 (2012).
- [100] Puglia, M. H., Lillard, T. S., Morris, J. P. & Connelly, J. J. Epigenetic modification of the oxytocin receptor gene influences the perception of anger and fear in the human brain. *Proc. Natl. Acad. Sci. U. S. A.* **112**, 3308–3313 (2015).
- [101] Quattrocki, E. & Friston, K. Autism, oxytocin and interoception. *Neurosci. Biobehav. Rev.* **47**, 410–430 (2014).
- [102] Craig, A. D. How do you feel? interoception: The sense of the physiological condition of the body. *Nat. Rev. Neurosci.* **3**, 655–666 (2002).
- [103] Seth, A. K. Interoceptive inference, emotion, and the embodied self. *Trends Cogn. Sci.* **17**, 565–573 (2013).
- [104] Friston, K. A theory of cortical responses. *Philos. Trans. R. Soc. Lond. B Biol. Sci.* **360**, 815–836 (2005).
- [105] Apps, M. A. & Tsakiris, M. The free-energy self: A predictive coding account of self-recognition. *Neurosci. Biobehav. Rev.* **41**, 85–97 (2014).
- [106] Damasio, A. & Carvalho, G. B. The nature of feelings: Evolutionary and neurobiological origins. *Nat. Rev. Neurosci.* **14**, 143–152 (2013).
- [107] Blair, R. Responding to the emotions of others: Dissociating forms of empathy through the study of typical and psychiatric populations. *Conscious. Cogn.* **14**, 698–718 (2005).

- [108] Cox, C. L. *et al.* The balance between feeling and knowing: Affective and cognitive empathy are reflected in the brain's intrinsic functional dynamics. *Soc. Cogn. Affect. Neurosci.* **7**, 727 (2012).
- [109] Bal, E. *et al.* Emotion recognition in children with autism spectrum disorders: Relations to eye gaze and autonomic state. *J. Autism Dev. Disord.* **40**, 358–370 (2010).
- [110] Hirstein, W., Iversen, P. & Ramachandran, V. S. Autonomic responses of autistic children to people and objects. *Proc. Biol. Sci. R. Soc.* **268**, 1883–1888 (2001).
- [111] Ming, X., Julu, P. O., Brimacombe, M., Connor, S. & Daniels, M. L. Reduced cardiac parasympathetic activity in children with autism. *Brain Dev.* **27**, 509–516 (2005).
- [112] Vaughan Van Hecke, A. *et al.* Electroencephalogram and heart rate regulation to familiar and unfamiliar people in children with autism spectrum disorders. *Child Dev.* **80**, 1118–1133 (2009).
- [113] Dawson, G. & McKissick, F. C. Self-recognition in autistic children. *J. Autism Dev. Disord.* **14**, 383–394 (1984).
- [114] Martino, A. D. *et al.* Functional brain correlates of social and nonsocial processes in autism spectrum disorders: An activation likelihood estimation meta-analysis. *Biol. Psychiatry* **65**, 63–74 (2009).
- [115] Osterling, J. & Dawson, G. Early recognition of children with autism: A study of first birthday home videotapes. *J. Autism Dev. Disord.* **24**, 247–257 (1994).
- [116] Uddin, L. Q. The self in autism: An emerging view from neuroimaging. *Neurocase* **17**, 201–208 (2011).

- [117] Baron-Cohen, S., Leslie, A. M. & Frith, U. Does the autistic child have a “theory of mind”? *Cognition* **21**, 37–46 (1985).
- [118] Green, L. *et al.* Oxytocin and autistic disorder: Alterations in peptide forms. *Biol. Psychiatry* **50**, 609–613 (2001).
- [119] Modahl, C. *et al.* Plasma oxytocin levels in autistic children. *Biol. Psychiatry* **43**, 270–277 (1998).
- [120] Lestanova, Z. *et al.* Oxytocin increases neurite length and expression of cytoskeletal proteins associated with neuronal growth. *J. Mol. Neurosci.* **59**, 184–192 (2016).
- [121] Leuner, B., Caponiti, J. M. & Gould, E. Oxytocin stimulates adult neurogenesis even under conditions of stress and elevated glucocorticoids. *Hippocampus* **22**, 861–868 (2012).
- [122] Sánchez-Vidaña, D. I. *et al.* Repeated treatment with oxytocin promotes hippocampal cell proliferation, dendritic maturation and affects socio-emotional behavior. *Neuroscience* **333**, 65–77 (2016).
- [123] Farroni, T., Csibra, G., Simion, F. & Johnson, M. H. Eye contact detection in humans from birth. *Proc. Natl. Acad. Sci. U. S. A.* **99**, 9602–9605 (2002).
- [124] Friston, K. J. *et al.* Dopamine, affordance and active inference. *PLoS Comput. Biol.* **8**, 1–20 (2012).
- [125] Lévy, F., Kendrick, K. M., Goode, J. A., Guevara-Guzman, R. & Keverne, E. B. Oxytocin and vasopressin release in the olfactory bulb of parturient ewes: Changes with maternal experience and effects on acetylcholine, γ -aminobutyric acid, glutamate and noradrenaline release. *Brain Res.* **669**, 197–206 (1995).

- [126] Viviani, D. & Stoop, R. Opposite effects of oxytocin and vasopressin on the emotional expression of the fear response. In Neumann, I. D. & Landgraf, R. (eds.) *Advances in vasopressin and oxytocin—From genes to behaviour to disease.*, vol. 170 of *Prog. Brain Res.*, 207–218 (Elsevier, 2008).
- [127] Viviani, D., Terrettaz, T., Magara, F. & Stoop, R. Oxytocin enhances the inhibitory effects of diazepam in the rat central medial amygdala. *Neuropharmacology* **58**, 62–68 (2010).
- [128] Rossoni, E. *et al.* Emergent synchronous bursting of oxytocin neuronal network. *PLoS Comput. Biol.* **4**, 1–12 (2008).
- [129] van den Heuvel, M. P., Scholtens, L. H., Feldman Barrett, L., Hilgetag, C. C. & de Reus, M. A. Bridging cytoarchitectonics and connectomics in human cerebral cortex. *J. Neurosci.* **35**, 13943–13948 (2015).
- [130] Dinstein, I. *et al.* Unreliable evoked responses in autism. *Neuron* **75**, 981–991 (2012).
- [131] Moseley, R. *et al.* Whole-brain functional hypoconnectivity as an endophenotype of autism in adolescents. *Neuroimage: Clinical* **9**, 140–152 (2015).
- [132] Müller, R.-A. *et al.* Underconnected, but how? A survey of functional connectivity MRI studies in autism spectrum disorders. *Cereb. Cortex* **21**, 2233–2243 (2011).
- [133] Kumsta, R., Hummel, E., Chen, F. S. & Heinrichs, M. Epigenetic regulation of the oxytocin receptor gene: Implications for behavioral neuroscience. *Front. Neurosci.* **7**, 83 (2013).

- [134] Bales, K. L., Abdelnabi, M., Cushing, B. S., Ottinger, M. A. & Carter, C. S. Effects of neonatal oxytocin manipulations on male reproductive potential in prairie voles. *Physiol. Behav.* **81**, 519–526 (2004).
- [135] Bales, K. L., Boone, E., Epperson, P., Hoffman, G. & Carter, C. S. Are behavioral effects of early experience mediated by oxytocin? *Front. Psychiatry* **2**, 24 (2011).
- [136] Bales, K. L. & Perkeybile, A. M. Developmental experiences and the oxytocin receptor system. *Horm. Behav.* **61**, 313–319 (2012).
- [137] Veenema, A. H. Toward understanding how early-life social experiences alter oxytocin- and vasopressin-regulated social behaviors. *Horm. Behav.* **61**, 304–312 (2012).
- [138] Glahn, D. C. *et al.* Genetic control over the resting brain. *Proc. Natl. Acad. Sci. U. S. A.* **107**, 1223–1228 (2010).
- [139] Richiardi, J. *et al.* Correlated gene expression supports synchronous activity in brain networks. *Science* **348**, 1241–1244 (2015).
- [140] Richmond, S., Johnson, K. A., Seal, M. L., Allen, N. B. & Whittle, S. Development of brain networks and relevance of environmental and genetic factors: A systematic review. *Neurosci. Biobehav. Rev.* **71**, 215–239 (2016).
- [141] Sinclair, B. *et al.* Heritability of the network architecture of intrinsic brain functional connectivity. *Neuroimage* **121**, 243–252 (2015).
- [142] Yang, Z. *et al.* Genetic and environmental contributions to functional connectivity architecture of the human brain. *Cereb. Cortex* **26**, 2341–2352 (2016).
- [143] Mars, R. *et al.* On the relationship between the “default mode network” and the “social brain.”. *Front. Hum. Neurosci.* **6**, 189 (2012).

- [144] Baron-Cohen, S., Wheelwright, S., Skinner, R., Martin, J. & Clubley, E. The autism-spectrum quotient (AQ): Evidence from asperger syndrome/high-functioning autism, males and females, scientists and mathematicians. *J. Autism Dev. Disord.* **31**, 5–17 (2001).
- [145] Castelli, F., Happe, F., Frith, U. & Frith, C. Movement and mind: A functional imaging study of perception and interpretation of complex intentional movement patterns. *Neuroimage* **12**, 314–325 (2000).
- [146] Heider, F. & Simmel, M. An experimental study of apparent behavior. *Am. J. Psychol.* **57**, 243–259 (1944).
- [147] Friston, K. J., Williams, S., Howard, R., Frackowiak, R. S. & Turner, R. Movement-related effects in fMRI time-series. *Magn. Reson. Med.* **35**, 346–355 (1996).
- [148] Tzourio-Mazoyer, N. *et al.* Automated anatomical labeling of activations in SPM using a macroscopic anatomical parcellation of the MNI MRI single-subject brain. *Neuroimage* **15**, 273–289 (2002).
- [149] Bedenbender, J. *et al.* Functional connectivity analyses in imaging genetics: Considerations on methods and data interpretation. *PLoS One* **6**, 1–8 (2011).
- [150] Friston, K. J., Rotshtein, P., Geng, J. J., Sterzer, P. & Henson, R. N. A critique of functional localisers. *Neuroimage* **30**, 1077–1087 (2006).
- [151] Bassett, D. S. *et al.* Dynamic reconfiguration of human brain networks during learning. *Proc. Natl. Acad. Sci. U. S. A.* **108**, 7641–7646 (2011).
- [152] Zhang, Z., Telesford, Q. K., Giusti, C., Lim, K. O. & Bassett, D. S. Choosing wavelet methods, filters, and lengths for functional brain network construction. *PLoS One* **11**, 1–24 (2016).

- [153] Sun, F. T., Miller, L. M. & D'Esposito, M. Measuring interregional functional connectivity using coherence and partial coherence analyses of fMRI data. *Neuroimage* **21**, 647–658 (2004).
- [154] Benesty, J., Chen, J. & Huang, Y. A generalized MVDR spectrum. *IEEE Signal Process. Lett.* **12**, 827–830 (2005).
- [155] Benesty, J., Chen, J. & Huang, Y. Estimation of the coherence function with the MVDR approach. In *IEEE Int. Conf. on Acoustics, Speech, and Signal Process.*, vol. 3, 500–503 (2006).
- [156] Shumway, R. & Stoffer, D. *Time series analysis and its applications*. (Springer-Verlag, New York, NY, USA, 2011).
- [157] Bolt, T., Nomi, J. S., Rubinov, M. & Uddin, L. Q. Correspondence between evoked and intrinsic functional brain network configurations. *Hum. Brain Mapp.* **38**, 1992–2007 (2017).
- [158] Meunier, D., Achard, S., Morcom, A. & Bullmore, E. Age-related changes in modular organization of human brain functional networks. *Neuroimage* **44**, 715–723 (2009).
- [159] van den Heuvel, M. P., Stam, C. J., Kahn, R. S. & Hulshoff Pol, H. E. Efficiency of functional brain networks and intellectual performance. *J. Neurosci.* **29**, 7619–7624 (2009).
- [160] Rubinov, M. & Sporns, O. Complex network measures of brain connectivity: Uses and interpretations. *Neuroimage* **52**, 1059–1069 (2010).
- [161] Tipping, M. E. Sparse Bayesian learning and the relevance vector machine. *J. Mach. Learn. Res.* **1**, 211–244 (2001).

- [162] Tipping, M. E. & Faul, A. C. Fast marginal likelihood maximisation for sparse Bayesian models. In *Proc. of the 9th Int. Workshop on Artificial Intelligence and Statistics*, 3–6 (2003).
- [163] Xia, M., Wang, J. & He, Y. BrainNet Viewer: A network visualization tool for human brain connectomics. *PLoS One* **8**, e68910 (2013).
- [164] Siegel, J. S. *et al.* Data quality influences observed links between functional connectivity and behavior. *Cereb. Cortex* 1–11 (2016).
- [165] Martin, A. & Weisberg, J. Neural foundations for understanding social and mechanical concepts. *Cogn. Neuropsychol.* **20**, 575–587 (2003).
- [166] Dasgupta, S., Tyler, S. C., Wicks, J., Srinivasan, R. & Grossman, E. D. Network connectivity of the right STS in three social perception localizers. *J. Cogn. Neurosci.* **29**, 221–234 (2017).
- [167] Achard, S., Salvador, R., Whitcher, B., Suckling, J. & Bullmore, E. A resilient, low-frequency, small-world human brain functional network with highly connected association cortical hubs. *J. Neurosci.* **26**, 63–72 (2006).
- [168] Bassett, D. S. & Bullmore, E. Small-world brain networks. *Neuroscientist* **12**, 512–523 (2006).
- [169] Boccaletti, S., Latora, V., Moreno, Y., Chavez, M. & Hwang, D.-U. Complex networks: Structure and dynamics. *Physics Reports* **424**, 175–308 (2006).
- [170] Muldoon, S. F., Bridgeford, E. W. & Bassett, D. S. Small-world propensity and weighted brain networks. *Sci. Rep.* **6**, 22057EP (2016).
- [171] van den Heuvel, M. P., Stam, C. J., Boersma, M. & Hulshoff Pol, H. E. Small-world and scale-free organization of voxel-based resting-state functional connectivity in the human brain. *Neuroimage* **43**, 528–539 (2008).

- [172] Buckner, R. L. *et al.* Cortical hubs revealed by intrinsic functional connectivity: Mapping, assessment of stability, and relation to Alzheimer's disease. *J. Neurosci.* **29**, 1860–1873 (2009).
- [173] Crossley, N. A. *et al.* The hubs of the human connectome are generally implicated in the anatomy of brain disorders. *Brain* **137**, 2382–2395 (2014).
- [174] van den Heuvel, M. P. & Sporns, O. Network hubs in the human brain. *Trends Cogn. Sci.* **17**, 683–696 (2013).
- [175] Cole, M. W., Bassett, D. S., Power, J. D., Braver, T. S. & Petersen, S. E. Intrinsic and task-evoked network architectures of the human brain. *Neuron* **83**, 238–251 (2014).
- [176] Finn, E. S. *et al.* Functional connectome fingerprinting: Identifying individuals using patterns of brain connectivity. *Nat. Neurosci.* **18**, 1664–1671 (2015).
- [177] Tavor, I. *et al.* Task-free MRI predicts individual differences in brain activity during task performance. *Science* **352**, 216–220 (2016).
- [178] Garrett, D. D., Kovacevic, N., McIntosh, A. R. & Grady, C. L. Blood oxygen level-dependent signal variability is more than just noise. *J. Neurosci.* **30**, 4914–4921 (2010).
- [179] Garrett, D. D., Kovacevic, N., McIntosh, A. R. & Grady, C. L. The importance of being variable. *J. Neurosci.* **31**, 4496–4503 (2011).
- [180] Turner, B. O., Lopez, B., Santander, T. & Miller, M. B. One dataset, many conclusions: BOLD variability's complicated relationships with age and motion artifacts. *Brain Imaging Behav.* **9**, 115–127 (2015).
- [181] Patel, A. X. *et al.* A wavelet method for modeling and despiking motion artifacts from resting-state fMRI time series. *Neuroimage* **95**, 287–304 (2014).

- [182] Rosenberg, M. D. *et al.* A neuromarker of sustained attention from whole-brain functional connectivity. *Nat. Neurosci.* **19**, 165–171 (2016).
- [183] Shen, X., Papademetris, X. & Constable, R. T. Graph-theory based parcellation of functional subunits in the brain from resting-state fMRI data. *Neuroimage* **50**, 1027–1035 (2010).
- [184] Shen, X., Tokoglu, F., Papademetris, X. & Constable, R. T. Groupwise whole-brain parcellation from resting-state fMRI data for network node identification. *Neuroimage* **82**, 403–415 (2013).
- [185] Tagliazucchi, E., Carhart-Harris, R., Leech, R., Nutt, D. & Chialvo, D. R. Enhanced repertoire of brain dynamical states during the psychedelic experience. *Hum. Brain Mapp.* **35**, 5442–5456 (2014).
- [186] Yu-Feng, Z. *et al.* Altered baseline brain activity in children with ADHD revealed by resting-state functional MRI. *Brain Dev.* **29**, 83–91 (2007).
- [187] Zou, Q.-H. *et al.* An improved approach to detection of amplitude of low-frequency fluctuation (ALFF) for resting-state fMRI: Fractional ALFF. *J. Neurosci. Methods* **172**, 137–141 (2008).
- [188] Cordes, D. *et al.* Frequencies contributing to functional connectivity in the cerebral cortex in “resting-state” data. *AJNR Am. J. Neuroradiol.* **22**, 1326–1333 (2001).
- [189] Lake, D. E., Richman, J. S., Griffin, M. P. & Moorman, J. R. Sample entropy analysis of neonatal heart rate variability. *Am. J. Physiol. Regul. Integr. Comp. Physiol.* **283**, R789–797 (2002).
- [190] Pincus, S. M. Approximate entropy as a measure of system complexity. *Proc. Natl. Acad. Sci. U. S. A.* **88**, 2297–2301 (1991).

- [191] Richman, J. S. & Moorman, J. R. Physiological time-series analysis using approximate entropy and sample entropy. *Am. J. Physiol. Heart Circ. Physiol.* **278**, H2039–2049 (2000).
- [192] Liu, C. Y. *et al.* Complexity and synchronicity of resting state blood oxygenation level-dependent (BOLD) functional MRI in normal aging and cognitive decline. *J. Magn. Reson. Imaging* **38**, 36–45 (2013).
- [193] Sokunbi, M. O. *et al.* Resting state fMRI entropy probes complexity of brain activity in adults with ADHD. *Psychiatry Res.* **214**, 341–348 (2013).
- [194] Wang, Z., Li, Y., Childress, A. R. & Detre, J. A. Brain entropy mapping using fMRI. *PLoS One* **9**, 1–8 (2014).
- [195] Gönen, M. A Bayesian multiple kernel learning framework for single and multiple output regression. In *Proc. of the 20th Eur. Conf. on Artificial Intelligence (ECAI)*, 354–359 (2012).
- [196] Gönen, M. Bayesian efficient multiple kernel learning. In Langford, J. & Pineau, J. (eds.) *Proc. of the 29th Int. Conf. on Machine Learning (ICML)*, 1–8 (2012).
- [197] Brancucci, A., Lucci, G., Mazzatenta, A. & Tommasi, L. Asymmetries of the human social brain in the visual, auditory and chemical modalities. *Philos. Trans. R. Soc. Lond. B Biol. Sci.* **364**, 895–914 (2009).
- [198] Shmuel, A. & Leopold, D. A. Neuronal correlates of spontaneous fluctuations in fmri signals in monkey visual cortex: Implications for functional connectivity at rest. *Hum. Brain Mapp.* **29**, 751–761 (2008).

- [199] Floresco, S. B., West, A. R., Ash, B., Moore, H. & Grace, A. A. Afferent modulation of dopamine neuron firing differentially regulates tonic and phasic dopamine transmission. *Nat. Neurosci.* **6**, 968–973 (2003).
- [200] Grace, A. A., Floresco, S. B., Goto, Y. & Lodge, D. J. Regulation of firing of dopaminergic neurons and control of goal-directed behaviors. *Trends Neurosci.* **30**, 220–227 (2007).
- [201] Briffaud, V., Williams, P., Courty, J. & Broberger, C. Excitation of tuberoinfundibular dopamine neurons by oxytocin: Crosstalk in the control of lactation. *J. Neurosci.* **35**, 4229–4237 (2015).
- [202] Zhang, X. & van den Pol, A. N. Dopamine/tyrosine hydroxylase neurons of the hypothalamic arcuate nucleus release GABA, communicate with dopaminergic and other arcuate neurons, and respond to dynorphin, met-enkephalin, and oxytocin. *J. Neurosci.* **35**, 14966–14982 (2015).
- [203] O’Connell, G. *et al.* Association of genetic variation in the promoter region of OXTR with differences in social affective neural processing. *J. Behav. Brain Sci.* **2**, 60–66 (2012).
- [204] Rudrauf, D. *et al.* Rapid interactions between the ventral visual stream and emotion-related structures rely on a two-pathway architecture. *J. Neurosci.* **28**, 2793–2803 (2008).
- [205] Andrews-Hanna, J. R., Saxe, R. & Yarkoni, T. Contributions of episodic retrieval and mentalizing to autobiographical thought: Evidence from functional neuroimaging, resting-state connectivity, and fMRI meta-analyses. *Neuroimage* **91**, 324–335 (2014).

- [206] Andrews-Hanna, J. R., Smallwood, J. & Spreng, R. N. The default network and self-generated thought: Component processes, dynamic control, and clinical relevance. *Ann. N. Y. Acad. Sci.* **1316**, 29–52 (2014).
- [207] Assaf, M. *et al.* Abnormal functional connectivity of default mode sub-networks in autism spectrum disorder patients. *Neuroimage* **53**, 247–256 (2010).
- [208] Yerys, B. E. *et al.* Default mode network segregation and social deficits in autism spectrum disorder: Evidence from non-medicated children. *Neuroimage: Clinical* **9**, 223–232 (2015).
- [209] Menon, V. & Uddin, L. Q. Saliency, switching, attention and control: A network model of insula function. *Brain Struct. Funct.* **214**, 655–667 (2010).
- [210] Taylor, K. S., Seminowicz, D. A. & Davis, K. D. Two systems of resting state connectivity between the insula and cingulate cortex. *Hum. Brain Mapp.* **30**, 2731–2745 (2009).
- [211] Uddin, L. Q. & Menon, V. The anterior insula in autism: Under-connected and under-examined. *Neurosci. Biobehav. Rev.* **33**, 1198–1203 (2009).
- [212] Uddin, L. Q. *et al.* Salience network-based classification and prediction of symptom severity in children with autism. *JAMA Psychiatry* **70**, 869–879 (2013).
- [213] Shine, J. M. *et al.* Estimation of dynamic functional connectivity using multiplication of temporal derivatives. *Neuroimage* **122**, 399–407 (2015).
- [214] Shine, J. M. *et al.* The dynamics of functional brain networks: Integrated network states during cognitive task performance. *Neuron* **92**, 544–554 (2016).

- [215] Shine, J. M., Koyejo, O. & Poldrack, R. A. Temporal metastates are associated with differential patterns of time-resolved connectivity, network topology, and attention. *Proc. Natl. Acad. Sci. U. S. A.* **113**, 9888–9891 (2016).
- [216] Jin, S.-G., Wu, X., Li, A. X. & Pfeifer, G. P. Genomic mapping of 5-hydroxymethylcytosine in the human brain. *Nucleic Acids Res.* **39**, 5015–5024 (2011).
- [217] Song, C.-X. *et al.* Selective chemical labeling reveals the genome-wide distribution of 5-hydroxymethylcytosine. *Nat. Biotech.* **29**, 68–72 (2011).
- [218] Tognoli, E. & Kelso, J. A. S. The metastable brain. *Neuron* **81**, 35–48 (2014).
- [219] Carhart-Harris, R. *et al.* The entropic brain: A theory of conscious states informed by neuroimaging research with psychedelic drugs. *Front. Hum. Neurosci.* **8**, 20 (2014).
- [220] Friston, K. The free-energy principle: A unified brain theory? *Nat. Rev. Neurosci.* **11**, 127–138 (2010).
- [221] Friston, K., Breakspear, M. & Deco, G. Perception and self-organized instability. *Front. Comput. Neurosci.* **6**, 44 (2012).
- [222] Bassett, D. S. *et al.* Hierarchical organization of human cortical networks in health and schizophrenia. *J. Neurosci.* **28**, 9239–9248 (2008).
- [223] Cheng, W., Rolls, E. T., Gu, H., Zhang, J. & Feng, J. Autism: Reduced connectivity between cortical areas involved in face expression, theory of mind, and the sense of self. *Brain* **138**, 1382–1393 (2015).
- [224] Bassett, D. S. & Gazzaniga, M. S. Understanding complexity in the human brain. *Trends. Cogn. Sci.* **15**, 200–209 (2011).

Appendix A

Supplementary information:

Experiment 1

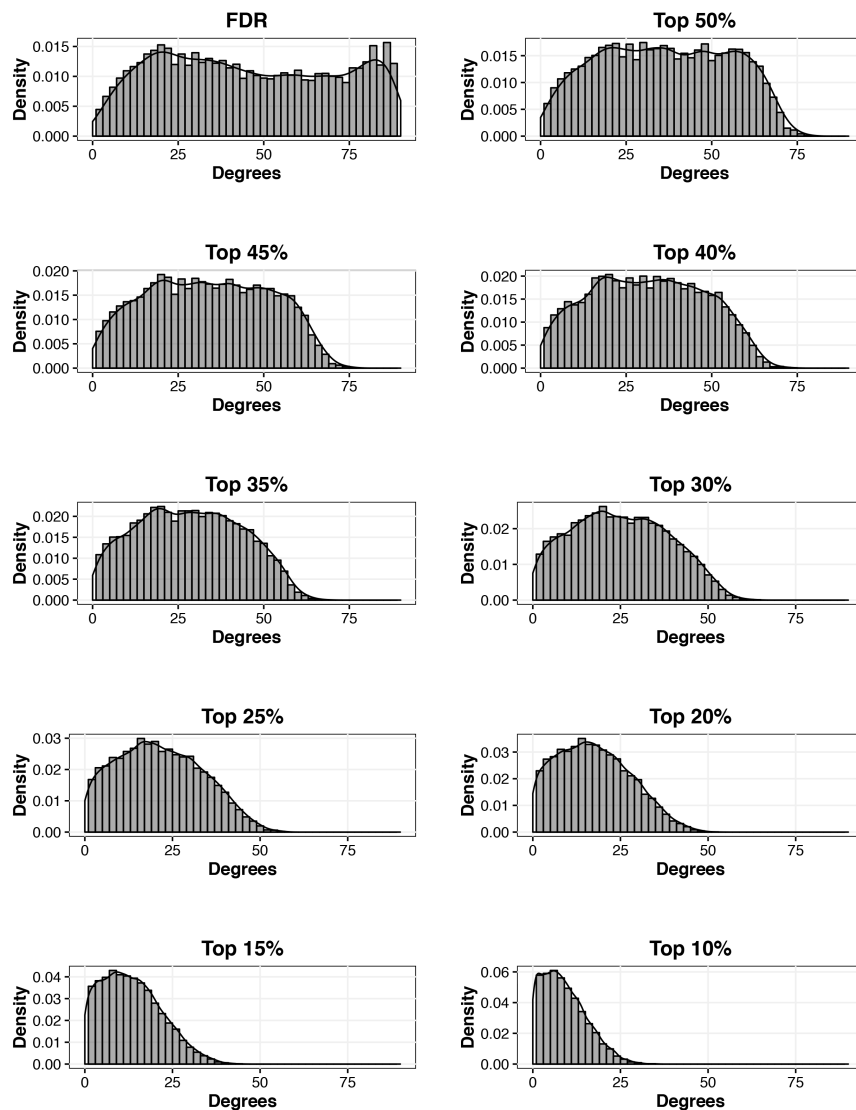


Figure A.1: Proportional thresholds nontrivially affect overall network topology. Degree distributions for each threshold are given for the full 90-region network (Study 1 data, $N = 127$). As the threshold becomes more stringent, the distribution approaches a heavily-tailed power law—this is characteristic of so-called “small-world” networks where a few highly-connected hubs control most of the information flow.

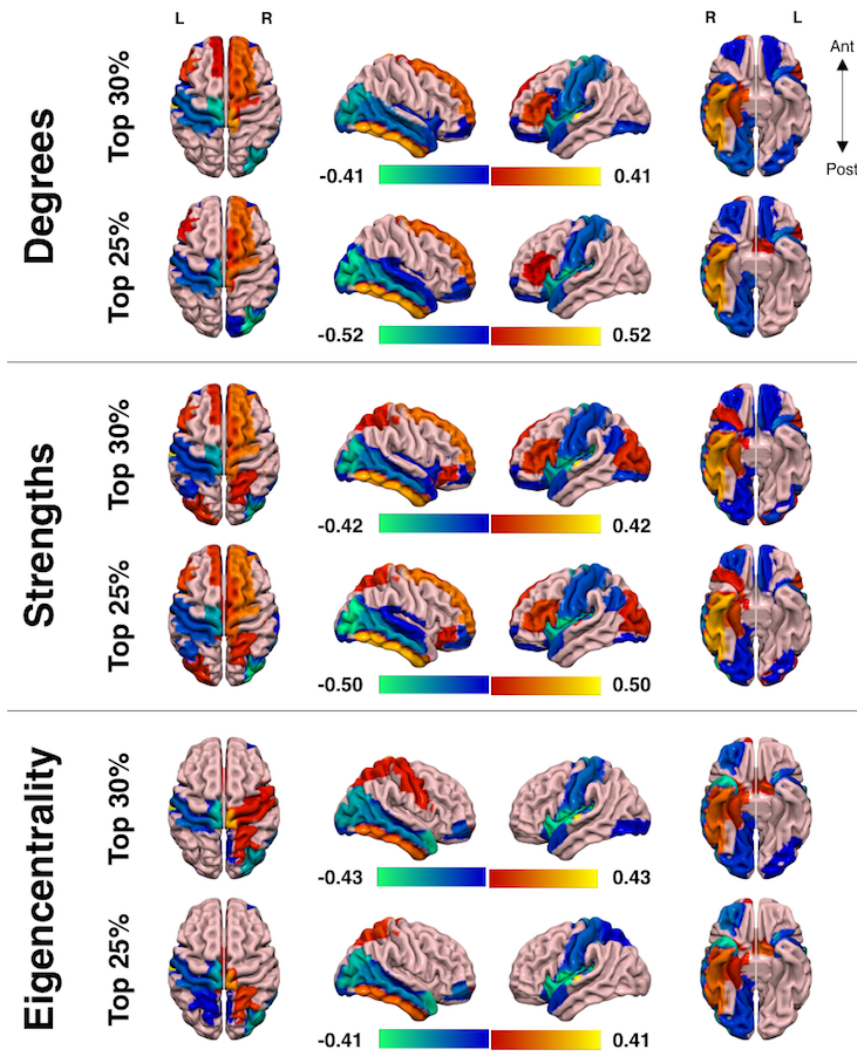


Figure A.2: Multivariate weight maps derived from the full 90-region network. Relevance vector regression identified a highly consistent set of regions relevant for predicting *OXTR* methylation. Models trained/tested using Study 1 data ($N = 127$). For simplicity, only models from CpG site -860 are presented here; weight maps are provided at the top 30% and top 25% thresholds. Values reflect average weights across CV folds, normalized to unit length. “Hot” colors push the prediction function towards higher expected methylation (with increased connectivity) while “cool” colors indicate the reverse.

Metric	Threshold	Prediction correlation	Prediction error (<i>RMSE</i>)
Degrees	FDR	0.11 (.227)	6.86 (.477)
	Top50	0.10 (.270)	6.86 (.480)
	Top45	0.19 (.102)	6.54 (.212)
	Top40	0.37 (.010)	5.87 (.012)
	Top35	0.35 (.009)	5.93 (.013)
	Top30	0.27 (.044)	6.25 (.078)
	Top25	0.06 (.331)	6.92 (.524)
	Top20	0.16 (.142)	6.80 (.383)
	Top15	0.26 (.052)	6.40 (.109)
	Top10	-0.12 (.742)	7.71 (.931)
Strengths	FDR	0.29 (.031)	6.11 (.045)
	Top50	0.21 (.097)	6.44 (.182)
	Top45	0.20 (.109)	6.43 (.193)
	Top40	0.28 (.032)	6.19 (.069)
	Top35	0.21 (.106)	6.43 (.197)
	Top30	0.17 (.141)	6.55 (.249)
	Top25	0.05 (.329)	7.01 (.599)
	Top20	0.11 (.252)	7.07 (.626)
	Top15	0.10 (.240)	7.22 (.716)
	Top10	-0.14 (.792)	7.87 (.967)
Eigencentality	FDR	0.19 (.142)	6.63 (.344)
	Top50	0.22 (.085)	6.46 (.167)
	Top45	0.21 (.091)	6.51 (.196)
	Top40	0.25 (.060)	6.33 (.100)
	Top35	0.26 (.049)	6.38 (.133)
	Top30	0.28 (.033)	6.20 (.065)
	Top25	0.24 (.060)	6.32 (.102)
	Top20	0.20 (.102)	6.61 (.257)
	Top15	0.19 (.118)	6.63 (.285)
	Top10	0.13 (.195)	6.60 (.294)

Table A.1: Whole-brain RVR model fit: CpG site -934. Model fit statistics (*prediction correlation* and *prediction error*) are given for each metric and network threshold. *P*-values derived from 1,000 iterations of nonparametric permutation testing are given in parentheses.

Metric	Threshold	Prediction correlation	Prediction error (<i>RMSE</i>)
Degrees	FDR	0.06 (.351)	6.44 (.591)
	Top50	0.12 (.217)	6.48 (.625)
	Top45	0.31 (.021)	5.76 (.070)
	Top40	0.34 (.016)	5.57 (.034)
	Top35	0.48 (.001)	4.97 (.001)
	Top30	0.56 (.001)	4.63 (.001)
	Top25	0.48 (.001)	4.91 (.001)
	Top20	0.47 (.001)	5.03 (.001)
	Top15	0.35 (.009)	5.46 (.010)
	Top10	0.16 (.161)	6.04 (.185)
Strengths	FDR	0.13 (.176)	6.30 (.469)
	Top50	0.25 (.051)	5.96 (.200)
	Top45	0.22 (.080)	6.18 (.380)
	Top40	0.26 (.053)	6.00 (.222)
	Top35	0.47 (.002)	5.04 (.001)
	Top30	0.53 (.001)	4.78 (.001)
	Top25	0.44 (.005)	5.17 (.006)
	Top20	0.42 (.001)	5.26 (.002)
	Top15	0.31 (.023)	5.58 (.025)
	Top10	0.21 (.087)	5.91 (.128)
Eigencentality	FDR	0.18 (.129)	5.95 (.210)
	Top50	0.23 (.071)	5.87 (.120)
	Top45	0.27 (.041)	5.77 (.072)
	Top40	0.26 (.044)	5.77 (.076)
	Top35	0.41 (.005)	5.21 (.004)
	Top30	0.42 (.001)	5.18 (.001)
	Top25	0.41 (.002)	5.17 (.001)
	Top20	0.36 (.003)	5.41 (.006)
	Top15	0.23 (.062)	5.84 (.096)
	Top10	0.01 (.453)	6.60 (.784)

Table A.2: Whole-brain RVR model fit: CpG site -860. Relevance vector regression fit statistics (*prediction correlation* and *prediction error*) are given for each metric and network threshold. *P*-values derived from 1,000 iterations of nonparametric permutation testing are given in parentheses.

Region	Degrees	Strengths	Eigencentality	Mean
Amygdala (L)	50%	20%	40%	36.67%
*Amygdala (R)	100%	100%	90%	96.67%
Angular Gyrus (L)	80%	100%	20%	66.67%
*Angular Gyrus (R)	60%	90%	80%	76.67%
Calcarine Fissure (L)	40%	20%	30%	30%
Calcarine Fissure (R)	70%	70%	60%	66.67%
Caudate (L)	50%	40%	40%	43.33%
*Caudate (R)	80%	40%	30%	50%
Cuneus (L)	40%	20%	10%	23.33%
Cuneus (R)	70%	70%	80%	73.33%
*Fusiform Gyrus (L)	90%	90%	80%	86.67%
*Fusiform Gyrus (R)	60%	90%	80%	76.67%
*Gyrus Rectus (L)	80%	80%	90%	83.33%
*Gyrus Rectus (R)	90%	100%	100%	96.67%
*Heschl's Gyrus (L)	70%	80%	50%	66.67%
Heschl's Gyrus (R)	50%	30%	80%	53.33%
Hippocampus (L)	70%	60%	60%	63.33%
Hippocampus (R)	40%	80%	20%	46.67%
*Insula (L)	90%	90%	100%	93.33%
*Insula (R)	100%	100%	100%	100%
Lingual Gyrus (L)	10%	20%	20%	16.67%
*Lingual Gyrus (R)	0%	50%	10%	20%
*Olfactory Cortex (L)	70%	70%	0%	46.67%
Olfactory Cortex (R)	40%	40%	50%	43.33%
Pallidum (L)	30%	90%	30%	50%
Pallidum (R)	20%	10%	0%	10%
Paracentral Lobule (L)	10%	20%	60%	30%
*Paracentral Lobule (R)	90%	90%	90%	90%
*Parahippocampal Gyrus (L)	70%	100%	100%	90%
*Parahippocampal Gyrus (R)	100%	100%	100%	100%
*Postcentral Gyrus (L)	30%	20%	60%	36.67%
*Postcentral Gyrus (R)	100%	100%	100%	100%
*Precentral Gyrus (L)	100%	100%	90%	96.67%
Precentral Gyrus (R)	30%	10%	90%	43.33%
*Precuneus (L)	90%	90%	100%	93.33%
Precuneus (R)	50%	40%	50%	46.67%
Putamen (L)	50%	90%	50%	63.33%
Putamen (R)	10%	20%	0%	10%
*Rolandic Operculum (L)	30%	30%	0%	20%
*Rolandic Operculum (R)	90%	80%	100%	90%
Supplementary Motor Area (L)	60%	50%	60%	56.67%
*Supplementary Motor Area (R)	100%	100%	100%	100%
*Supramarginal Gyrus (L)	100%	100%	90%	96.67%
Supramarginal Gyrus (R)	40%	20%	30%	30%
Thalamus (L)	40%	20%	80%	46.67%
Thalamus (R)	10%	70%	0%	26.67%

Table A.3: Relevance probabilities: CpG site -934. For each AAL node and network metric, we give the probability of inclusion across RVR models for CpG site -934. Metric-specific columns indicate the probability of nonzero weight across all network threshold levels; the far right column gives the mean. Starred (*) nodes were ultimately included in the 43-region subnetwork (relevant in over 75% of models for *either* CpG site -934 or CpG site -860).

Region	Degrees	Strengths	Eigencentality	Mean
Amygdala (L)	30%	0%	60%	30%
*Amygdala (R)	40%	40%	70%	50%
Angular Gyrus (L)	50%	90%	0%	46.67%
*Angular Gyrus (R)	70%	90%	30%	63.33%
Calcarine Fissure (L)	40%	50%	20%	36.67%
Calcarine Fissure (R)	50%	30%	10%	30%
Caudate (L)	50%	40%	60%	50%
*Caudate (R)	80%	90%	80%	83.33%
Cuneus (L)	30%	80%	0%	36.67%
Cuneus (R)	90%	60%	10%	53.33%
*Fusiform Gyrus (L)	20%	60%	30%	36.67%
*Fusiform Gyrus (R)	60%	50%	20%	43.33%
*Gyrus Rectus (L)	30%	90%	10%	43.33%
*Gyrus Rectus (R)	50%	60%	0%	36.67%
*Heschl's Gyrus (L)	100%	100%	100%	100%
Heschl's Gyrus (R)	50%	60%	20%	43.33%
Hippocampus (L)	30%	10%	20%	20%
Hippocampus (R)	30%	30%	20%	26.67%
*Insula (L)	100%	90%	100%	96.67%
*Insula (R)	90%	100%	10%	66.67%
Lingual Gyrus (L)	30%	20%	10%	20%
*Lingual Gyrus (R)	80%	90%	90%	86.67%
*Olfactory Cortex (L)	100%	100%	100%	100%
Olfactory Cortex (R)	70%	70%	50%	63.33%
Pallidum (L)	20%	20%	60%	33.33%
Pallidum (R)	20%	40%	20%	26.67%
Paracentral Lobule (L)	30%	10%	20%	20%
*Paracentral Lobule (R)	70%	70%	70%	70%
*Parahippocampal Gyrus (L)	100%	100%	100%	100%
*Parahippocampal Gyrus (R)	90%	90%	90%	90%
*Postcentral Gyrus (L)	100%	100%	90%	96.67%
*Postcentral Gyrus (R)	40%	20%	30%	30%
*Precentral Gyrus (L)	80%	50%	80%	70%
Precentral Gyrus (R)	60%	40%	100%	66.67%
*Precuneus (L)	50%	50%	0%	33.33%
Precuneus (R)	30%	30%	100%	53.33%
Putamen (L)	40%	20%	10%	23.33%
Putamen (R)	50%	50%	0%	33.33%
*Rolandic Operculum (L)	100%	100%	100%	100%
*Rolandic Operculum (R)	80%	90%	60%	76.67%
Supplementary Motor Area (L)	0%	10%	0%	3.33%
*Supplementary Motor Area (R)	100%	100%	100%	100%
*Supramarginal Gyrus (L)	20%	30%	70%	40%
Supramarginal Gyrus (R)	20%	0%	30%	16.67%
Thalamus (L)	10%	10%	30%	16.67%
Thalamus (R)	70%	70%	80%	73.33%

Table A.4: Relevance probabilities: CpG site -860. For each AAL node and network metric, we give the probability of inclusion across RVR models for CpG site -860. Metric-specific columns indicate the probability of nonzero weight across all network threshold levels; the far right column gives the mean. Starred (*) nodes were ultimately included in the 43-region subnetwork (relevant in over 75% of models for *either* CpG site -934 or CpG site -860).

Metric	Threshold	Prediction correlation	Prediction error (<i>RMSE</i>)
Degrees	FDR	-0.01 (.488)	6.80 (.972)
	Top50	0.18 (.092)	6.20 (.259)
	Top45	0.22 (.058)	6.19 (.237)
	Top40	0.33 (.004)	5.77 (.006)
	Top35	0.29 (.023)	5.93 (.046)
	Top30	0.29 (.016)	5.95 (.052)
	Top25	0.26 (.022)	6.06 (.089)
	Top20	0.28 (.014)	5.94 (.038)
	Top15	0.22 (.047)	6.25 (.273)
	Top10	0.15 (.152)	6.16 (.188)
Strengths	FDR	0.18 (.110)	6.15 (.434)
	Top50	0.21 (.065)	6.15 (.225)
	Top45	0.21 (.063)	6.20 (.274)
	Top40	0.30 (.013)	5.87 (.025)
	Top35	0.32 (.005)	5.79 (.016)
	Top30	0.25 (.038)	6.07 (.111)
	Top25	0.20 (.091)	6.26 (.376)
	Top20	0.21 (.058)	6.24 (.336)
	Top15	0.24 (.037)	6.12 (.140)
	Top10	0.11 (.225)	6.20 (.257)
Eigencentality	FDR	0.12 (.170)	6.29 (.408)
	Top50	0.10 (.244)	6.38 (.573)
	Top45	0.15 (.157)	6.28 (.409)
	Top40	0.23 (.118)	6.20 (.285)
	Top35	0.25 (.049)	6.06 (.103)
	Top30	0.24 (.039)	6.02 (.074)
	Top25	0.24 (.025)	6.03 (.075)
	Top20	0.11 (.064)	6.06 (.109)
	Top15	0.17 (.107)	6.09 (.146)
	Top10	0.12 (.209)	6.11 (.182)

Table A.5: Subnetwork RVR model fit: CpG site -934. Fit statistics (*prediction correlation* and *prediction error*) from subnetwork relevance vector regression are given for each metric and network threshold. *P*-values derived from 1,000 iterations of nonparametric permutation testing are given in parentheses.

Metric	Threshold	Prediction correlation	Prediction error (<i>RMSE</i>)
Degrees	FDR	0.09 (.236)	5.90 (.606)
	Top50	0.29 (.012)	5.36 (.011)
	Top45	0.30 (.013)	5.37 (.019)
	Top40	0.24 (.042)	5.52 (.061)
	Top35	0.27 (.021)	5.46 (.034)
	Top30	0.38 (.002)	5.18 (.001)
	Top25	0.25 (.003)	5.32 (.110)
	Top20	0.37 (.002)	5.29 (.006)
	Top15	0.37 (.002)	5.32 (.007)
	Top10	0.06 (.318)	5.93 (.656)
Strengths	FDR	0.34 (.002)	5.30 (.013)
	Top50	0.23 (.041)	5.62 (.165)
	Top45	0.26 (.017)	5.54 (.067)
	Top40	0.21 (.067)	5.67 (.254)
	Top35	0.26 (.025)	5.61 (.041)
	Top30	0.39 (.001)	5.17 (.001)
	Top25	0.40 (.001)	5.18 (.002)
	Top20	0.35 (.003)	5.29 (.005)
	Top15	0.38 (.002)	5.24 (.025)
	Top10	0.03 (.392)	6.00 (.750)
Eigencentality	FDR	0.23 (.053)	5.57 (.116)
	Top50	0.17 (.106)	5.73 (.312)
	Top45	0.25 (.042)	5.53 (.079)
	Top40	0.16 (.123)	5.75 (.334)
	Top35	0.19 (.225)	5.90 (.641)
	Top30	0.23 (.042)	5.61 (.120)
	Top25	0.18 (.113)	5.78 (.410)
	Top20	0.17 (.129)	5.83 (.501)
	Top15	0.21 (.051)	5.67 (.234)
	Top10	0.09 (.273)	5.93 (.701)

Table A.6: Subnetwork RVR model fit: CpG site -860. Fit statistics (*prediction correlation* and *prediction error*) from subnetwork relevance vector regression are given for each metric and network threshold. *P*-values derived from 1,000 iterations of nonparametric permutation testing are given in parentheses.

Appendix B

Supplementary information:

Experiment 2

Metric	CpG site -934	CpG site -860
ApEn	7.85 (.277)	8.20 (.863)
SampEn	8.31 (.590)	8.06 (.842)
σ_t	7.48 (.057)	7.46 (.379)
σ_ω^2	7.42 (.047)	7.18 (.220)
LFP	8.27 (.397)	7.55 (.380)
fALFF	9.11 (.804)	6.36 (.006)

Table B.1: Whole-brain BEMKL model fit. Values indicate root mean squared error (*RMSE*) across CV folds; *p*-values from 1,000 iterations of nonparametric permutation testing are given in parentheses.

Metric	CpG site -934	CpG site -860
ApEn	8.50 (.967)	7.30 (.879)
SampEn	8.00 (.892)	6.63 (.270)
σ_t	7.85 (.890)	7.41 (.986)
σ_ω^2	8.38 (.993)	7.42 (.979)
LFP	8.67 (1.00)	8.15 (1.00)
fALFF	8.97 (1.00)	7.25 (.976)

Table B.2: Medial frontal RVR model fit. Values indicate root mean squared error (*RMSE*) across CV folds; *p*-values from 1,000 iterations of nonparametric permutation testing are given in parentheses.

Metric	CpG site -934	CpG site -860
ApEn	8.41 (.974)	8.03 (.994)
SampEn	7.58 (.477)	7.76 (.990)
σ_t	8.35 (.994)	6.53 (.209)
σ_ω^2	7.46 (.491)	6.80 (.572)
LFP	7.73 (.899)	7.95 (1.00)
fALFF	7.40 (.504)	6.44 (.133)

Table B.3: Frontoparietal RVR model fit. Values indicate root mean squared error (*RMSE*) across CV folds; *p*-values from 1,000 iterations of nonparametric permutation testing are given in parentheses.

Metric	CpG site -934	CpG site -860
ApEn	7.54 (.549)	6.40 (.110)
SampEn	8.29 (.992)	7.18 (.926)
σ_t	7.15 (.194)	7.28 (.974)
σ_ω^2	7.13 (.171)	7.34 (.984)
LFP	7.42 (.624)	7.34 (.998)
fALFF	7.77 (.964)	7.15 (.978)

Table B.4: Default mode RVR model fit. Values indicate root mean squared error (*RMSE*) across CV folds; *p*-values from 1,000 iterations of nonparametric permutation testing are given in parentheses.

Metric	CpG site -934	CpG site -860
ApEn	7.37 (.153)	7.90 (.918)
SampEn	7.65 (.344)	6.83 (.294)
σ_t	7.41 (.247)	7.29 (.860)
σ_ω^2	7.46 (.285)	7.53 (.955)
LFP	7.81 (.766)	6.03 (.016)
fALFF	7.30 (.193)	6.39 (.071)

Table B.5: Subcortical-cerebellum RVR model fit. Values indicate root mean squared error (*RMSE*) across CV folds; *p*-values from 1,000 iterations of nonparametric permutation testing are given in parentheses.

Metric	CpG site -934	CpG site -860
ApEn	7.79 (.504)	6.39 (.073)
SampEn	5.17 (.111)	7.56 (.961)
σ_t	7.21 (.153)	6.79 (.453)
σ_ω^2	7.30 (.239)	6.85 (.534)
LFP	7.89 (.888)	7.01 (.811)
fALFF	7.08 (.114)	6.72 (.474)

Table B.6: Motor RVR model fit. Values indicate root mean squared error (*RMSE*) across CV folds; *p*-values from 1,000 iterations of nonparametric permutation testing are given in parentheses.

Metric	CpG site -934	CpG site -860
ApEn	7.35 (.394)	7.08 (.857)
SampEn	8.20 (.988)	7.85 (.997)
σ_t	7.33 (.565)	6.62 (.445)
σ_ω^2	7.55 (.843)	6.79 (.775)
LFP	7.43 (.860)	6.49 (.274)
fALFF	6.93 (.089)	6.91 (.929)

Table B.7: Visual I RVR model fit. Values indicate root mean squared error (*RMSE*) across CV folds; *p*-values from 1,000 iterations of nonparametric permutation testing are given in parentheses.

Metric	CpG site -934	CpG site -860
ApEn	6.55 (.007)	6.84 (.758)
SampEn	6.63 (.016)	6.99 (.915)
σ_t	7.18 (.380)	5.34 (.100)
σ_ω^2	7.19 (.412)	6.46 (.242)
LFP	6.82 (.049)	6.58 (.418)
fALFF	7.20 (.438)	6.95 (.940)

Table B.8: Visual II RVR model fit. Values indicate root mean squared error (*RMSE*) across CV folds; *p*-values from 1,000 iterations of nonparametric permutation testing are given in parentheses.

Metric	CpG site -934	CpG site -860
ApEn	7.92 (.905)	6.63 (.261)
SampEn	8.49 (.570)	7.79 (1.00)
σ_t	6.30 (.002)	6.83 (.690)
σ_ω^2	6.20 (.001)	7.04 (.920)
LFP	7.14 (.284)	6.98 (.925)
fALFF	8.09 (.998)	6.27 (.068)

Table B.9: Visual association RVR model fit. Values indicate root mean squared error (*RMSE*) across CV folds; *p*-values from 1,000 iterations of nonparametric permutation testing are given in parentheses.

Metrics	ApEn	SampEn	σ_t	σ_ω^2	LFP	fALFF
ApEn	–	7.28 (< .001)	0.33 (.744)	0.44 (.663)	0.66 (.511)	1.27 (.203)
SampEn	–	–	-0.95 (.343)	-0.82 (.418)	-0.83 (.407)	0.03 (.973)
σ_t	–	–	–	18.19 (< .001)	7.72 (< .001)	2.52 (.012)
σ_ω^2	–	–	–	–	8.04 (< .001)	2.55 (.011)
LFP	–	–	–	–	–	7.54 (< .001)
fALFF	–	–	–	–	–	–

Table B.10: Average whole-brain correlations between BOLD variability metrics. *Z*-scored mean correlation coefficients across all participants are given for each pairwise comparison. In general, entropy measures were significantly related to each other but not to any other metrics. Temporal and spectral variability measures (including LFP and fALFF) were also significantly correlated. Together, this suggests that entropy is capturing a unique functional characteristic of the BOLD signal relative to other standard measures of BOLD variability.